Experimental and Theoretical Challenges in Understanding the rp-Process on Accreting Neutron Stars

By

Mark Sidney Wallace

A DISSERTATION

Submitted to
Michigan State University
in partial fulfillment of the requirements
for the degree of

DOCTOR OF PHILOSOPHY

Department of Physics and Astronomy

2005

ABSTRACT

Experimental and Theoretical Challenges in Understanding the rp-Process on Accreting Neutron Stars

By

Mark Sidney Wallace

The rp-process is responsible for observed X-ray bursts originating from accreting neutron stars in binary systems. This explosive process drives nucleosynthesis toward the proton drip line where little experimental data exists, making it necessary to rely on models.

One of these models (GAMBLER) has been developed in order to study the effects detailed nuclear physics has on the rp-process above ^{56}Ni. Results from calculations suggest the mass of ^{64}Ge and ^{65}As will have a strong effect on the nucleosynthetic processing time beyond ^{64}Ge.

The use of (p,d) transfer reactions for measuring the masses of ^{64}Ge and ^{65}As was studied by detailed Monte Carlo simulations which take into considerations all experimental uncertainties. The results show this technique provides a powerful tool in determining the masses of proton rich nuclei with high accuracy. However, it requires high-resolution detectors to achieve accuracies of astrophysical relevance.

A high-resolution array (HiRA) of silicon strip detector and CsI(Tl) crystal was developed. This array consists of 20 identical telescopes, each consisting of a 65 μm thick single sided silicon strip detector, a 1.5 mm thick double sided silicon strip detector, and 4 CsI(Tl) crystals read out by photo-diodes. The array utilizes a new application specific integrated circuit (ASIC) to signal processing of the 2000 signals.

In addition to HiRA, a high-rate, high-resolution, position sensitive beam tracking system using micro channel plate detectors was developed.

To my family

ACKNOWLEDGMENTS

The work of this thesis is not only the work I have done, but has been a collaboration with many people. I would like to acknowledge many of these people for there role in this work, or in helping me succeed in graduate school.

I must start by thanking my research adviser, Bill Lynch. His wisdom and guidance have been invaluable to me. When things looked impossible, he has always helped me through, teaching me never to loose focus on the big picture.

I would like to thank all the members of the ”HiRA” group. There could never have been ”HiRA” without the efforts of so many people. I would like to thank Betty Tsang for keeping the group organized, and helping ”get stuff done”. When projects around the lab slowed down, she could always speed them up. I must thank former HiRA post-docs Marc-Jan van Goethem and Giuseppe Verde. Marc-Jan’s attention to detail and his guidance while working in the HiRA group has been wonderful, and his continued friendship after his departure a blessing. His work has shaped the pages of this dissertation. Giuseppe Verde has been a friend and mentor for so many years. I have been fortunate to have worked with such people.

I would also like to thank current HiRA members whose contributions can not be accurately measured. Mike Famiano is the toughest guy I know. I’ve seen him work for 3 days straight on experiments. His hard work and dedication has brought rough ideas into hard realities for HiRA. I have learned so much from him, as well as his hard working personality. Franck Delaunay is the most recent addition to the HiRA group, but he has been no less instrumental then all others. We have worked very closely over the past year or two. His careful and systematic approach to physics has really helped me. His love for the buffalo burger and Guinness has also been appreciated.

I would like to thank Andy Rogers for his help in so many things. Andy has been instrumental in so many areas of HiRA over the past few years. It seems anytime something new comes up, we ask Andy to do it. He always does, and does it well. He

is the future of this group. His skills and work ethic will surly make him successful.

There have been so many people in the lab that have helped make HiRA a success. I can't name them all here but I must acknowledge the hard work of a few people. The first, and by most instrumental, is Len Morris. He has helped design every nut and bolt in HiRA. He has designed -and redesigned- so many parts for us I could not begin to count them all. I would like to thank Ron Fox for all his help on computer programming and software development, without which HiRA would not be very useful. John Yurkon has always been helpful when trying to understand technical problems. I must thank Raman Anantaraman for his patience with me as I scheduled and rescheduled HiRA test runs over and over again.

There are many current and former graduate students that I must acknowledge. To begin with I will mention those who came before me. Thanks goes out to Katie Miller, Joann Prisciandaro, Ryan Clement, Eric Tryggestad, and Pat Lofy. A special thanks goes out to Pat Lofy as he "recruited" me onto the Art's softball team. Art's softball has helped keep me sane during so many busy times and Pat was a true leader both on and off the field.

I must thank my office mate, group member, and coffee buddy Michal Mocho. I don't know what I will do without 10 am coffee time. Thanks goes out to Paul Hosmer, my study partner without whom I might not have made it through the first few years of classes and exams. I would also like to thank some of my other classmates, Bill Peters and Mike Crosser, Jeremy Seitz, and Ben Perry.

Debbie Simmons has been a wonderful help throughout my entire graduate career, I thank her for helping me along the way.

A special thanks to the members of my thesis committee for their advise and help during my graduate career. Brad Sherrill has been a great help during all the S800 experiments and anytime I have general questions. Hendrik Schatz has really helped me learn the astrophysics part of nuclear astrophysics. Wayne Repko was my first professor and his teaching helped me through the first few years. Vladamir

Zelevinsky taught me E&M and nuclear structure. His teaching has been instrumental in my education. All of their advice as member of my committee is appreciated.

I would like to thank a few other scientists outside of the NSCL for their contributions. I thank Ed Brown for his help on developing GAMBLER, and for his insight into nuclear astrophysics. I would also like to thank Dan Shapira of Oak Ridge National Lab for his collaboration on the MCP project. I have enjoyed working with him and appreciate all the knowledge he has shared with me.

Several former and current undergraduates at the NSCL have contributed to my work and I would like to acknowledge them. Brian Nett was a great help and a good friend. Dave Oostdyke was instrumental in the HiRA power supply, ”Sparky”, and also a good friend. Stephanie Simpson has helped on so many different projects I can’t list them all here, but her help is appreciated.

I would like to thank some friends outside of the physics department as well. A special thanks goes out to Anne Fischer and Katie Boin whose friendship has helped me through the difficulties of graduate school. Chris Jambor and Claire Vielle have been wonderful friends too. I have enjoyed playing volleyball, eating cheese, and drinking wine with them.

I would like to end by thanking my family. To my parents, Karen and Robert Wallace, for always being there for me, not just in graduate school, but my entire life. I thank my twin brother Rob. Only a twin could understand how much his support has meant to me. Thanks to Paul, my older brother, for being such a good friend and brother. I would also like to thank my sisters-in-law Paula Wallace, and Nicole Wallace. I am fortunate to have two wonderful and supportive sisters-in-law. I want to end by thanking the newest members of my family, my niece Baylie, and my nephews Owen, and Oak. Visiting them has really helped me relax and enjoy some of the very busy times in graduate school.

Contents

1 Introduction **1**

1.1 Motivations 1

1.2 Astrophysics 4

1.3 Nuclear Physics of the rp-process 11

1.4 Major Focuses of Dissertation 14

1.5 Organization of Dissertation 15

2 rp-Process Calculations **16**

2.1 Introduction 16

2.2 Nuclear Physics in GAMBLER 17

2.2.1 Non-Resonant Reaction Rates 19

2.2.2 Resonant Reaction Rates 21

2.2.3 Screening Effects 22

2.3 Thermodynamics in GAMBLER 24

2.3.1 Equation of State (EOS) 24

2.3.2 Energy Transport 25

2.4 Numerical Technique 27

2.4.1 Time Step Calculation 31

2.5 Inputs for GAMBLER 33

2.6 Burst Conditions 34

2.7 Results from GAMBLER 38

2.8 Key Nuclear Physics 44

2.9 Conclusions 48

3 Experimental Design **50**

3.1 Introduction 50

3.2 Choice of measurement technique 51

3.2.1 Direct Methods 51

3.2.2 Indirect Methods 52

3.2.3 Using (p,d) in Inverse Kinematics 53

3.3 Beam Characteristics 57

3.4 Experimental Resolution 58

3.4.1 Beam Energy Effects 59

3.4.2 Target Effects 60

3.4.3 Deuteron Energy 64

3.4.4 Reaction Angle 65

3.4.5 Total Resolution 69
3.4.6 Background 70
3.5 Final Results 71

4 The High Resolution Array, HiRA 72
4.1 Introduction 72
4.2 Silicon strip detectors 74
4.2.1 Silicon detector design 76
4.2.2 Testing of silicon detectors 83
4.3 CsI(Tl) crystals 86
4.3.1 Crystal selection 88
4.3.2 Crystal preparation 89
4.3.3 Alpha scanning 92
4.3.4 Direct primary beam measurements 96
4.3.5 HiRA crystals 104
4.3.6 HiRA beam tests 105
4.4 Electronics 110
4.4.1 Application Specific Integrated Circuit (ASIC) 111
4.4.2 HiRA electronics 114
4.5 Mechanical 116
4.5.1 Electronics structure 118
4.5.2 Supporting structure 119
4.5.3 Pin source design 121
4.6 Calibrations using pin source 123
4.7 Particle identification 125

5 Beam tracking detectors and the full experimental setup 129
5.1 Introduction 129
5.2 Beam measurements using Parallel Plate Avalanche Counters (PPACs) 129
5.3 Micro Channel Plate detectors 132
5.3.1 MCP design 132
5.3.2 Position resolution 136
5.3.3 Timing resolution 139
5.3.4 Efficiency & counting rate 140
5.4 The full experimental setup 142

6 Summary and future work 147
6.1 Summary 147
6.2 Future work 149
6.2.1 ^{65}As Measurement 149
6.2.2 Measurements beyond the proton drip-line 149
6.2.3 Other reactions 149
Bibliography 151

List of Figures

1.1 Chart of the nuclides 2
1.2 The general path of the s-process 3
1.3 The energy production with respect to temperature for the pp chain and the CNO cycle. The Sun is shown here as a reference 5
1.4 Schematic view of binary star system with the center of mass and the Roche Lobe showing. 7
1.5 Artist representation of binary system with accreting neutron star . . 9
1.6 X-ray bursts event taken from GS 1826-24 10
1.7 General path of the rp-process 12

2.1 Richardson Extrapolation example 30
2.2 The Jacobian matrix $\partial\mathbf{f}/\partial\mathbf{y}$ used in GAMBLER 32
2.3 Demonstration of the variable time stepping used in GAMBLER . . . 34
2.4 Nuclei used in GAMBLER calculations 35
2.5 Temperature during an X-ray burst for three different initial temperatures 37
2.6 Temperature of X-Ray burst for different starting temperature with a small offset applied to align ignition times 37
2.7 Temperature profile of X-Ray burst for different mass accretion . . . 39
2.8 Burst description for an accretion rate $\dot{m}/\dot{m}_{edd} = 0.01$ 40
2.9 Burst description for $\dot{m}/\dot{m}_{edd} = 0.03$ 41
2.10 Burst description for $\dot{m}/\dot{m}_{edd} = 0.10$ 42
2.11 Burst description for $\dot{m}/\dot{m}_{edd} = 0.30$ 43
2.12 Abundances of nuclei in the ^{64}Ge region 45
2.13 Ratio of the ^{64}Ge$(p,\gamma)^{65}$As to the ^{65}As$(\gamma,p)^{64}$Ge rate as a function of the Q-value 46
2.14 Temperature profile for burst with different extreme ^{65}As$(\gamma,p)^{64}$Ge reaction rates from the Q-value 47
2.15 Mass fraction of waiting point nuclei for two extreme ^{65}As$(\gamma,p)^{64}$Ge reaction rates 48

3.1 Lab Vs. Center of Mass Angle 53
3.2 Lab frame kinematics 54
3.3 Cross section for ^{65}Ge(p,d)^{64}Ge at 60 MeV/u in the center of mass and lab frame 55
3.4 Deuteron energy Vs. lab frame angle from ^{66}As$(p,d)^{65}$As at 60 MeV/u 56

3.5 DE vs. TOF histogram showing simulated fragmentation beams for ^{66}As and ^{65}Ge 58
3.6 Mass peak resolution from target thickness only 62
3.7 Deuteron energy resolution vs mass resolution 65
3.8 Deuteron energy Vs. lab angle at low energy 66
3.9 Demonstration of kinematic broadening effect 67

4.1 Two configurations for HiRA. On the left HiRA is configured at forward angles for transfer reactions or breakup reactions. On the right HiRA is configured for elastic scattering near 90° in the lab. 73
4.2 Each HiRA telescope contains 2 silicon strip detectors and 4 CsI(Tl) crystals as shown here 75
4.3 The silicon DE frame for HiRA 76
4.4 The silicon DE frame for HiRA 77
4.5 Picture of the front side of an E detector 80
4.6 Picture of the back side of an E detector 81
4.7 Picture of the front side of a DE detector 81
4.8 Picture of the back side of a DE detector 82
4.9 Energy spectrum of the ^{228}Th alpha source on a single strip on the front of an E detector. The red triangles are locations of peaks found by the peak finding function. The colored lines on 5 of the eight peaks are Gaussian fits. 85
4.10 Histogram of energy resolution for all strips on all E an DE detectors 86
4.11 Side view and front view of a HiRA crystal, light guide and photo-diode assembly. The two inner sides of the crystal are cut perpendicular to the front and the rear faces of the crystal and the two outer sides of the crystal are cut at an angle of 5.3° from the perpendicular in order to back the active area of the silicon detectors when the telescope are placed at a distance of 35 cm. 87
4.12 Test configuration for the HiRA CsI crystals inside the scanning chamber with a collimated ^{241}Am α source 92
4.13 The variation of the light output over the face of the detector is show here as a percent deviation from the mean (S_{ij} as defined in Equation. 4.1). Here neighboring pixels are separated from each other by 3 mm in both x and y directions. This result is obtained using 5.5 MeV alphas from a ^{241}Amsource. 93
4.14 Test configuration for the HiRA CsI crystals. In the case of the test at the Texas A&M facility, the silicon detector was stationary with respect to the beam line and the crystals were wrapped separately. In the case of the tests performed at the NSCL, the silicon detector moved with the crystals and the crystals were wrapped as shown. 96

4.15 Relative comparisons of the light outputs from the eight test crystals. The light output of the HiRA crystals were selected to be within 15% of the light output of test crystal 6. These results were obtained with the 220 MeV α beam; the same results are obtained for the deuteron beam. The error bars are estimated from the reproducibility in the relative light output observed after recoupling the test crystals to the photo-diode and its associated electronics. 98
4.16 S_{ij} obtained for the alpha and deuteron beams for CsI 4 and 6 99
4.17 Correlation between the slope parameters obtained via the alpha source test and those obtained via the 220 MeV alpha beam test (solid points) and the 110 MeV deuteron beam test (open points). The diagonal dashed line represents a trend-line with a slope of 0.5. The region between the two vertical dotted lines represents the acceptance criteria for HiRA crystals. 100
4.18 D_{ij} for crystals 4 & 6 from alpha and deuteron beams 102
4.19 Left panels: crystal 4 with large non-uniformity. Right panels: crystal 6 with small non-uniformity. Bottom panels: Results for 110 MeV deuterons. Top panels: Results for 220 MeV alpha particles. In all panels, the dotted lines are the uncorrected energy spectra. The dashed lines are the spectra corrected with the linear correction for the light output non-uniformities. The solid lines are spectra for particles that enter into one randomly chosen pixel in the detectors. The dot-dash line is the crystal spectra corrected using the smoothing algorithm. . 103
4.20 Non-uniformity values S_{ij} for HiRA crystals 8 (left side) & 9 (right side) for the indicated beam particles from the CCF at the NSCL. Each pixel is separated in both x and y directions from its neighbor by 2 mm. 107
4.21 Non-uniformity values S_{ij} for HiRA crystals #8 (left side) & 9 (right side) for ^{6}Li and ^{7}Be 108
4.22 Scaling factor α, which describes the non-uniformity of specific isotopes with respect to that for ^{6}Li at E = 26 MeV/A for various particles and energies. By construction, we have a value of $\alpha = 1$ at $AZ^2/E = 0.34$ corresponding to the ^{6}Li fragmentation beam. The line is the fit to the non-linear term in Equation 4.8. 110
4.23 Block diagram of the HiRA ASIC 112
4.24 Picture of the HiRA chipboard. There are two ASICs on this board in the middle of the board. Below the board is a 4 channel prototype ASIC with the cover off exposing the actual chip inside the packaging. A US quarter is displayed next to it for size reference. 113
4.25 Oscilloscope trace of motherboard energy signals 116
4.26 Technical drawing of a HiRA detector box 117
4.27 Image of a motherboard inside its shielding box. Also shown are the cooling bar configuration designed to keep the ASICs cool in vacuum. 119
4.28 3-D rendering of a HiRA tower unit 120
4.29 3-D rendering of the entire HiRA system 121
4.30 Image of the front part of a HiRA telescope 122

4.31 Image of the α source frame used to calibrate the E detector without removing the DE detector. Extra pins are shown on the right. 123
4.32 2-D hit pattern for α particles from a pin source inserted between the DE and E detectors. 124
4.33 Raw energy spectrum for strip EF_{16} gated on pixel 16-16 125
4.34 Profile histogram for two strips on the front surface, EF_{23} and EF_{29} vs the calibrated EB_{16} Strip 126
4.35 Profile histogram for two strips on the front surface, EF_{23} and EF_{29} vs the calibrated EB_{16} strip after cross calibrations from back strip . . . 126
4.36 Particle identification plot using EF vs CsI 127
4.37 Particle identification plot using DE vs EF 128

5.1 Schematic design of a Micro Channel Plate 133
5.2 View of chevron style MCPs 133
5.3 Schematic design of MCP setup 135
5.4 Spectrum of MCP mask calibration 138
5.5 Time of flight spectrum between a MCP and a surface barrier detector 139
5.6 Simulated time spectrum for a cocktail beam containing ^{66}As 140
5.7 Image of the MCP setup in the 92" chamber 141
5.8 The NSCL cyclotrons and the A1900 fragment separator 144
5.9 The S800 Spectrograph 145
5.10 S800 Target Chamber with HiRA and MCPs in it 146

Images in this dissertation are presented in color

List of Tables

1.1 The approximate Main Sequence lifetime for stars of various mass . . 6

2.1 Ignition conditions used by GAMBLER 38
2.2 Half-lives for waiting point nuclei 44

3.1 Simulated resolution effect from target energy loss 63
3.2 Simulated resolution effect from deuteron energy measurement 64
3.3 Simulated resolution effect from position resolution in HiRA 67
3.4 Simulated resolution effect from position resolution of MCPs 68
3.5 Simulated resolution effect from total reaction angle 69

4.1 The energy resolution for each peak in 4.9 given raw and after subtracting electronic noise.The α energy is given in MeV and the FWHM are given in keV 85
4.2 Crystals used in testing 90
4.3 S_{rms} from alpha scans on all 8 test crystals 94
4.4 Linear fit parameters for the test crystals determined from α source scanning, α beam measurements, and deuteron beam measurements. . 95

5.1 MCP efficiency results for various beam rates 142

Chapter 1

Introduction

1.1 Motivations

In 1920 Sir Arthur Eddington proposed the fusion of hydrogen into helium as the source of the Sun's energy. This idea was not taken seriously until 1939 when Hans Bethe described the CNO cycle as a way of producing helium from hydrogen [1]. These early connections between nuclear physics and astronomy were solidified by a series of events in the 1950's. In 1954 Fred Hoyle claimed the amount of carbon in the universe requires there to be a resonant state in ^{12}C at around 7.7 MeV allowing three alpha particles to form one ^{12}C nucleus. In 1957 Cook, Fowler, Lauritsen, and Lauritsen discovered this state at 7.654 MeV [2]. With this measurement laboratory based nuclear astrophysics began. In 1957 Burbidge, Burbidge, Fowler, and Hoyle (B^2FH), wrote a detailed description of the synthesis of elements in stars [3]. During that same year, A.G.W. Cameron independently published similar findings [4]. Their works outlined nucleosynthesis processes that are believed to occur in the cosmos, and that are responsible for the synthesis of the elements.

Over the past 50 years nuclear astrophysicists have focused much attention on the elementary nuclear processes relevant to element production. Early work focused on slow processes that take place close to the valley of stability because such nuclei could

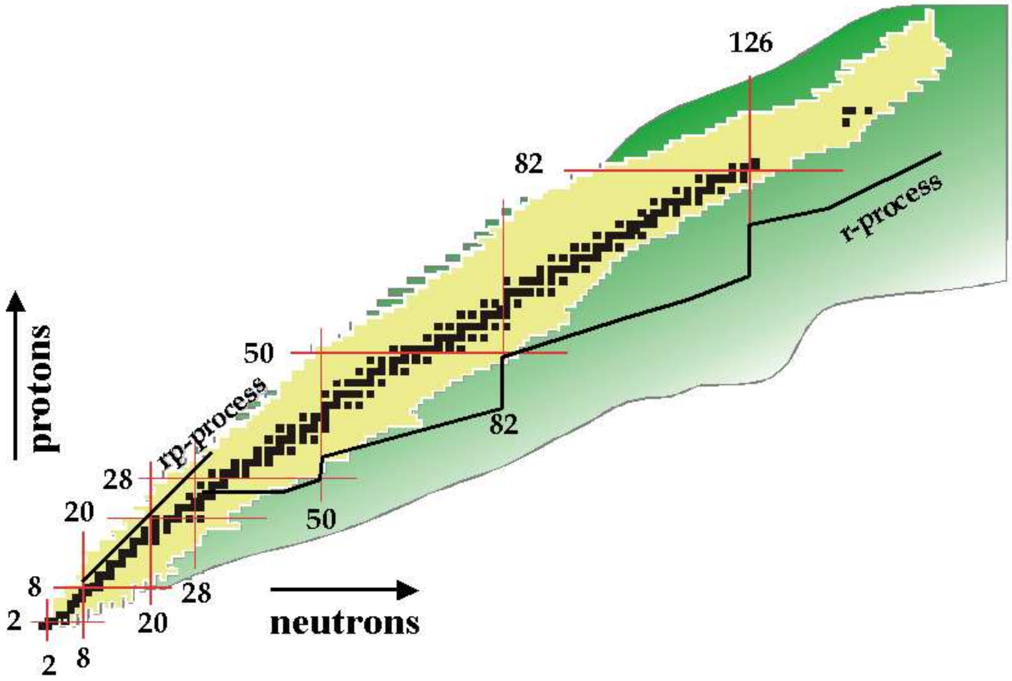

Figure 1.1: Chart of the nuclides

be produced with stable beams and targets. With the advent of rare isotope beams, explosive processes that occur far from beta stability can be investigated.

Figure 1.1 is a representation of the nuclear landscape. The horizontal axis is the neutron number N, and the vertical axis is the proton number Z. Each isotope of a given element is represented by one square. The black squares represent stable nuclei, the yellow region represent nuclei that have been observed, and the green region is the region where nuclei are believed to exist but have never been observed. The general path of two important processes for explosive nucleosynthesis, the r-process, and the rp-process, are shown as black lines on opposite sides of the valley of stability.

The two primary processes described in the early works of (B^2FH) and Cameron to make heavy elements were the s-process and the r-process. The s-process is an acronym for slow neutron capture where stable nuclei capture neutrons and then beta decay back to stability. Figure 1.2 shows a detailed description of the path of the s-process occurring in the region between Iron and Zirconium. The horizontal axis is the neutron number N, and the vertical axis is the proton number Z. Only stable

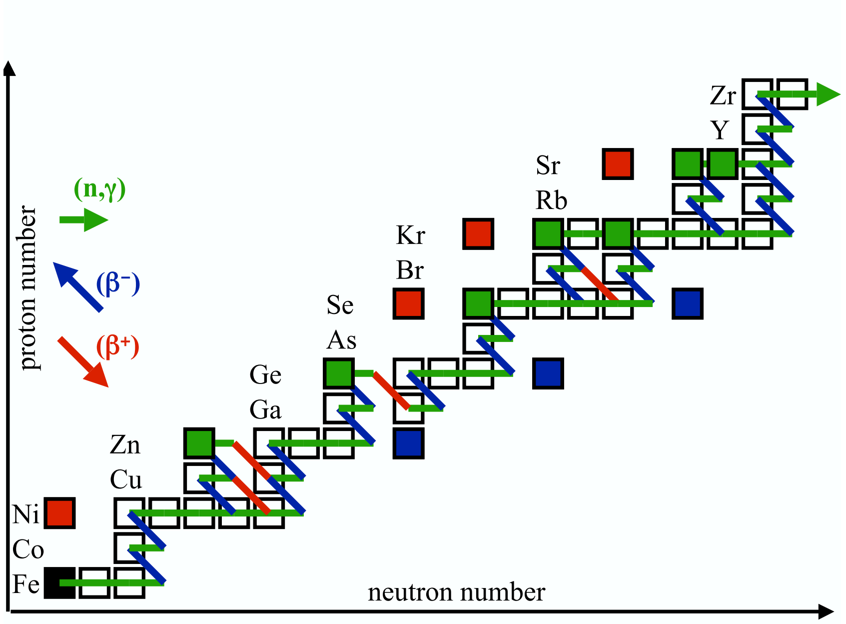

Figure 1.2: The general path of the s-process

isotopes are shown. The lines connecting these stable isotopes represent the path. The green lines represent (n, γ) reactions, the blue and red lines represent β^- and β^+ decays. The path of the s-process involves nuclear species that remain close to the valley of stability. In contrast, the r-process, or rapid neutron capture process, occurs much farther from stability on the very neutron rich side of the valley of stability as shown on Figure 1.1. It is characterized by a rapid capture of many neutrons followed by beta decay.

The timescales and astrophysical environments for these processes are very different from each other. The s-process is expected to occur over thousands of years within the helium burning shells of red-giant stars. In contrast, the r-process is expected to occur over time scales on the order of seconds. The sites of the r-process are still unknown, but could include type II supernova or the merger of two neutron stars.

In this dissertation, I will focus on similar phenomena that is believed to occur on the proton rich side of the valley of stability, the rapid proton capture, or rp-process. The general path of this process is indicated by the black line on the neutron deficient side of the valley of stability shown in Figure 1.1. This process is important to the explanation of observed X-ray bursts. These bursts are believed to be the consequence of thermal nuclear explosions on the surface of neutron stars in close binary star systems. The rp-process in such systems follows a pathway on the proton-rich side of the valley of stability that can be studied only by using proton-rich rare isotope beams. Key nuclei to be studied are the waiting point nuclei where the burning process slows down. From the astrophysical point of view, the most important property of such nuclei are their masses because their influence on the burning rate is exponential. Resonance energies are also important for determining the pathway, but require masses to determine the energy where resonances are important.

1.2 Astrophysics

In this section the life cycle of a star is briefly described. A star is “born” from a gravitationally contracting gas. As the gas contracts the density and temperature increase. This contraction leads to enhanced thermal nuclear reactions at the center of the collapsing protostar. Eventually, the energy released from such nuclear reactions is sufficient to balance the pressure from gravitational collapse, thereby creating a star in quasi hydrostatic equilibrium. Hydrogen burning continues at the core allowing its sustained existence.

Stars that burn hydrogen in their cores constitute the largest fraction of observed stars. They display a common luminosity-temperature relationship by which they can be identified as “Main Sequence” stars. Two basic processes contribute to this burning: the pp chain that burns hydrogen to make ^{4}He, and the CNO cycle that uses carbon as a catalyst to make ^{4}He. The pp chain happens via the reactions $p(p, e^{+}\nu)d$, followed by $d(p,\gamma)^{3}$He, and then primary ^{3}He(^{3}He$, 2p)^{4}$He fusing four protons into ^{4}He. The CNO cycle is more complicated. The basic path is ^{12}C$(p,\gamma)^{13}$N, ^{13}N$(e^{+}\nu_{e})^{13}$C, ^{13}C$(p,\gamma)^{14}$N, ^{14}N$(p,\gamma)^{15}$O, ^{15}O$(e^{+}\nu_{e})^{15}$N, and ^{15}N$(p,^{4}$He$)^{12}$C. In order

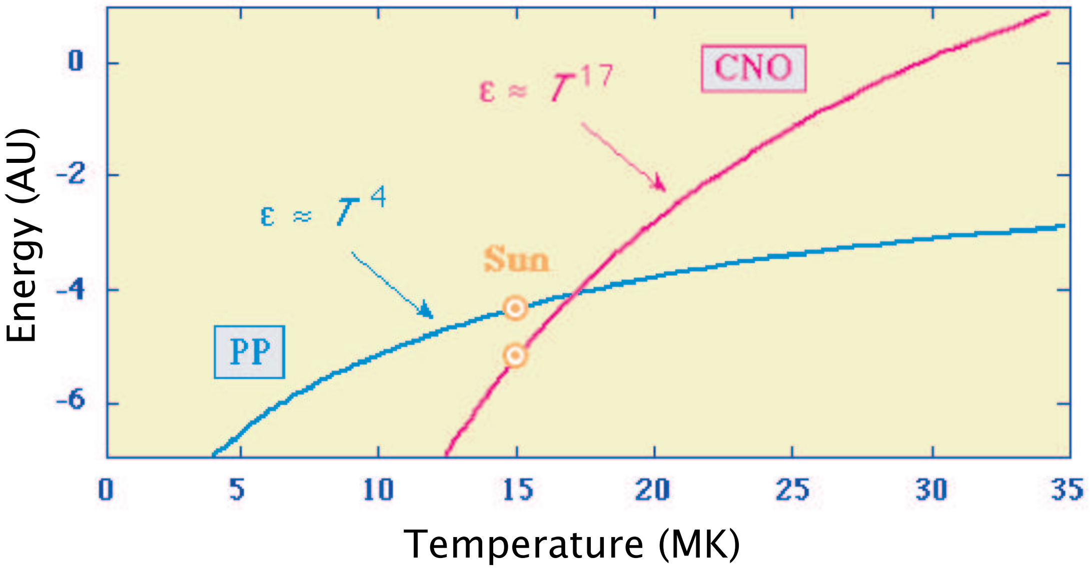

Figure 1.3: The energy production with respect to temperature for the pp chain and the CNO cycle. The Sun is shown here as a reference

for the CNO cycle to occur there must be carbon in the star.

As little, or no carbon was produced in the Big Bang, it is believed that the carbon found today in most stars originated in much heavier stars that burned quickly and distributed their ashes in the past via stellar winds or violent explosions.

Figure 1.3 shows the energy production as a function of temperature for both the pp chain and the CNO cycle. The dependence on energy increases as the 4th power of temperature for the pp chain. In the case of the CNO cycle, energy increases as the temperature to the 17th power. The Sun symbols on Figure 1.3 represents the contribution to energy production from the pp and CNO chains in our Sun, which is characterized by a core temperature of 15 Million Kelvin. As can be seen in the figure, the dominant energy production for stars with the mass of the Sun is the pp chain.

The greater the mass of the star the larger the pressure from gravity resulting in higher temperatures at the core. Therefore the internal temperature of the star is strongly correlated with its mass. More massive stars burn hydrogen more rapidly. Table 1.1 shows the Main Sequence lifetime for various mass stars, expressed in units

Table 1.1: The approximate Main Sequence lifetime for stars of various mass

Mass ($M_\odot$)	Time on Main Sequence (10^6 years)
25	3
15	15
3	500
1.5	3,000
1.0	10,000
0.75	15,000
0.5	200,000

of solar masses, $M_\odot$, where 1 $M_\odot = 1.989 \times 10^{33}$ g.

After most of the hydrogen in the center has been fused into helium it can no longer sustain the original gravitation pressure and the core begins to contract again. As the core contracts it will begin to burn helium into carbon via the triple alpha process. The region above the core will heat up and begin to burn hydrogen. The outer layers of the star will expand dramatically. When the sun begins burning helium it will expand from its current size all the way out to the orbit of earth. This stage of stellar burning is known as the Red Giant phase.

For stars with a mass below 4 $M_\odot$, The Red Giant phase will last about 10^8 years, and when this is done nuclear burning process within the star cease. The temperature in the core never becomes high enough to burn carbon, the star instead collapses until electron degeneracy pressure stops the collapse. This compact object is held up by electron degeneracy pressure and is known as a white dwarf.

For stars with a mass above 4 $M_\odot$ additional burning phases can occur as the core collapses and heats up. For stars with an initial masses above 25 $M_\odot$ the temperature in the core will reach a point were oxygen, neon, magnesium, and silicon can fuse leading to an iron core. Fusion involving iron does not produce a net energy gain as ^{56}Fe is the most tightly bound nucleus. It is therefore not energetically favorable to fuse into heavier elements.

Without an energy input from burning, the Iron core will begin to collapse. As

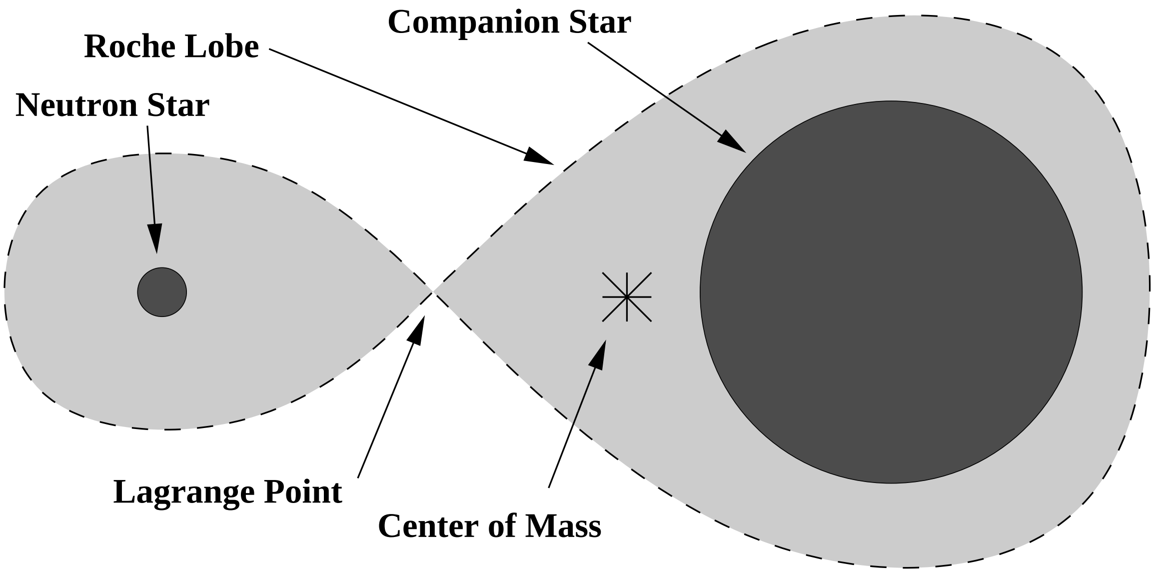

Figure 1.4: Schematic view of binary star system with the center of mass and the Roche Lobe showing.

the Iron core collapses, its temperature increases and can reach 5 GK where photodisintegration of the Iron into protons and neutrons can occur. As the density increases, electron capture on the protons begins to produce a strongly neutron rich core, a process known as neutronization. The density in the center increases to 4–5 times the saturation density of nuclear matter, where the repulsive nuclear matter equation of state at high density halts the collapse. It is believed that a shock wave then propagates outward. It is currently not possible to fully simulate such astrophysical events but such events are believed to be the site of type II supernovae. Such supernova have been observed to, and in some cases, such as the Crab nebula, leave behind a compact object known as a neutron star. In principle such explosions could produce a black hole instead, however this work will focus on the neutron star remnant.

Many neutron stars have now been identified. Typically, observations of the masses of neutron stars in binary systems are consistent with a mass of about 1.4 $M_\odot$. For certain reasonable nuclear equations of state, a radius of about 10 km is expected.

It is believed that about 60% of stars are born into binary systems with another star, based on observations and our understanding of stellar creation. Naturally, the two stars will orbit about their common center of mass. Figure 1.4 shows a schematic view of a binary system containing a neutron star and a companion star. An equipotential surface is shown by the dashed line representing the region where material is gravitationally confined to the neutron star or to its companion star but cannot travel from one to the other. This boundary is called its Roche Lobe. The point where the lobes of each star touch is the inner Lagrangian point, where the gravitational force from one star balances the other.

If one of the stars in a binary system was a massive star with a mass of 25 $M_\odot$ or greater, and the other was less massive, the heavier star could go through all its burning stages and explode as a supernova during the Main Sequence lifetime of the companion star. Thus one would have a binary system consisting of a 1.4 $M_\odot$ neutron star and a Main Sequence star. When the lower mass companion star completes its Main Sequence lifetime and begins to burn helium and expand dramatically during its Red Giant phase, hydrogen and helium rich matter from the surface of the large cool Red Giant will flow through the inner Lagrangian point and begin to orbit the neutron star. As both stars are spinning and orbiting, the orbiting matter will initially form a disk about the neutron star and matter in the disk will begin to accrete onto the neutron star surface. An artistic representation of the binary system with this disk about the neutron star is shown in Figure 1.5.

The accreted matter, mostly hydrogen and helium, falls on the neutron star releasing gravitational potential energy. The gravitational energy released by accreting matter of mass m_u on the star of mass M and radius R is given approximately by:

$$E = \frac{GMm_u}{R} \tag{1.1}$$

This energy released corresponds to about 200 MeV/u for a mass of 1.4 $M_\odot$ and a radius of 10 km. This gravitational energy is believed to be responsible for the

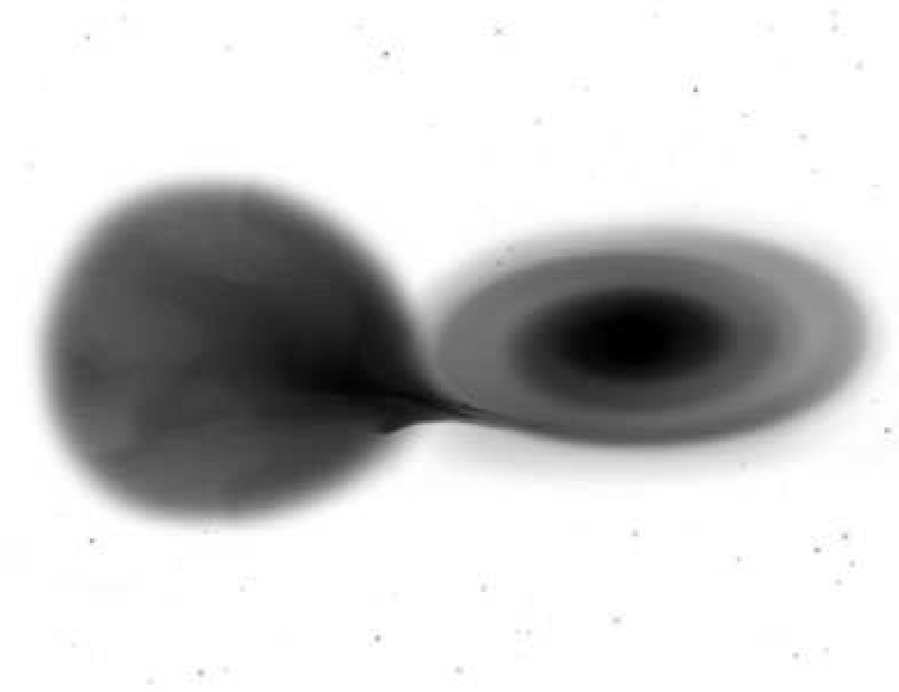

Figure 1.5: Artist representation of binary system with accreting neutron star

persistent X-ray flux from the star. The material on the crust can become very proton rich from the influx of hydrogen from its companion. As this hydrogen rich matter settles deeper into the crust of the neutron star, the temperatures and pressures of the crust will rise. After accumulating sufficient material, hydrogen will ignite at some depth in the crust, and the resulting thermal nuclear conflagration will spread and engulf the entire surface of the neutron star. This nucleosynthetic process (rp-process) is a “rapid” proton capture process. The rp-process leads to a sudden burst of energy which may be observed astronomically as an X-ray burst. X-ray bursts from the source 3U 1820–30 were first discovered by J.Grindlay *et al.* in 1976 using the Astronomical Netherlands Satellite (ANS) [5]. Currently there are about 40 known X-ray bursters. These sources show a wide variety of burst characteristics. Typical bursts last for about 10–100’s seconds with X-ray energy outputs of about $10^{36} - 10^{38}$ ergs/s. To put this in context, a Main Sequence star has an energy output between $10^{33} - 10^{35}$ ergs/s. The recurrence time is hours to days with some occurring regularly and others quite irregularly.

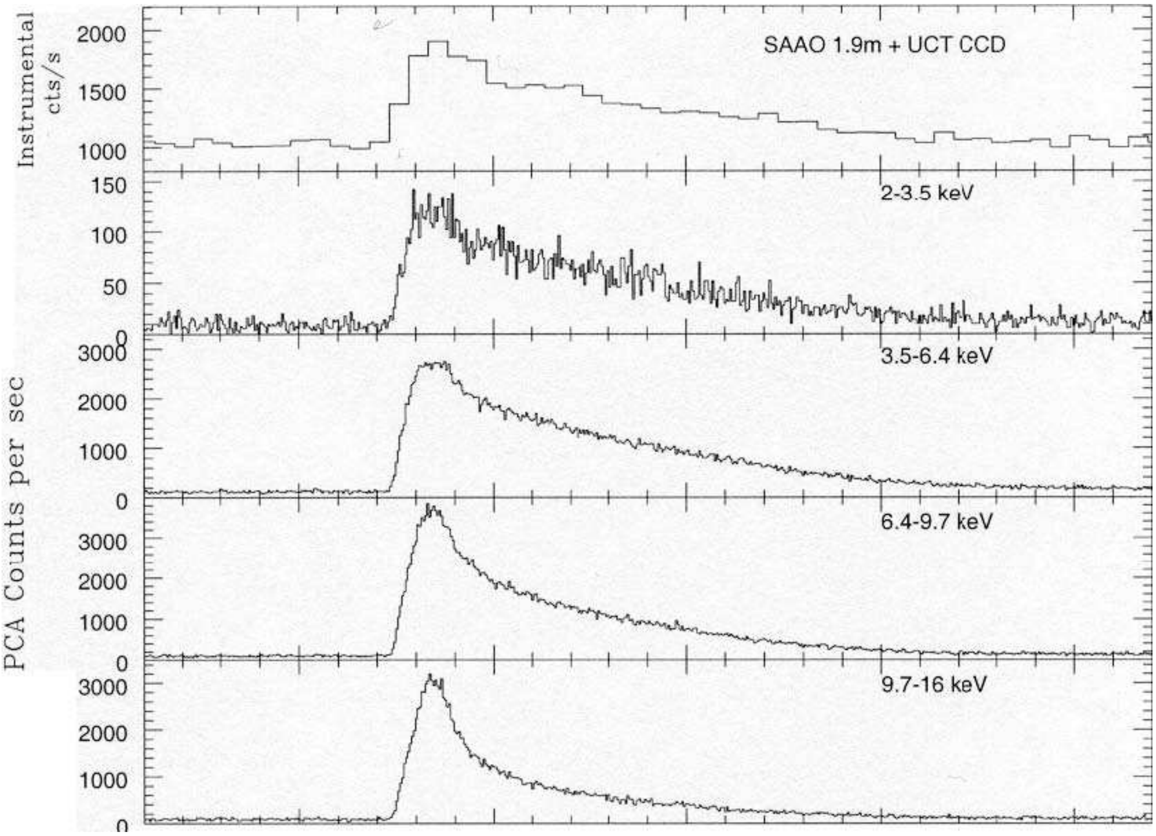

Figure 1.6: X-ray burst event taken from GS 1826-24

Figure 1.6 shows an observed X-ray burst from GS 1826-24. The top graph is from the SAAO optical telescope with the lower graphs from the RXTE satellite in different frequencies. The horizontal axis ticks are in 10 second intervals.

1.3 Nuclear Physics of the rp-process

There are many interesting properties about neutron stars such as the range of masses for which neutron stars can be stable, their possible radii, their magnetic fields, their rotational frequencies, their internal compositions, and their internal structure for all parts in the interior from the core all the way to the atmosphere. Nuclear physics is relevant to all these issues. The density of matter in the center of the star is believed to be well above ($\sim 9\times$) nuclear saturation density. The equation of state for neutron rich nuclear matter therefore governs the internal structure and stability of the neutron star.

In this dissertation I am concerned with reactions occurring much closer to the surface of the star where the rp-process dominates. Generally, the rp-process path is governed by the balance between proton capture, photo-disintegration, and beta decay. Because of the dominance of proton captures, the pathway occurs on the proton rich (neutron deficient) side of the valley of stability.

Figure 1.7 shows a possible scenario for the basic reaction network that is followed during a simulated X-ray burst. As matter accretes onto the surface of the neutron star, steady state CNO burning occurs. Ignition may occur when the conditions begin to favor the triple alpha reaction. If this occurs the temperature can rise enough to initiate breakout of the CNO cycle. A series of (α, p), (p, γ) reactions, shown by the green path in Figure 1.7, then occur starting on nuclei around ^{14}O, and continuing on to ^{41}Sc. This sequence of reactions is known as the αp-process. The Coulomb barrier will prevent α-capture from continuing beyond ^{41}Sc. If there is sufficient hydrogen remaining in the stellar crust (p, γ) reactions will proceed rapidly, until (γ, p) photo-

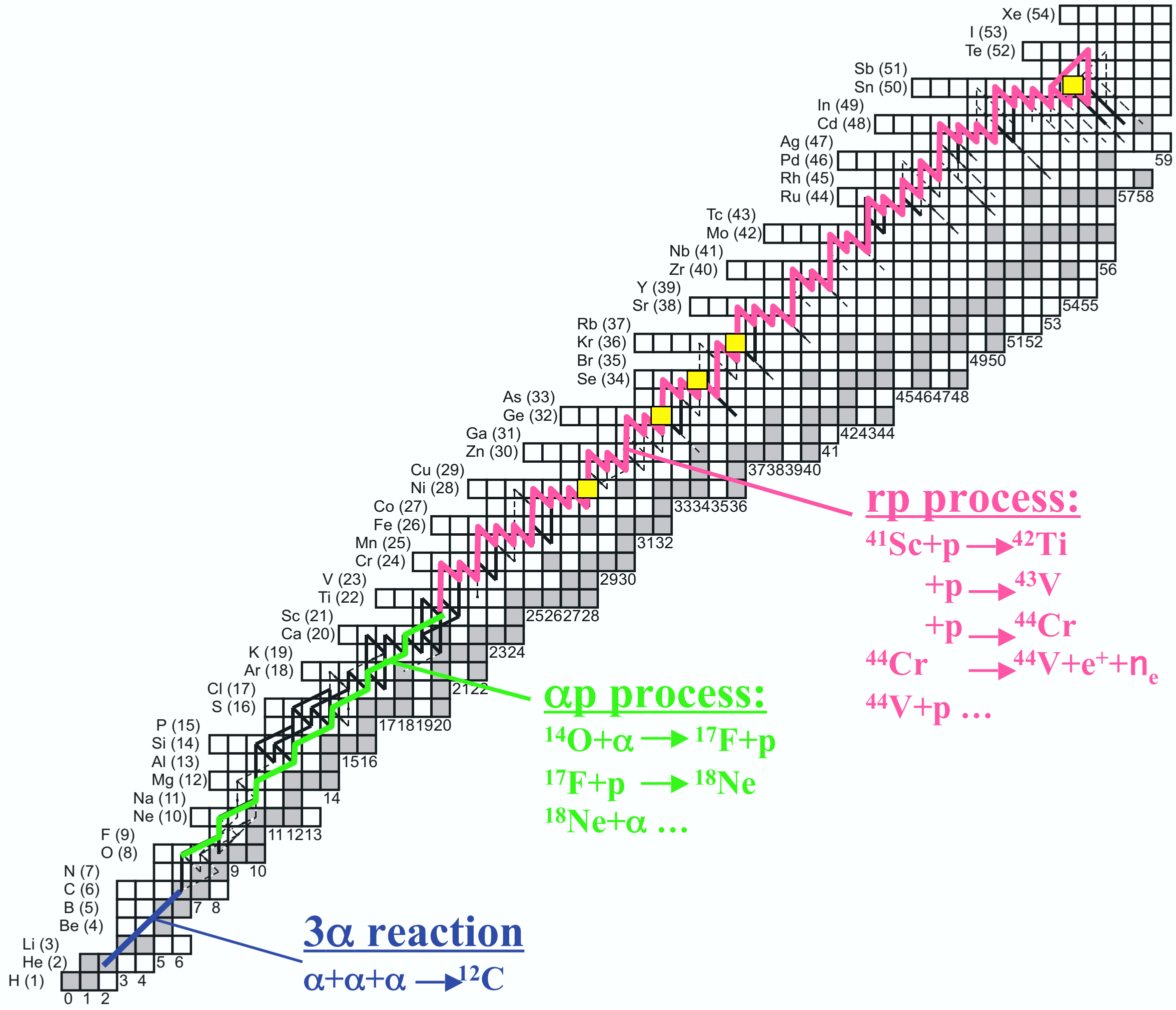

Figure 1.7: General path of the rp-process

disintegration reaction rates are significantly larger than the (p,γ) reactions rate. This will stop the rapid proton capture until a beta-decay occurs that brings the path closer to stability where the (p,γ) reactions can continue. The resulting proton captures and beta decays shown in pink in Figure 1.7 are known as the rp-process. For nuclei on the rp-process pathway for which the (γ,p) reaction rate is significantly larger then the (p,γ) reaction rate, and the beta-decay half-life is long, a buildup in abundance will occur. Cessation of reactions at such nuclei reduce the energy generation and allows the environment to cool. Such nuclei are known as waiting point nuclei; their properties determine the ultimate termination or continuation of the rp-process. Some important rp-process waiting point nuclei are shown as yellow squares in Figure 1.7.

The proton separation energy is defined as:

$$S_p = -(M(Z,N) + M(Z-1,N) + M_p)c^2 \tag{1.2}$$

where c is the speed of light and $M(Z,N)$ is the mass of the nuclei with Z protons and N neutrons. The proton separation energy is not only important for defining the limits of stability, but it plays a critical role in the rp-process. At waiting point nuclei both the (p,γ) and (γ,p) reaction rates are large, which puts the nuclei involved in a state of nuclear statistical equilibrium with each other. In this situation the relative abundances are entirely determined by the equilibrium mass described by the Saha equation:

$$\frac{n_i n_p}{n_j} = \frac{g_i g_p}{g_j}\left(\frac{m_i m_p}{m_j}\right)^{3/2}\left(\frac{k_b T}{2\pi\hbar^2}\right)^{3/2} exp(-S_p/k_b T) \tag{1.3}$$

where n_i, n_j,and n_p represent the number density for the nuclei i, j and protons. The partition functions for nuclei i, j,and p are given by g_i, g_j, g_p. The corresponding masses are given by m_i, m_j, and m_p. The temperature is given by T. k_b is the Boltzmann constant and S_p is the proton separation energy. This exponential dependence on the proton separation energy, and hence the relevant nuclear masses, makes it extremely important to know such masses to high accuracy. As seen in Figure 1.7, the rp-process occurs away from the valley of stability, where the experimental data relating to the relevant reactions becomes sparse. Many of the masses of key waiting point nuclei along the rp-process have not been measured. Systematic errors in mass model extrapolations in this region are on the order of 300 keV. It is therefore critical to measure the precise mass of nuclei involved in key waiting point reactions.

1.4 Major Focuses of Dissertation

The initial plan for this thesis was to perform mass measurements of the key waiting point nuclei involved in the rp-process in the mass range $A = 64 - 74$. Unfortunately, difficulties in instrumenting such experiments with very high quality experimental tools made the time needed to construct the equipment and perform the high precision experiments for mass measurements extend beyond the duration of one thesis. Thus the dissertation focus became the development of the necessary detectors and the careful design of an experiment capable of performing these measurements. A separate theoretical effort was undertaken to identify the relevant nuclear data required to the rp-process.

Concerning the experimental part of the thesis, there were two separate tasks. The first was the technical development of a new charged particle array known as the High Resolution Array (HiRA), and other devices needed for tracking the rare isotope beam. The second part was to figure out the optimum way to perform the experiments, taking into account the constraints on beam quality, beam rate, detector rate capabilities, so as to achieve absolute mass measurements of the required accuracy.

1.5 Organization of Dissertation

The chapters to follow this are organized in the following way. In Chapter 2 the astrophysical modeling of rp-process nucleosynthesis will be described in detail. This serves as the primary motivation for the experiments discussed later. Chapter 3 will detail the simulations and design work as well as a detailed description of the various aspects of the measurements and how the final resolution will be affected by them as well as potential systematic errors. Chapter 4 focuses on the development of HiRA. One of the scientific justifications for building HiRA was the performance of mass measurements for the rp-process as described within this thesis, however it was not built solely for this reason. A description of how HiRA will be used in the mass measurements is given in Chapter 5. The final chapter, Chapter 6 discusses the results from test runs and presents an outlook of the future campaign of experiments.

Chapter 2

rp-Process Calculations

2.1 Introduction

In order to understand the details of the rp-process, which is believed to occur on the surface of neutron stars in binary systems, one must rely on computer models as a tool. Computer models are limited in what they can do and are only as good as the physics implemented in them. They are also limited by the computational time required for large models. In order to make models which are computationally feasible, yet scientifically useful, approximations and simplifications are made to the system which is being modeled.

In this work GAMBLER is used to study details of the rp-process. GAMBLER stands for **G**eneral **A**bundance **M**anipulator **B**ased on **L**ocal **E**volution of **R**eactions. It was developed specifically to study the effects detailed nuclear properties of nuclei in the region above ^{56}Ni, have on the rp-process or more specifically, on X-ray bursts which have been discussed in Section 1.2.

In this chapter the physics implemented in the GAMBLER model will be described. This will be followed by a description of the results from calculations for several different accretion rates, which lead to different nuclear-burning ignition conditions. After this additional calculations which demonstrate the importance of performing experimental measurements of key nuclear physics properties in the mass region just above ^{56}Ni are shown.

2.2 Nuclear Physics in GAMBLER

Of primary interest in modeling thermal nuclear burning is the change in the abundances of all nuclei involved due to nuclear reactions. To start with, the abundance is defined in a way that is independent of volume or density.

$$Y_i = \frac{X_i}{A_i} \tag{2.1}$$

where X_i is the mass fraction of nuclei i and A_i is the mass number for i. This definition of abundance is unit-less and invariant under compression. The abundance of nuclei i is considered only for the ground state. Resonant state abundances are not considered. The number density can then be written as

$$n_i = \frac{X_i \rho}{m_i} \tag{2.2}$$

Where ρ is the mass density in (g/cm^3), and m_i is mass which can be written as $m_i \approx A_i \cdot m_u$ where m_u is in atomic mass unit and is defined as $m_{^{12}\mathrm{C}}/12$. In CGS units $m_u = 1/N_A$, where N_A is Avogadro's number. With this the number density can then be written as

$$n_i = Y_i \rho N_A \tag{2.3}$$

If one considers a single binary reaction of the type $i + j \to k + l$, where i and j are not equal to k and l, the change in abundance of nucleus i (Y_i) is

$$\frac{dY_i}{dt} = -Y_i Y_j \rho N_A \langle \sigma \nu \rangle_{ij,kl} \tag{2.4}$$

Here $\langle \sigma \nu \rangle$ denotes the product of cross section and relative velocity averaged over the

Maxwell Boltzmann distribution of the astrophysical plasma. The minus sign is there because this reaction will destroy nuclei of type i, so the change in abundance will be negative. The quantity $N_A\langle\sigma\nu\rangle$ is often referred to as the astrophysical reaction rate. Equation 2.4 can be generalized to apply to all nuclei and all reactions giving the differential equation

$$\begin{aligned}\frac{dY_i}{dt} = &\sum_{k,l} N_i \frac{Y_k^{N_k}}{N_k!}\frac{Y_l^{N_l}}{N_l!}(\rho N_A)^{N_k+N_l-1}\langle\sigma\nu\rangle_{kl,ij} \\ &-\sum_{j} N_i \frac{Y_i^{N_i}}{N_i!}\frac{Y_j^{N_j}}{N_j!}(\rho N_A)^{N_i+N_j-1}\langle\sigma\nu\rangle_{ij,kl} \\ &+\sum_j Y_j \frac{ln(2)}{t_{1/2_{j\rightarrow i}}} - \sum_i Y_i \frac{ln(2)}{t_{1/2_{i\rightarrow j}}}\end{aligned} \tag{2.5}$$

where N_i, N_j, N_k, and N_l are the multiplicities of the nuclei i, j, k, and l respectively. The factorials in the denominator are included to avoid double counting when the reaction consist of like particles. The N_i before the first two terms of equation 2.5 accounts for the multiplicity of the nucleus i which are produced or destroyed in the reaction. The first two summations represent changes in abundance due to binary reactions as well as a few three body reactions like the triple-α reaction. The last two summations describe decay processes that will respectively create, or destroy nuclei of type i. Equation 2.5 for each nucleus included in the network make up a set of coupled ordinary differential equations.

The nuclear physics in Equation 2.5 is contained inside the reaction rate $\langle\sigma\nu\rangle$. When available, measured reaction rates are used, however many of the reactions involved have not been measured therefore one must rely on model calculations of these unknown reaction rates. These reaction rates are largely estimated by assuming that the reaction proceeds through a compound nuclear (CN) intermediate state. We break reaction rates into two parts, "resonant", for which the CN state widths and level spacing is much greater than k_bT and the CN widths are all less than the level spacing, and non-resonant for which this condition does not hold. The sum of these makes up the astrophysical reaction rate. For both cases, GAMBLER calculations employ standard reaction rate libraries that are widely available. Details of these rates are given in the following two sections.

2.2.1 Non-Resonant Reaction Rates

Non-Resonant rates were calculated using SMOKER [6], and more recently using NON-SMOKER [7]. Both are statistical model calculations based on the Hauser-Feshbach formalism. Reactions of the type (n, γ), (n, p), (n, α), (p, γ), (p, α), and (α, γ) are computed, along with their inverse reactions. Reactions of particles with charge higher than two are not considered to be important because the Coulomb barrier strongly reduces the chance of direct nuclear reactions at the astrophysical temperatures under consideration. For statistical model calculations, the key inputs are γ-transmission coefficients, particle transmission coefficients, the level density of excited states, and the mass. In this formalism the cross section is given by:

$$\begin{aligned} \sigma^{\mu\nu}(E_{ij}) &= \frac{\pi/(k_{ij}^2)}{(2J_i^\mu+1)(2J_j+1)} \sum_{J,\pi}(2J+1) \\ &\quad \times \frac{T_j^\mu(E, J, \pi, E_i^\mu, J_i^\mu, \pi^\mu) T_o^\nu(E, J, \pi, E_m^\nu, J_m^\nu, \pi_m^\nu)}{T_{tot}(E, J, \pi)} \end{aligned} \tag{2.6}$$

where $\sigma^{\mu\nu}$ represents the cross section for the reaction $i^\mu(j, o)m^\nu$ from the target state i^μ to the excited state m^ν. T represents the transmission coefficient, In this expression k^2 is the wave number for the incoming channel where $k_{ij}^2 = 2\mu_{ij}E_{ij}/\hbar^2$ for massive particles where E_{ij} is the center of mass energy and μ_{ij} is the reduced mass, J represents the spin, and E corresponds to the excitation energy with π being the parity of the intermediate compound nuclear state formed in the reactions. $T_{tot} = \Sigma_{\nu,o}T_o^\nu$ represents the total transmission summed over all channels. The astrophysical cross section σ^* is then given by

$$\sigma^*(E_{ij}) = \frac{\sum_\mu (2J_i^\mu + 1) exp(-E_i^\mu / k_b T^*) \sum_\nu \sigma^{\mu\nu}(E_{ij})}{\sum_\mu (2J_i^\mu + 1) exp(-E_i^\mu / k_b T^*)} \tag{2.7}$$

where k_b is the Boltzmann constant and T^* is the temperature of the astrophysical plasma. The summations are over the μ, the initial states, and ν, the final states. The astrophysical reaction rate is then calculated by integrating the cross section over the Maxwell-Boltzmann velocity distribution which represents the thermal motion of the nuclei within the astrophysical environment.

$$\begin{aligned} \langle \sigma^* \nu \rangle &= \langle \sigma \nu \rangle^* \\ &= \left(\frac{8}{\pi \mu} \right)^{1/2} \frac{1}{(k_b T^*)^{3/2}} \int_0^\infty E \sigma^*(E) exp \left(-\frac{E}{k_b T^*} \right) dE \end{aligned} \tag{2.8}$$

Using this expression for the stellar cross section, the reverse reaction rate can be calculated by using detailed balance. The reverse astrophysical reaction rate is defined as:

$$\begin{aligned} N_A \langle \sigma_m \nu \rangle^* &= \left(\frac{A_i A_j}{A_o A_m} \right)^{3/2} \frac{(2J_i + 1)(2J_j + 1)}{(2J_o + 1)(2J_m + 1)} \\ &\quad \times \frac{G_i(T^*)}{G_m(T^*)} exp\left(-Q/k_b T^*\right) N_A \langle \sigma_i \nu \rangle^* \end{aligned} \tag{2.9}$$

where A_i is the mass of nuclei i and Q is the forward reaction Q-value from the initial ground state to the final ground state. $G(T^*)$ is the temperature-dependent partition function normalized to the ground state target spin given by

$$\begin{aligned} (2J_i^o + 1) G(T^*) &= \sum_{\mu=0}^{\mu_m} (2J_i^\mu + 1) e^{-E_i^\mu / kT^*} \\ &+ \int_{E_i^{\mu_m}}^{E_i^{max}} \sum_{J^\mu, \pi^\mu} (2J^\mu + 1) e^{-\epsilon / k_b T^*} \rho(\epsilon, J^\mu, \pi^\mu) d\epsilon \end{aligned} \tag{2.10}$$

where ρ is level density and μ_m is the last experimentally known state.

From Equation 2.9, one can see the exponential dependence on the Q-value, which means the reaction rate depends exponentially on the masses. For reactions where the mass has not been measured a parameterization of the nuclear mass is used. For most reactions of astrophysical interest this statistical model approach can give accurate rates to within a factor of 2 [8].

2.2.2 Resonant Reaction Rates

If the level density is below about 5–10 MeV^{-1} in the region of the thermal peak energy distribution and k_bT is much less then the level spacing then a few resonant states can dominate the overall reaction rate. The general form for the cross section contribution due to a single resonance is given by the Breit-Wigner formula:

$$\sigma(E) = \pi \lambda\!\!\!^{-}{}^2 \frac{2J_r + 1}{(2J_p + 1)(2J_T + 1)} \frac{\Gamma_i \Gamma_j}{(E - E_r)^2 + (\Gamma/2)^2} \tag{2.11}$$

where $\pi \lambda\!\!\!^{-}{}^2$ represents a geometrical cross section, which is the maximum value the cross section can attain. J_r is the spin or the resonance state, J_p and J_T are the spins of the projectile and target, Γ_i and Γ_j are the partial widths for decay of resonance by emission of initial particles i and final particles j. Γ is the total width and E_r is the resonance energy.

The complete set of reaction rates from resonant and non-resonant calculations and measurements was compiled into a data base called REACLIB [6]. The REACLIB data base contains seven parameters for each reaction rates. The rate is given by:

$$rate = exp(a_1 + \frac{a_2}{t_9} + \frac{a_3}{{t_9}^{1/3}} + \frac{a_4}{{t_9}^{1/3}} + a_5 t_9 + a_6 {t_9}^{\frac{5}{3}} + a_7 ln(t_9)) \tag{2.12}$$

where t_9 is the temperature in (GK) and a_1–a_7 are fit parameters. For calculating inverse rates, the input file for each nuclei contains its partition function as a function of temperature. The partition function is calculated by a logarithmic interpolation.

The REACLIB rates are then modified by

$$rate_{rev} = \frac{\prod_o part}{\prod_i part} rate_{for} \tag{2.13}$$

where the product is taken over partition functions of all outgoing particles (o) and incoming particles (i) for the reverse reaction.

2.2.3 Screening Effects

In hot astrophysical environments the nuclei will often only be partly ionized which affects the astrophysical reaction rates. Screening of the nuclear charge by electrons can enhance the reaction rate of the neutral or partly ionized nuclei compared to that of bare nuclei. The electrons have the effect of lowering the coulomb barrier. Therefore, models of astrophysical plasma must take screening effects into account. The measured and calculated cross sections which have been discussed above are necessarily for bare reactions as screening depends on the composition, density, and temperature. In GAMBLER, screening effects are taken into account following the method used in References 9,10 by H.C.Graboske *et al.* The bare reaction rates are therefore modified by:

$$\langle \sigma \nu \rangle_{screened} = f \langle \sigma \nu \rangle_{bare} \tag{2.14}$$

where f is the scaling factor.

$$f = exp[H_{12}(0)] \tag{2.15}$$

where $H_{12}(0)$ can be written as

$$H_{12}(0) = k_b \eta_b \zeta_b {\Lambda_0}^b \quad \Lambda_0 = 0.188 \frac{\rho^{1/2}}{\bar{A}^{1/2}} {T_6}^{-3/2} \tag{2.16}$$

where $\bar{A}$ represents the average mass number. The value of each of these parameters depends on the screening conditions. For weak screening

$$b = 1 \quad k_b = \frac{1}{2} \quad \eta_b = \tilde{z} \quad \zeta_b = 2Z_1Z_2 \tag{2.17}$$

where

$$\tilde{z} = (\sum_i {Z_i}^2 Y_i \bar{A} + \sum_i Z_i Y_i \bar{A} \theta_e)^{1/2} \tag{2.18}$$

where θ_e is the electron degeneracy factor. For intermediate screening

$$b = 0.860 \quad k_b = 0.380 \tag{2.19}$$

$$\eta_b = \frac{\left\langle z^{3b-1} \right\rangle}{\tilde{z}^{3b-2} \, \bar{z}^{2-2b}} \tag{2.20}$$

$$\zeta_b = [(Z_1 + Z_2)^{1+b} - {Z_1}^{1+b} - {Z_2}^{1+b}] \tag{2.21}$$

For strong screening

$$b = 2/3 \quad k_b = 0.624 \quad \eta_b = \bar{z}^{1/3} \tag{2.22}$$

$$\begin{aligned} \zeta_b \;=\; & [(Z_1 + Z_2)^{5/3} - {Z_1}^{5/3} - {Z_2}^{5/3}] \\ & +0.316\bar{z}^{1/3}[(Z_1 + Z_2)^{4/3} - {Z_1}^{4/3} - {Z_2}^{4/3}] \\ & +0.737\bar{z}^{-1}[(Z_1 + Z_2)^{2/3} - {Z_1}^{2/3} - {Z_2}^{2/3}]/{\Lambda_0}^{2/3} \end{aligned} \tag{2.23}$$

The boundaries between weak, intermediate and strong screening are defined by Λ_{12} which is $H_{12}(0)$ for weak screening. If Λ_{12} is less than 0.1, weak screening is used. If it is greater then 0.1 and less then 2 intermediate screening is used. If it is above 5 then strong screening is used. Between 2 and 5 both strong and intermediate are calculated and the lower of the two are used. For a detailed description of screening effects see references 9,10.

2.3 Thermodynamics in GAMBLER

The motivation for writing GAMBLER was to better understand the dependency of the rp-process on nuclear properties, however a reasonable description of the environment in which the burning occurs is necessary as the change in abundance as defined in Equation. 2.5 depends explicitly on the density and the astrophysical reaction rates depend very strongly on the temperature. In order to give a reasonable description of the environment we need to include the thermodynamical properties like the equation of state of the environment and a model describing the energy transport.

2.3.1 Equation of State (EOS)

An equation of state (EOS) relates the state variable pressure, temperature, and density to each other. The EOS used in GAMBLER is taken from the web site of Frank Timmes [11] and is comprised of four components

$$P_{tot} = P_{rad} + P_{ion} + P_{ele} + P_{pos} \tag{2.24}$$

$$E_{tot} = E_{rad} + E_{ion} + E_{ele} + E_{pos} \tag{2.25}$$

where P_{tot} is the scalar pressure (in ergs/cm^3) and E_{tot} is the specific thermal energy (in ergs/g). The subscripts “rad”,”ion”, ”ele”, and “pos” represent contributions from radiation, nuclei, electrons, and positrons.

The radiation portion is calculated assuming blackbody radiation in local thermodynamic equilibrium:

$$P_{rad} = \frac{aT^4}{3}, \qquad E_{rad} = \frac{3P_{rad}}{\rho} \tag{2.26}$$

where a is the radiation density constant, which is related to the Stefan-Boltzmann constant (σ) by $a = 4\sigma/c$ and c is the speed of light in vacuum. For the ion part the ideal gas law is used:

$$n_{ion} = \frac{N_A \rho}{\overline{A}}, \quad P_{ion} = n_{ion} kT, \quad E_{ion} = \frac{3P_{ion}}{2\rho}, \tag{2.27}$$

where n_{ion} is the number of ions per unit volume, N_A is Avogadro's number, ρ is the mass density, $\overline{A}$ is the average number of nucleons per nucleus.

For the electrons and positrons a noninteracting Fermi gas is assumed with an arbitrary degree of degeneracy. The Thermodynamic potential is the Helmholtz free energy.

$$F = E - TS, \quad dF = -SdT + \frac{P}{\rho^2} d\rho. \tag{2.28}$$

where S is the specific entropy (in ergs/g/K). The pressure is then given by

$$P = \rho^2 \left. \frac{\partial F}{\partial \rho} \right|_{\rho} \tag{2.29}$$

A table of Helmholtz free energy and eight of its partial derivatives are in a file. The program has an interpolation scheme using a bi-quintic Hermite polynomial to determine actual values from the table. For a detailed description of the EOS and it's interpolation scheme see Reference 12.

2.3.2 Energy Transport

During nuclear burning, energy is being generated by the nuclear reactions and energy is also being carried away by radiation transport, conduction and convection. The basic equation for temperature change is

$$\frac{\partial T}{\partial t} = \frac{1}{C_p} \left(\epsilon_{nuc} - \frac{d\mathcal{F}}{dy} \right) \tag{2.30}$$

where C_p is the specific heat at constant pressure, ϵ_{nuc} is the energy generated from nuclear reactions (in ergs/s/g), and $\mathcal{F}$ represents the flux of energy leaving the zone (in ergs/s/cm^2). The column depth y (in g/cm^2) , is used here instead of the Cartesian displacement coordinate. This change of base comes from the simple relation $dy = \rho dz$ were z is the Cartesian coordinate.

The flux of energy can be carried away by three forms of energy transport, radiation, conduction, and convection. This program takes into account radiation and conduction while ignoring convection, as this is a one zone model. The flux can be written generally as

$$\mathcal{F} = K\nabla T = -K\rho\frac{dT}{dy} \tag{2.31}$$

where T is the temperature and K is the conductivity. Hydrostatic balance will yield $P = gy$ where $g \approx GM/R^2$. M and R are the neutron star mass and radius. Following Bildsten [13], we approximate dT/dy by T/y which provides $d\mathcal{F}/dy = -g^2/P^2\rho KT$ which along with Equation 2.30 is written as

$$\frac{\partial T}{\partial t} = \frac{1}{C_p}\left(\epsilon_{nuc} - \frac{g^2}{P^2}\rho KT\right) \tag{2.32}$$

The conductivity can be broken up with

$$K = K_{rad} + K_{cond} \tag{2.33}$$

where these represent the conductivity from radiation and conduction. The radiative component is written as

$$K_{rad} = \frac{16\sigma T^3}{3\rho}\frac{1}{\kappa_{th} + \kappa_{ff}} \tag{2.34}$$

where T is the temperature, σ is the Stefan-Boltzmann constant, ρ is the mass density, and κ_{th}, κ_{ff} are the opacities due to Thomson scattering and free–free scattering. The calculation of κ_{th} opacity is outlined in Reference 14 and κ_{ff} in Reference 15. The conductivity due to electron transport can be written as

$$K_{cond} = \frac{\pi^2 n_e k_b^2 T}{3m^*(\nu_{ee} + \nu_{ei} + \nu_{eq})} \tag{2.35}$$

where n_e is the electron number density, k_b is the Boltzmann constant, m^* is the relativistic effective mass of an electron at the Fermi surface, and $\nu_{ee,ei,eq}$ are the collision frequencies for electron–electron, electron–impurity, and electron–ion. Calculations of the collision frequencies are given in References 16, 17, and 18

Neutrino energy losses is not considered in GAMBLER currently. The interaction of neutrinos is small can can be neglected on the surface of the neutron star. The neutrino energy in beta decay would effectively enhance the cooling rate if implemented.

2.4 Numerical Technique

Equation 2.5 described in Section 2.2 represents a highly "stiff" set of ordinary differential equations (ODEs). A set of equations is considered "stiff" when the scales for independent variables are very different. As an example, consider the change in abundance from two different reactions. From Equation 2.5 one can write:

$$\frac{dY_i}{dt} = -Y_i Y_j \rho N_A \langle \sigma\nu \rangle_{ij,kl} + Y_j \frac{ln(2)}{t_{1/2_{j\to i}}} \tag{2.36}$$

Here the coefficients, given by $Y_i \rho N_A \langle \sigma\nu \rangle_{ij,kl}$ and $ln(2)/t_{1/2_{j\to i}}$, could be different by 100 orders of magnitude. One has to consider this when choosing a numerical technique.

For GAMBLER the problem is considered an *initial value problem*, meaning the initial values for all abundances are known and a solution for the abundance at a future time is needed. One must approximate dY by ΔY, a finite step, and calculate the abundance at a future time by making appropriately small steps ΔY. This procedure is know as *Euler's method.* For a simple equation such as:

$$y' = -cy \tag{2.37}$$

where $c > 0$ and constant, there are two Euler methods for writing y_{n+1}, the value of

y after one time step. The forward Euler method would give:

$$y_{n+1} = y_n + hy'_n = (1 - ch)y_n \tag{2.38}$$

where h is the step size. If $h > 2/c$ this method is unstable and would lead to an exponential increase in $|y_{n+1}|$, to overcome such instabilities requires the time steps to be extremely small for a stiff set of equations where the coefficient c can be very large. One solution to this problem is to use implicit, or backward Euler method. In this approach:

$$y_{n+1} = y_n + hy'_{n+1} = (1 + ch)^{-1}y_n \tag{2.39}$$

which will remain stable even with large time step h.

The technique used in GAMBLER for solving the set of ODEs comes from Bader and Deuflhard [19], and is described in detail in Numerical Recipes in C++ [20]. This method is a variable-order calculation based on the *semi-implicit Euler method.* The starting point is an implicit form of the midpoint rule:

$$\mathbf{y}_{n+1} - \mathbf{y}_{n-1} \approx 2h\mathbf{f}\left(\frac{\mathbf{y}_{n+1} + \mathbf{y}_{n-1}}{2}\right) \tag{2.40}$$

where $\mathbf{f}(\mathbf{y})$ is the expression for the derivative given by the differential equation. Since there are many yields involved, $\mathbf{f}(\mathbf{y})$ is a function of the many yields that are coupled to $\mathbf{f}$ by the differential equation. This is linearized using a Taylor expansion to first order giving:

$$\left[\widetilde{\mathbf{1}} - h\frac{\partial \mathbf{f}}{\partial \mathbf{y}}\right] \cdot \mathbf{y}_{n+1} = \left[\widetilde{\mathbf{1}} - h\frac{\partial \mathbf{f}}{\partial \mathbf{y}}\right] \cdot \mathbf{y}_{n-1} + 2h\left[\mathbf{f}(\mathbf{y}_n) - \frac{\partial \mathbf{f}}{\partial \mathbf{y}}\right] \cdot \mathbf{y}_n. \tag{2.41}$$

which can then be written as

$$\mathbf{y}_{n+1} = \mathbf{y}_{n-1} + 2h\left[\widetilde{\mathbf{1}} - h\frac{\partial \mathbf{f}}{\partial \mathbf{y}}\right]^{-1}\left[\mathbf{f}(\mathbf{y}_n) - \frac{\partial \mathbf{f}}{\partial \mathbf{y}}\right] \cdot \mathbf{y}_n \tag{2.42}$$

The first time step is done using the semi-implicit Euler step and the last time step in this method is modified for "smoothing". The last $\mathbf{y}_n$ is replaced by

$$\overline{\mathbf{y}}_n \equiv \frac{1}{2}(\mathbf{y}_{n+1} + \mathbf{y}_{n-1}) \tag{2.43}$$

This is implemented in GAMBLER by using $\Delta_k \equiv \mathbf{y}_{k+1} - \mathbf{y}_k$, with $h = H/m$. The first semi-implicit Euler step is then given by

$$\Delta_0 = \left[\widetilde{\mathbf{1}} - h\frac{\partial \mathbf{f}}{\partial \mathbf{y}}\right]^{-1} \cdot h\mathbf{f}(\mathbf{y}_0) \tag{2.44}$$

$$\mathbf{y}_1 = \mathbf{y}_0 + \Delta_0 \tag{2.45}$$

Equation 2.42 is then rewritten with k = 1,...,m-1, as

$$\Delta_k = \Delta_{k-1} + 2\left[\widetilde{\mathbf{1}} - h\frac{\partial \mathbf{f}}{\partial \mathbf{y}}\right]^{-1} \cdot [h\mathbf{f}(\mathbf{y}_k) - \Delta_{k-1}] \tag{2.46}$$

$$\mathbf{y}_{k+1} = \mathbf{y}_k + \Delta_k \tag{2.47}$$

Finally the last "smoothing" step is computed

$$\Delta_m = \left[\widetilde{\mathbf{1}} - h\frac{\partial \mathbf{f}}{\partial \mathbf{y}}\right]^{-1} \cdot [h\mathbf{f}(\mathbf{y}_m) - \Delta_{m-1}] \tag{2.48}$$

$$\overline{\mathbf{y}}_m = \mathbf{y}_m + \Delta_m \tag{2.49}$$

In order to achieve the necessary accuracy, the differential equation given by Equation 2.36 is integrated numerically using the method of Bader and Deuflhard with a variable step size. In particular this procedure is done a variable number of times for each time step H by varying n, the number of sub steps, and then extrapolation in a Richardson extrapolation to the correct result with zero length step sizes. Figure 2.1 shows the idea of the Richardson Extrapolation. Here the time step from x to $x + H$ is broken down into n sub steps. The calculation is performed for

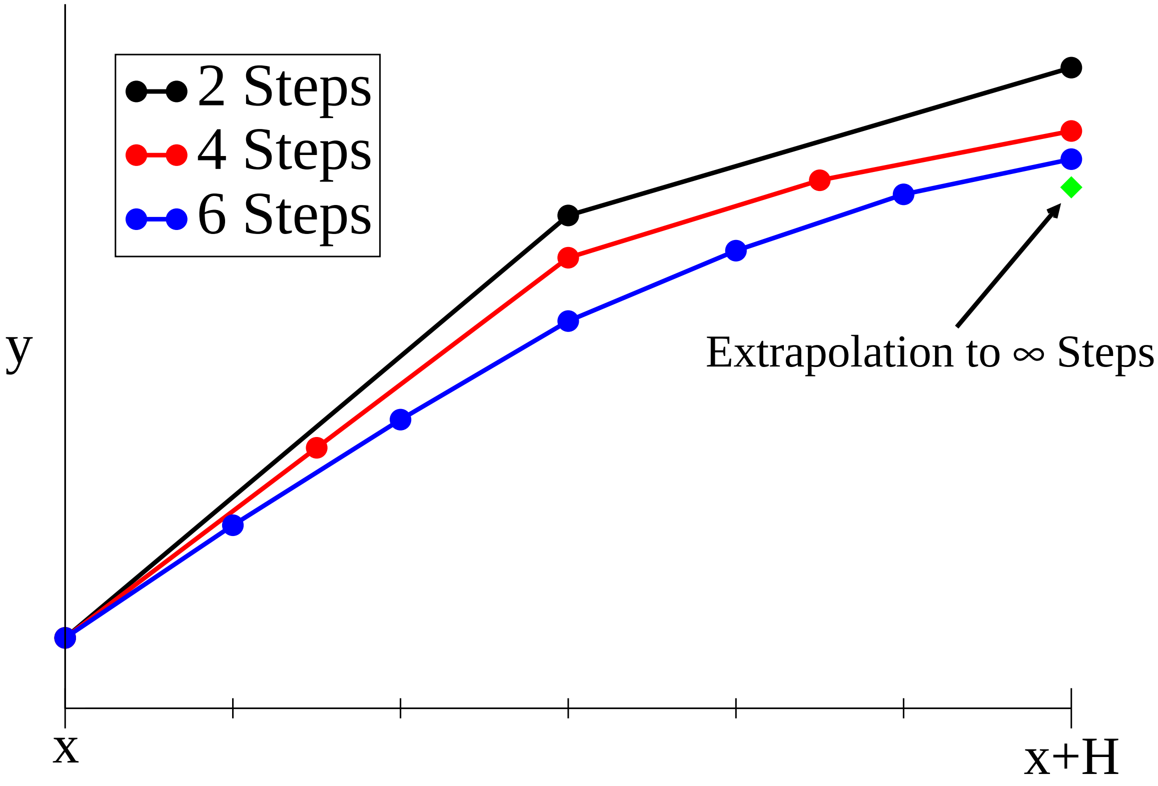

Figure 2.1: Richardson Extrapolation example

$n = 2, 4, 6, 8, 10, 12, 14, \ldots, [n_j = 2(j+1)], \ldots$ until the accuracy of an polynomial extrapolation to $n = \infty$ has an uncertainty below a user specified value. Once this occurs the time step H is accepted.

Considering equations such as 2.44 one can define the matrices:

$$\widetilde{\mathbf{A}} = \left(\widetilde{\mathbf{1}} - h\widetilde{\mathbf{J}}\right) \tag{2.50}$$

where $\widetilde{\mathbf{J}}$ is the Jacobian matrix, which is defined as:

$$\widetilde{\mathbf{J}} = \frac{\partial \mathbf{f}}{\partial \mathbf{y}} \tag{2.51}$$

Then one has to solve a matrix equation of the form:

$$\widetilde{\mathbf{A}} \cdot \Delta = h\mathbf{f}(\mathbf{y}_n) \tag{2.52}$$

As indicated above, the quantities $\mathbf{y}$ and $\mathbf{f}$ in the preceding equations are vector quantities. The quantity $\partial\mathbf{f}/\partial\mathbf{y}$ is therefore a matrix. This matrix represents the flow, in nuclei per second, from the initial nuclear abundances towards the final abundances. In principle all elements of the Jacobian matrix should be non zero as all reactions are possible, however most reactions, such as ^{32}S+^{56}Ni are not considered for reasons discussed in Section 2.2.1. Each non-zero element in this matrix represents some reaction flow that must be calculated.

The non-zero elements in the Jacobian matrix are shown in Figure 2.2. One can see that the important rates lie close to the diagonal corresponding to all γ capture/decay and beta decays. This matrix is non-symmetric, as forward and reverse rates are often very different. The Jacobian changes with time based on the reaction rates used. For these calculations the Jacobian is 98.4% sparse, i.e 98.4% of the matrix elements can be neglected. This figure shows the highly sparse 686 by 686 matrix. To increase numerical stability the final 3 elements are n,p,α. With this exception, the elements of the matrix begin with low mass in the top left corner and increse down and left.

GAMBLER uses a math package called UMFPACK [21] to perform the matrix solving of Equations 2.44,2.46, and 2.48. This is a special package of math routines specifically written to solve equations of the form given in Equation 2.52. This math package uses the Unisymmetric Multi-Frontal method and direct sparse LU factorization [22].

2.4.1 Time Step Calculation

Once a step has been performed GAMBLER computes a guess for the optimum time step to try next. This is done by considering the time required to converge after an appropriate number of n sub step attempts. If the initial step size it too large it will require too many sub steps, which increases the computation time. If the program estimates the number of sub steps will be excessive it will re-scale H to a smaller value and start over. If the value for H is chosen to be too small each step H will

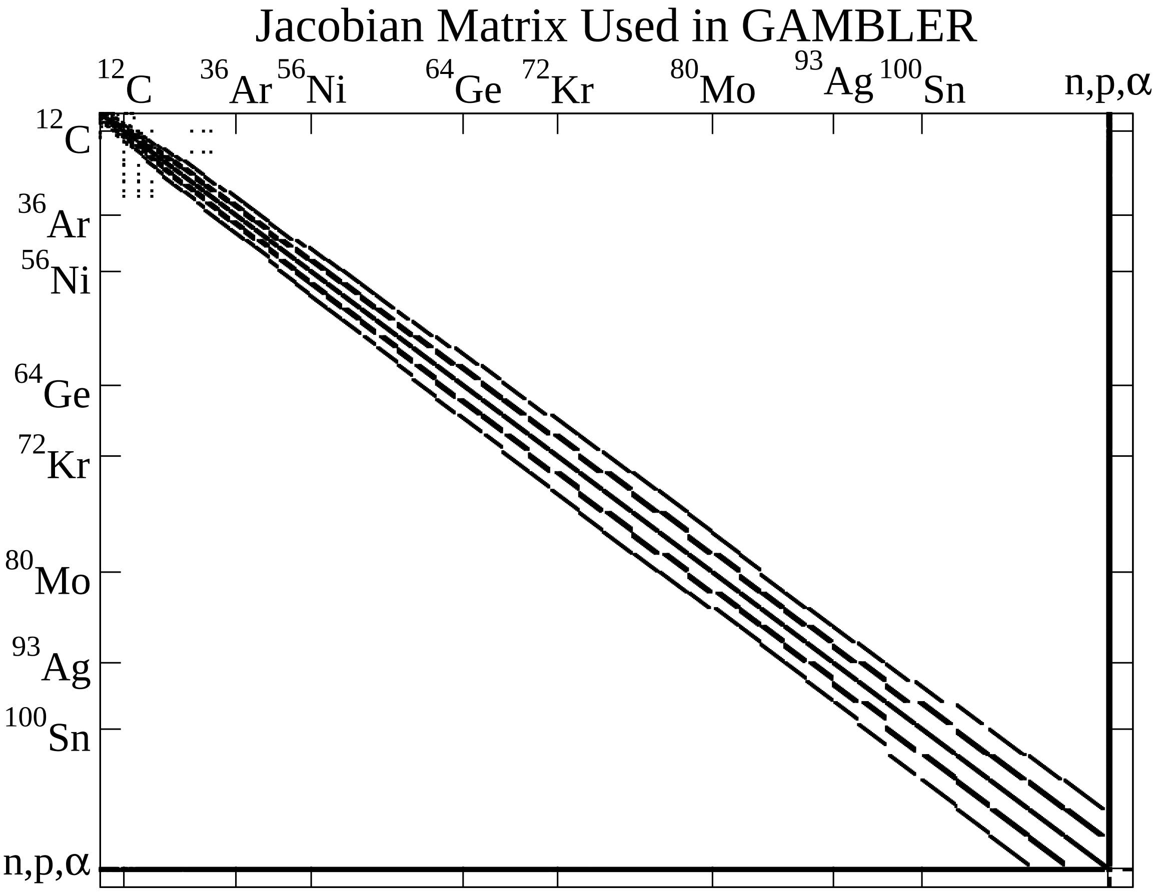

Figure 2.2: The Jacobian matrix $\partial \mathbf{f}/\partial \mathbf{y}$ used in GAMBLER

converge quickly but the total calculation requires excessive steps H to complete the calculation. This is why the next time step H is recomputed after each accepted time step. When reaction rates are low, very large time steps can be performed without any accuracy problems. When the temperature increases and reactions rates become large, the time step must be smaller.

Once the abundance step has been completed and the calculation of the next step size is determined, GAMBLER calculates explicitly the temperature change based on the Equation 2.32. The thermal time-scale, which is defined to be the time required to reach zero temperature or to double the temperature, is computed by:

$$t_{therm} = \frac{T}{\Delta T} \Delta t_{did} \tag{2.53}$$

where t_{did} is the last time step size. If the next time step H_{try} is greater then 1% of the thermal time scale, the program replaces H_{try} by $0.01 t_{therm}$.

Figure 2.3 demonstrates the variable time stepping. In the top figure the thermal profile of a X-ray burst calculation is shown. In the lower figure the time step (H) taken is shown as a function of burst time. One can see the step size becomes small at the ignition and then again when there are significant changes in the thermal profile. During ignition, the step size can be as small as a millisecond. Towards the end of the burst, when it is cooling, the step size is of the order of 10's of seconds.

2.5 Inputs for GAMBLER

In order to model the rp-process a network of 686 nuclei from neutrons and protons up to Xenon was used.

Figure 2.4 shows a chart of the nuclei for all nuclei included in the calculations. One can see that for each element isotopes from stability to the proton drip line are included. There are 7635 nuclear reactions that link these nuclei together. For all

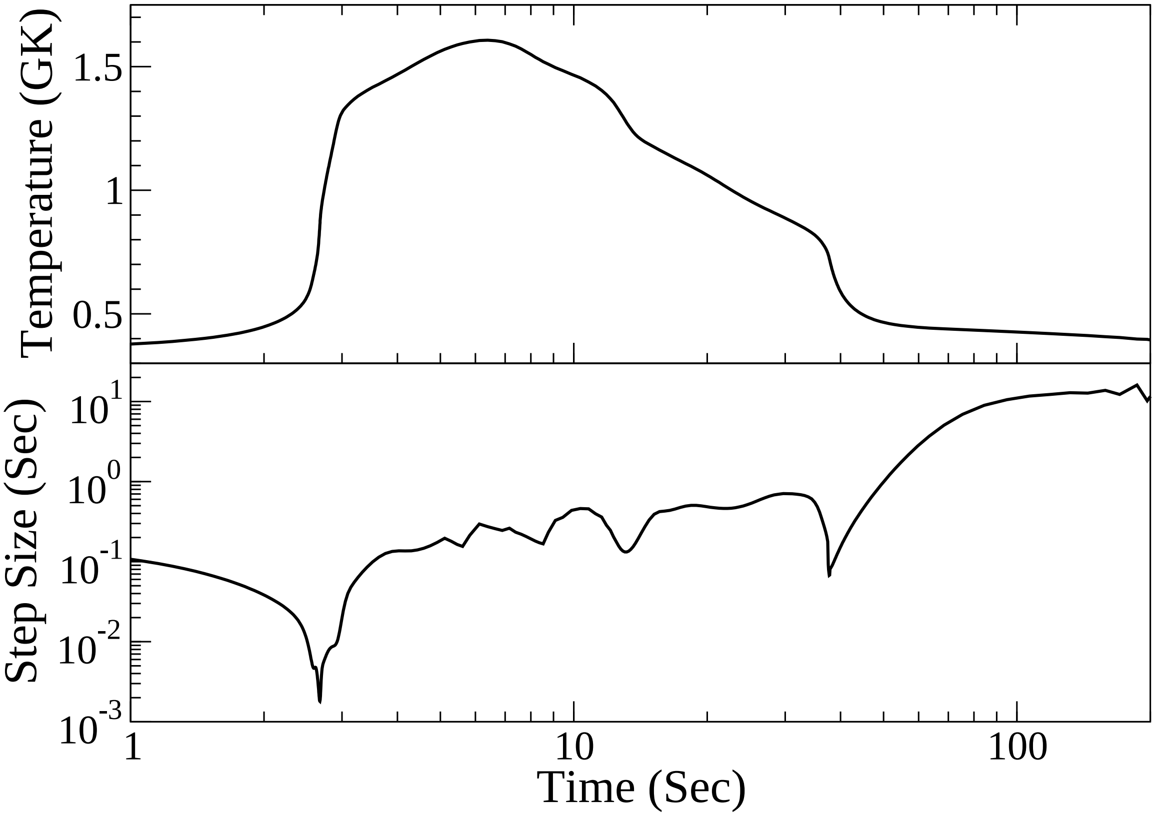

Figure 2.3: Demonstration of the variable time stepping used in GAMBLER

cases studied the local gravity was taken to be 1.9×10^{14} dyne/g. The column depth is given for each condition and is held fixed during the burst. The column depth is on the order of 2×10^{14} g/cm^3. The pressure is calculated from this and held fixed during the burst. The pressure is on the order of 5×10^{22} ergs/cm^3. The density is varying during the burst but is typically on the order 10^5–10^6 g/cm^3.

2.6 Burst Conditions

A one zone model can be used to study the influence of key nuclear physics inputs upon the burst characteristics; however it can not accurately predict the conditions for which bursts can occur on the surface of neutron stars. For this a 1-D model is used. The key parameter in 1-D models is the accretion rate. The accretion rate will determine how much material builds up on the surface before ignition occurs,

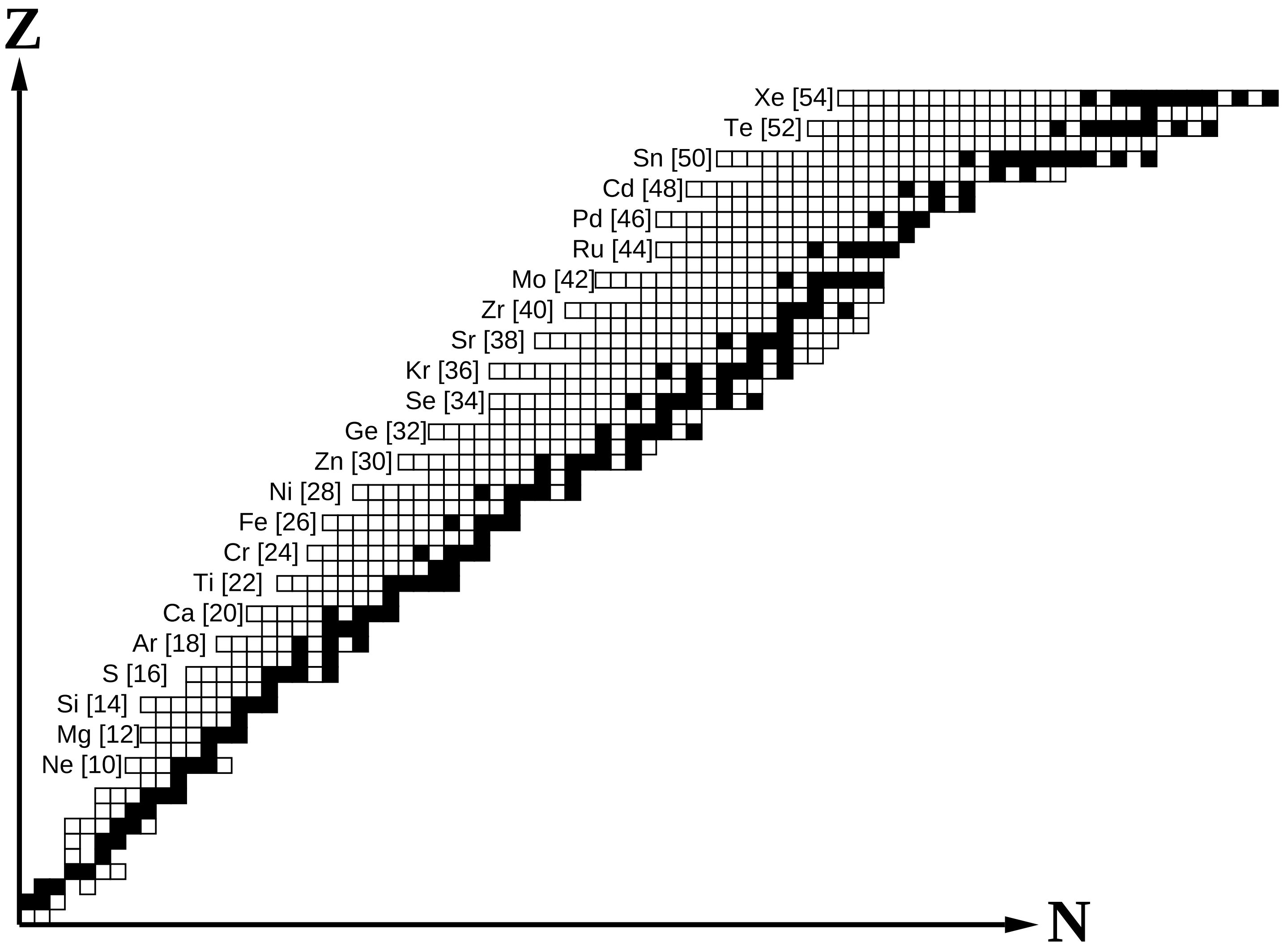

Figure 2.4: Nuclei used in GAMBLER calculations

and how long this takes. Solving a 1-D model provides values for the temperature, column depth, and initial abundances at the time of ignition. As mass builds up on the surface, hydrogen burning will occur and the amount of hydrogen burned before ignition will determine how many of the heavier elements are formed. This affects the thermal profile of the burst.

In this dissertation we used the ignition conditions given by Cummings and Bildsten [23]. The ignition of the rp-process basically occurs when heating from the triple alpha reaction exceeds cooling from radiation and conduction. The triple alpha reaction rate used in GAMBLER differs from that used in Cumming and Bildsten, therefore to simulate a burst with identical ignition conditions, such as the metallicity, density, and column depth, GAMBLER requires a higher pre-burst temperature. This should not affect the results of the burst as its temperature will rise very quickly to something greater than a billion degrees. This increase occurs before any substantial change to any of the abundances can occur. To test this, one set of ignition conditions was used for several different pre-burst temperatures. All of them were large enough to initiate ignition. Figure 2.5 shows the temperature profile for each of these burns.

From this figure one can see that the maximum temperature and general shape are not effected by the initial temperature, the only effect is a shift of a few seconds in the ignition time. To verify this the time axis is shifted to align the thermal profiles of all three bursts. This is shown in Figure 2.6. As one can see here, the curves are indistinguishable. Even zoomed in to the first 10 seconds the overlap is perfect.

The conditions for ignition depend on the local mass accretion rate. The ratio of this accretion rate over the Eddingtion local mass accretion rate $\dot{m}/\dot{m}_{edd}$ is used to define different ignition conditions. The Eddingtion local mass accretion rate $\dot{m}_{edd}$=8.8×10^4 g cm^{-2}s^{-1}, is equivalent to a global rate $\dot{M}_{edd}$=1.7×10^{-8} $M_{\odot}$yr^{-1} when integrated over the stellar surface. GAMBLER was run with four different ignition conditions corresponding to four different accretion rates. Table 2.1 gives the initial

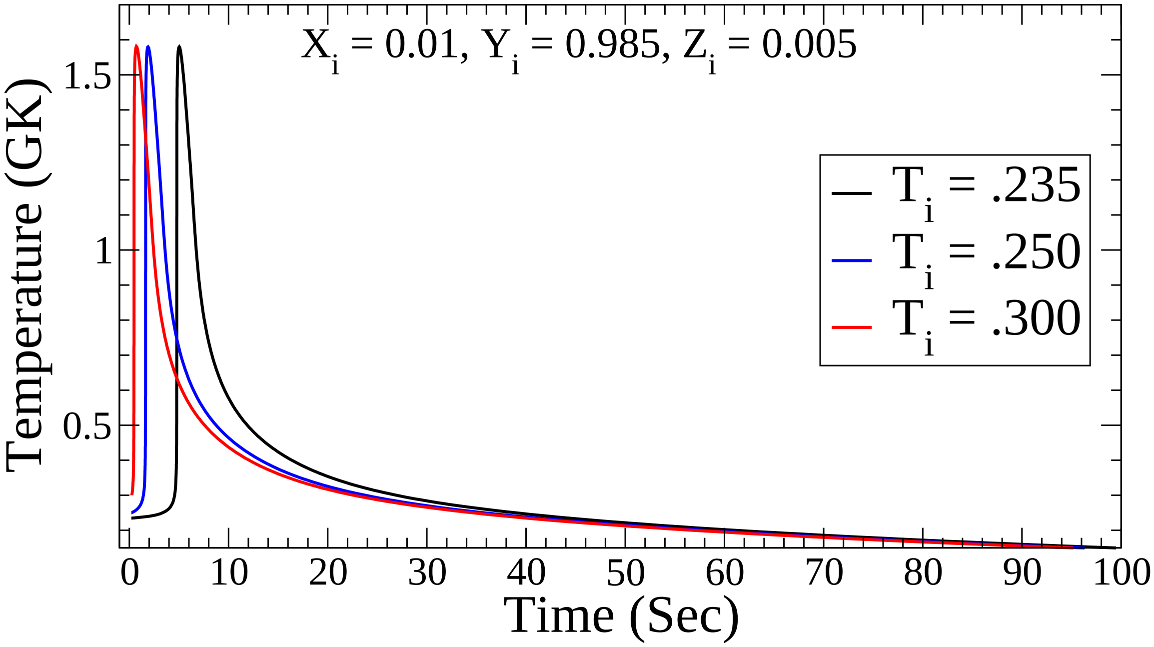

Figure 2.5: Temperature during an X-ray burst for three different initial temperatures

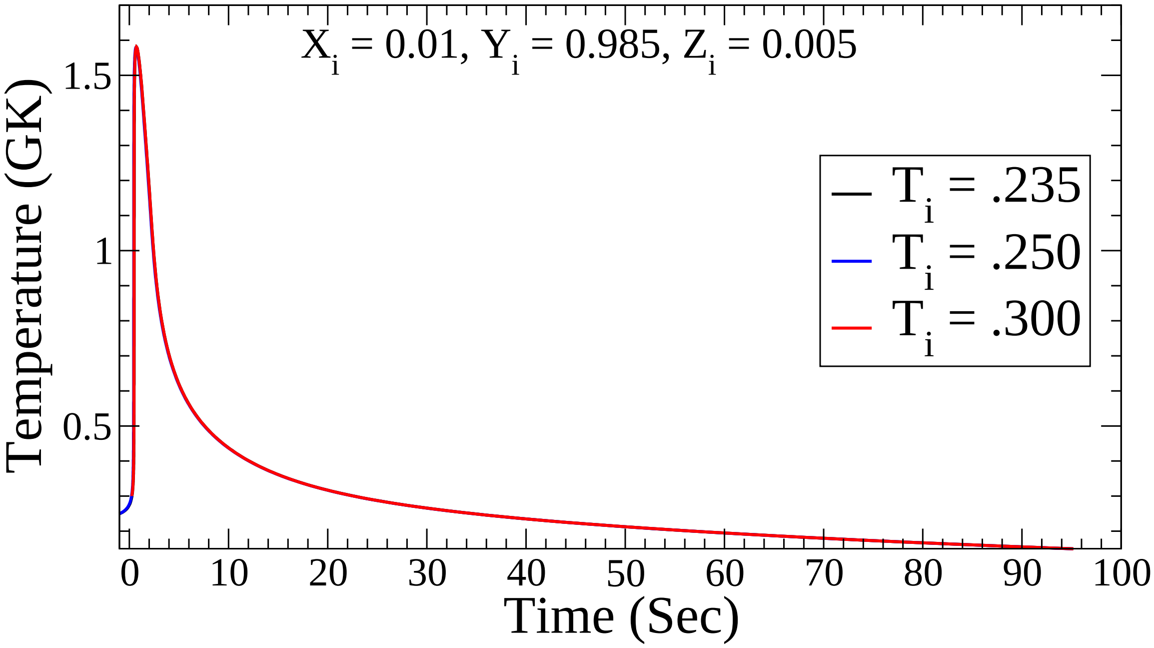

Figure 2.6: Temperature during an X-ray burst for three different initial temperatures with a small offset applied to align ignition times

Table 2.1: The ignition conditions used by GAMBLER

$\dot{m}/\dot{m}_{edd}$	Z_{CNO}	X	Y	T (10^8 K)	y (10^8 g cm^{-2})	ρ (10^6 g cm^{-3})
0.01	0.005	0.01	0.985	1.73	2.05	1.16
0.03	0.005	0.31	0.685	1.86	2.35	0.94
0.10	0.005	0.57	0.425	2.05	2.70	0.84
0.30	0.005	0.67	0.325	2.24	2.62	0.76

conditions provided in Ref. 23. Given in this table is the accretion rate as defined by $\dot{m}/\dot{m}_{edd}$, the mass fraction of CNO elements (Z_{CNO}), the mass fraction of hydrogen (X), the mass fraction of helium (Y), the temperature, the column depth, and the density at the time of ignition.

2.7 Results from GAMBLER

The goal of this project was to study the nuclear physics inputs which are important in the region of ^{64}Ge. We therefore look more closely at the results from these calculations. For all calculations performed, a minimum accuracy of 1×10^{-5} was required. This means that the uncertainly in the abundance of every nucleus, after extrapolation to infinite sub step number, was less than 1×10^{-5} of the current abundance. This is true for all nuclei with abundances above 1×10^{-6}. For nuclei with abundances below 1×10^{-6}, this requires the uncertainty in the abundance to be less than 1×10^{-11}. Higher accuracies were not required for such low abundances because one is not concerned about the uncertainties in abundances that are 10–30 orders of magnitude below the most abundant nuclei. With this accuracy stipulated, bursts were calculated for the ignition conditions given in Table 2.1. For all of these calculations the total number of steps (H) taken was around 350–600. These calculations were done on a dual processor Intel machine running Linux. The computation time was between 15–20 minutes for each X-ray burst calculation.

Figure 2.7 shows the temperature profile for bursts assuming the mass accretion

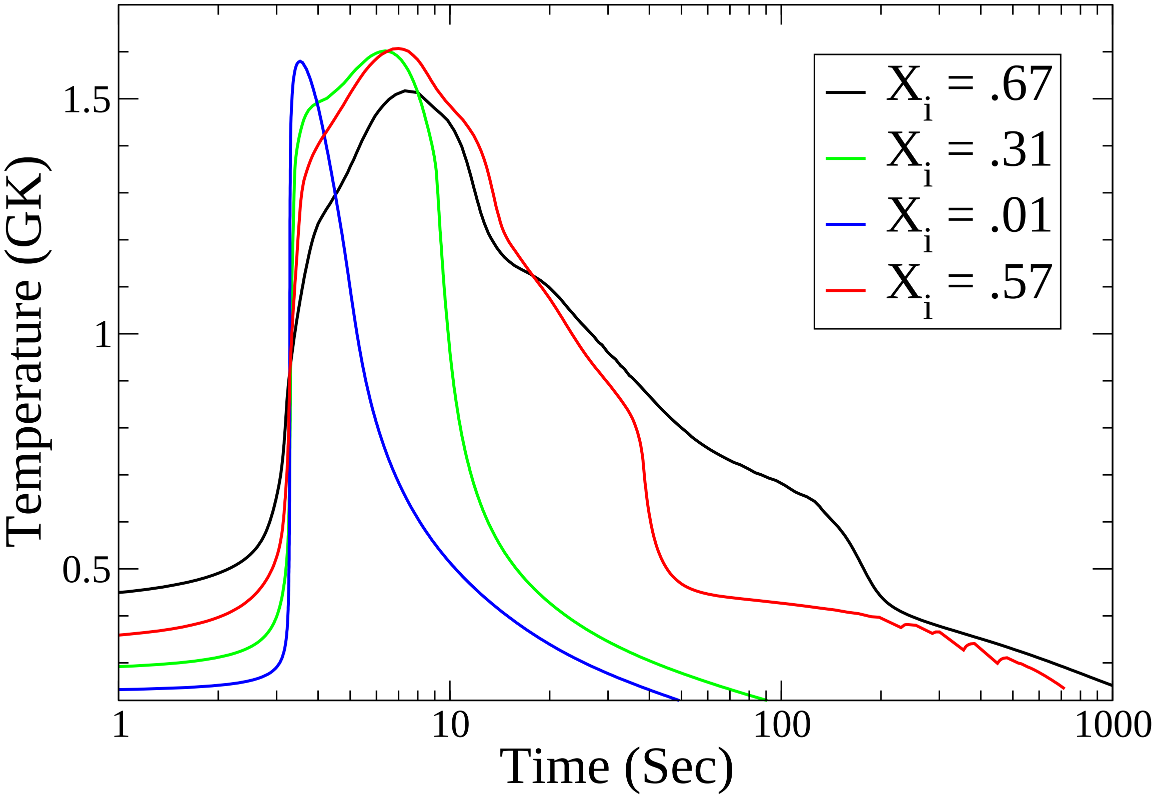

Figure 2.7: Temperature profile of X-Ray burst for different mass accretion

and ignition conditions given in Table 2.1. The ignition time has been lined up for all bursts as discussed in the preceding section. One can see that the duration of the burst and its general shape are determined by the initial composition, which is dictated by the mass accretion rate. The rise time is slower and the burst extends to longer times for large hydrogen abundances characteristic of high accretion rates. A description of each of these bursts follows.

As stated earlier, the mass accretion will determine the composition and ignition conditions before the burst, so we shall look first at the lowest mass accretion rate. For an accretion rate $\dot{m}/\dot{m}_{edd} = 0.01$, CNO burning converts almost all the hydrogen is converted into helium before ignition, leaving only 1% hydrogen at the time of ignition.

Figure 2.8 shows this burst. The top graph is the temperature as a function of time. Below this is a plot of the mass fraction of the most abundant nuclei during the

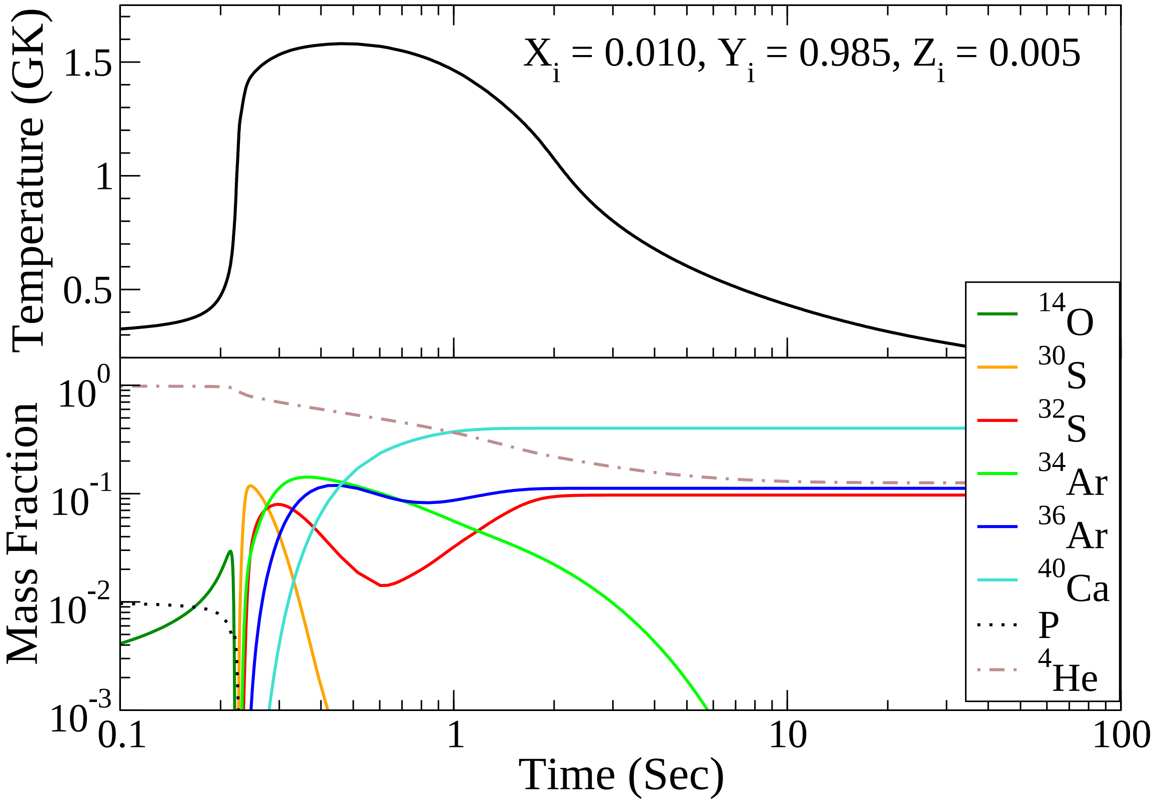

Figure 2.8: Burst description for an accretion rate $\dot{m}/\dot{m}_{edd} = 0.01$

burst. From this we can see the hydrogen fuel is used up almost immediately. The burst proceeds from the hot CNO cycle to more massive nuclei via the αp-process described in Section 1.3. Large abundances of $^{30\text{-}32}$S and $^{34\text{-}36}$Ar occur within the first second, followed by the dominant production of ^{40}Ca. For this burst the peak temperature is about 1.6 GK. This temperature is achieved in less than 1 second after ignition. The star rapidly cools for about 10 seconds, and then more slowly for an additional minute. At this low mass accretion rate we see that the rp-process does not really play an important role as the fuel runs out before the rp-process nuclei are made.

Figure 2.9 shows a burst with a slightly higher accretion rate of $\dot{m}/\dot{m}_{edd} = 0.03$. At this accretion rate the initial composition contains 31 % hydrogen. From the figure one can see that the initial distrobution is similar to that for the lower accreation rate of 0.01. However, with the higher accretion rate, there is still hydrogen fuel remaining

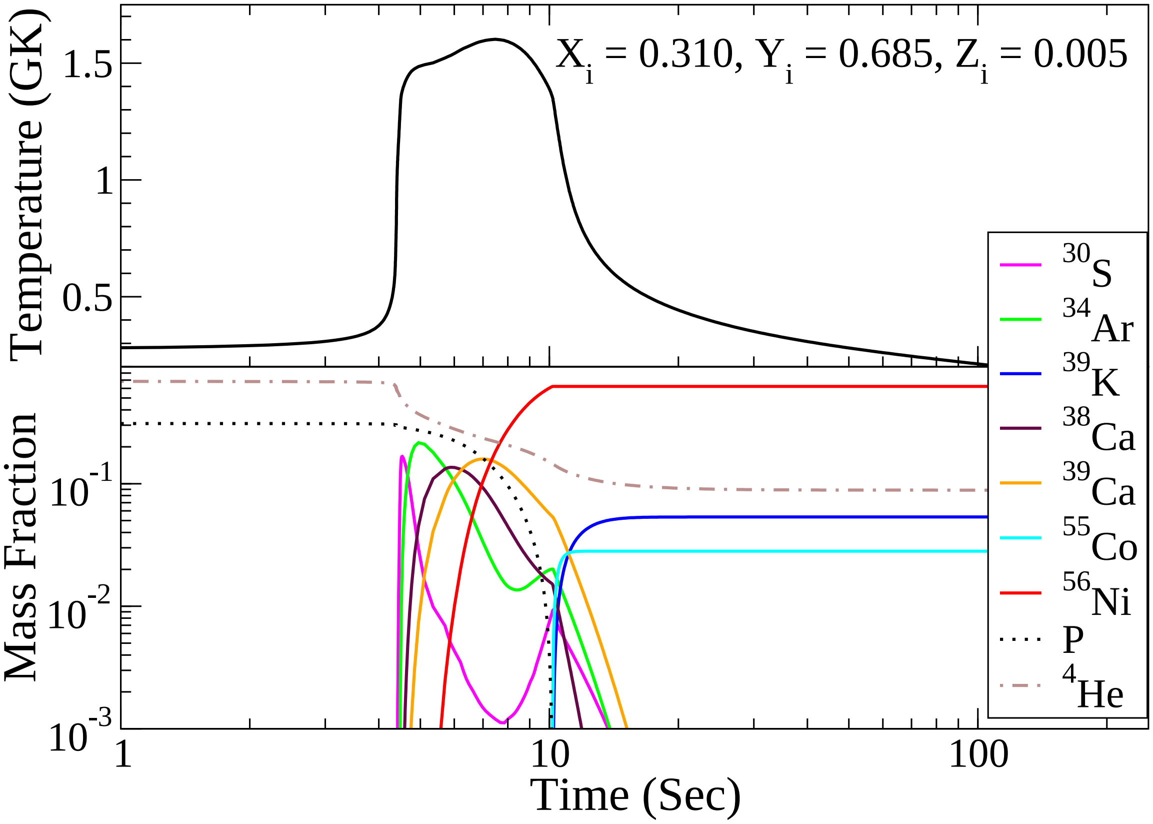

Figure 2.9: Burst description for $\dot{m}/\dot{m}_{edd} = 0.03$

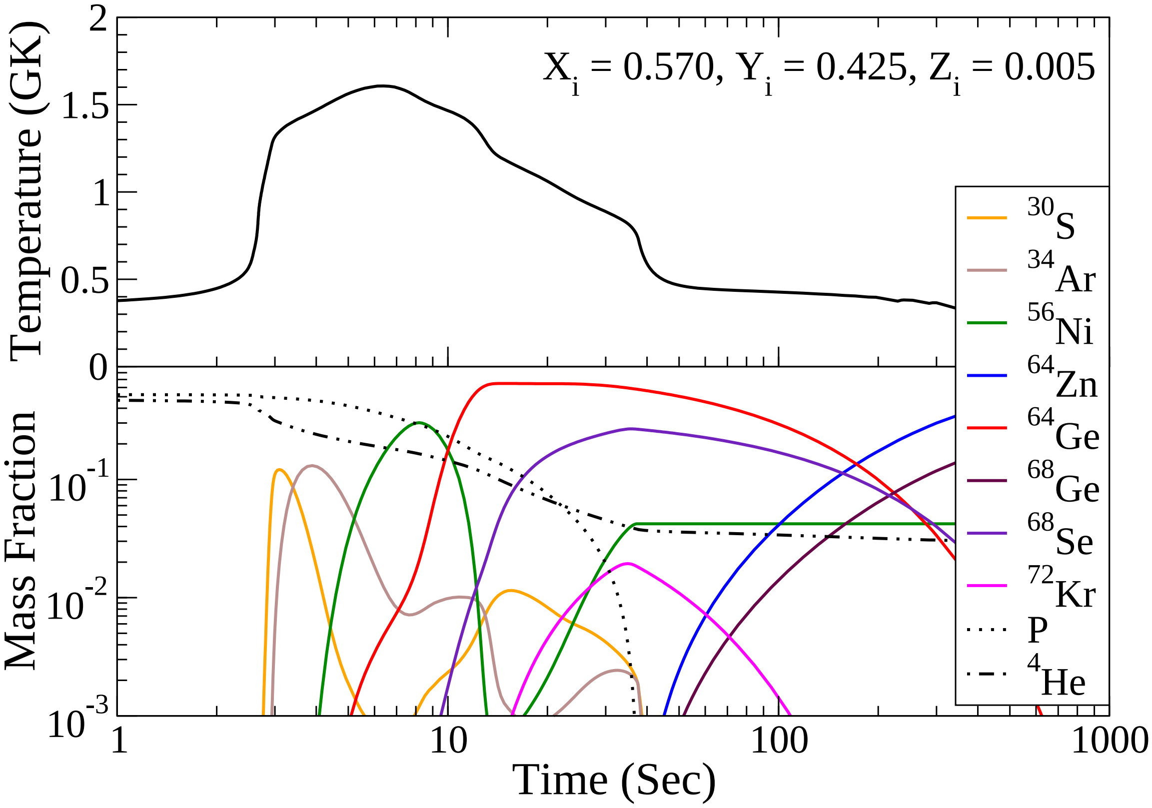

Figure 2.10: Burst description for $\dot{m}/\dot{m}_{edd} = 0.10$

after the αp-process completes, and one observes an rp-process that ends at ^{56}Ni. The burst peaks 5 seconds after ignition with a peak temperature of 1.6 GK. The rp-process uses all the hydrogen fuel in about 6-7 seconds, resulting in most of the mass converted to ^{56}Ni. Very little of the ^{56}Ni is burned in the rp-process to make heavier nuclei.

Figure 2.10 shows a burst with an even higher accretion rate of $\dot{m}/\dot{m}_{edd} = 0.10$. At this accretion rate the initial composition of hydrogen is 57%. Like the calculations with the lower accretion rates, the early stages are dominated by the αp-process. Then the rp-process occurs that processes material through ^{56}Ni. However, there is still hydrogen remaining at this accretion rate, which causes the ^{56}Ni to be converted quickly into ^{64}Ge after a few seconds of additional burning. The hydrogen fuel runs out after a burn of 20-25 seconds. The burst cools in about 30 seconds. At the time the hydrogen is consumed most of the mass is converted to ^{64}Ge. The half life of ^{64}Ge

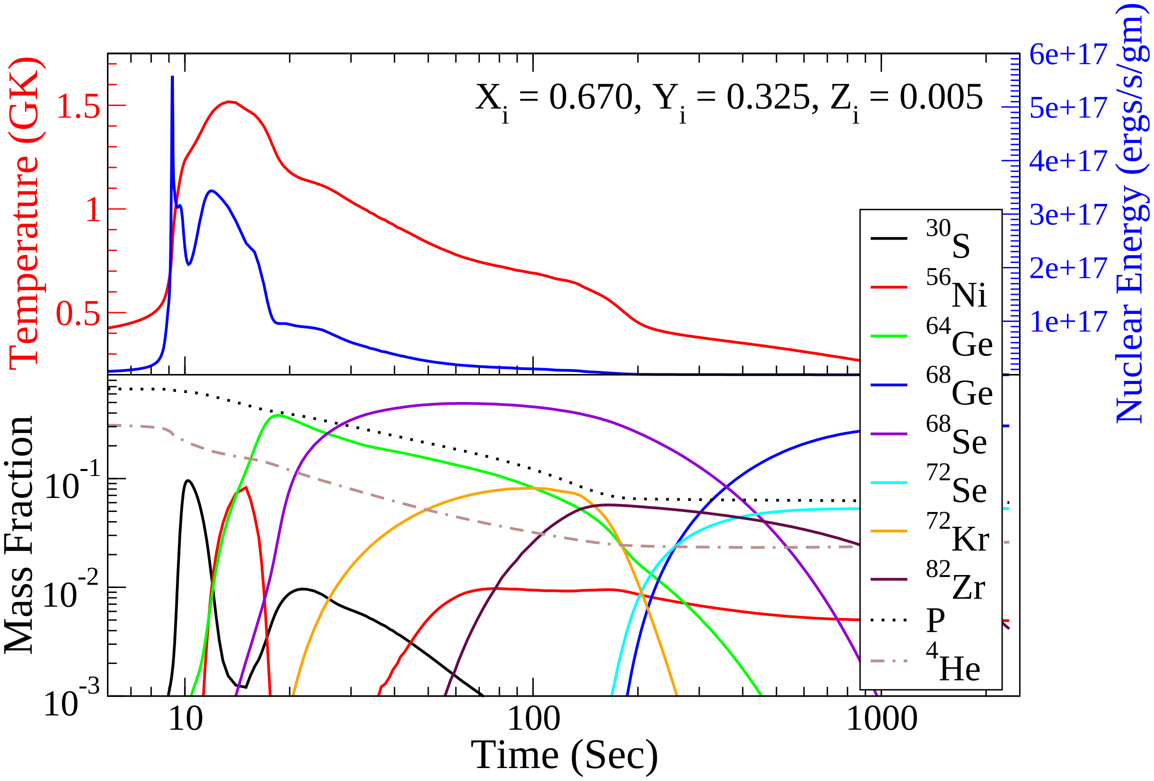

Figure 2.11: Burst description for $\dot{m}/\dot{m}_{edd} = 0.30$

is about 64 seconds. After some time beta decay converts this ^{64}Ge into ^{64}Zn.

The largest mass accretion rate we simulated was $\dot{m}/\dot{m}_{edd} = 0.30$, which is still only 30 % of the Eddington rate. Here one observes some interesting things. The burst begins like all the others with an αp-process followed by the rp-process rapidly up to ^{64}Ge. At this point, however, the hydrogen fuel is not used up. The burst continues for several hundred seconds and after about 60 seconds, corresponding to one half-life of ^{64}Ge, the abundance has shifted to ^{68}Se as shown at the bottom of Figure 2.11. After about 1000 seconds the distribution peaks at ^{68}Ge and there is some significant yield of ^{72}Se from the decay of ^{72}Kr. Some production of nuclei with masses up to ^{82}Zr occurs, but this yield is very small. There is still a fraction of hydrogen remaining after the burst.

Why does the hydrogen burning not continue? This can be understood by looking at the blue curve added to the top panel of this figure which shows the nuclear energy generation as a function of time. There are large bursts of energy during the αp-

Table 2.2: Half-lives for waiting point nuclei

Nuclei	Half-Life (Sec)
^{64}Ge	63.7
^{68}Se	35.5
^{72}Kr	17.2

process and during the rp-process as it burns nuclei up to ^{64}Ge. Then the nuclear energy generation goes way down, because much of the mass is sitting at the ^{64}Ge waiting point. Then, after beta decay of ^{64}Ge, nuclei are burned up to the ^{68}Se waiting point. If some nuclei burn past ^{68}Se the burning continues up to the ^{72}Kr waiting point. This demonstrates that there is enough hydrogen fuel for the burst to continue well beyond the ^{64}Ge, ^{68}Se, and ^{72}Kr waiting points, if the time spent at these waiting points were shorter. Given the time spent at these waiting points, it is necessary to investigate the various nuclear physics aspects which play a role in this mass region, and how accurate data can change our predictions for the rp-process.

2.8 Key Nuclear Physics

From the last section, one can observe that bursts can occur at sufficiently high accretion rates, which terminate with unburned hydrogen. This is due to the waiting point nuclei ^{64}Ge, ^{68}Se, and ^{72}Kr. The half-lives of these nuclei are given in Table 2.2.

From this table one can see that ^{64}Ge has the longest half-life. As it is also the lowest mass of the 3 waiting points it is the most important one to study.

There are two ways to go beyond ^{64}Ge, the first is to beta decay producing ^{64}Ga. The second way is by proton capture via the ^{64}Ge$(p,\gamma)^{65}$As reaction. The resulting ^{65}As can beta decay to ^{65}Ge or capture a proton via the ^{65}As$(p,\gamma)^{66}$Se reaction, and then beta decay to ^{66}As.

We calculate the ^{64}Ge$(p,\gamma)^{65}$As reaction rate assuming it proceeds through 3 narrow resonances in ^{65}As that have been observed in the mirror nucleus, ^{65}Ge [24]. We calculate the ^{65}As$(p,\gamma)^{66}$Se reaction rate assuming that it proceeds through 3

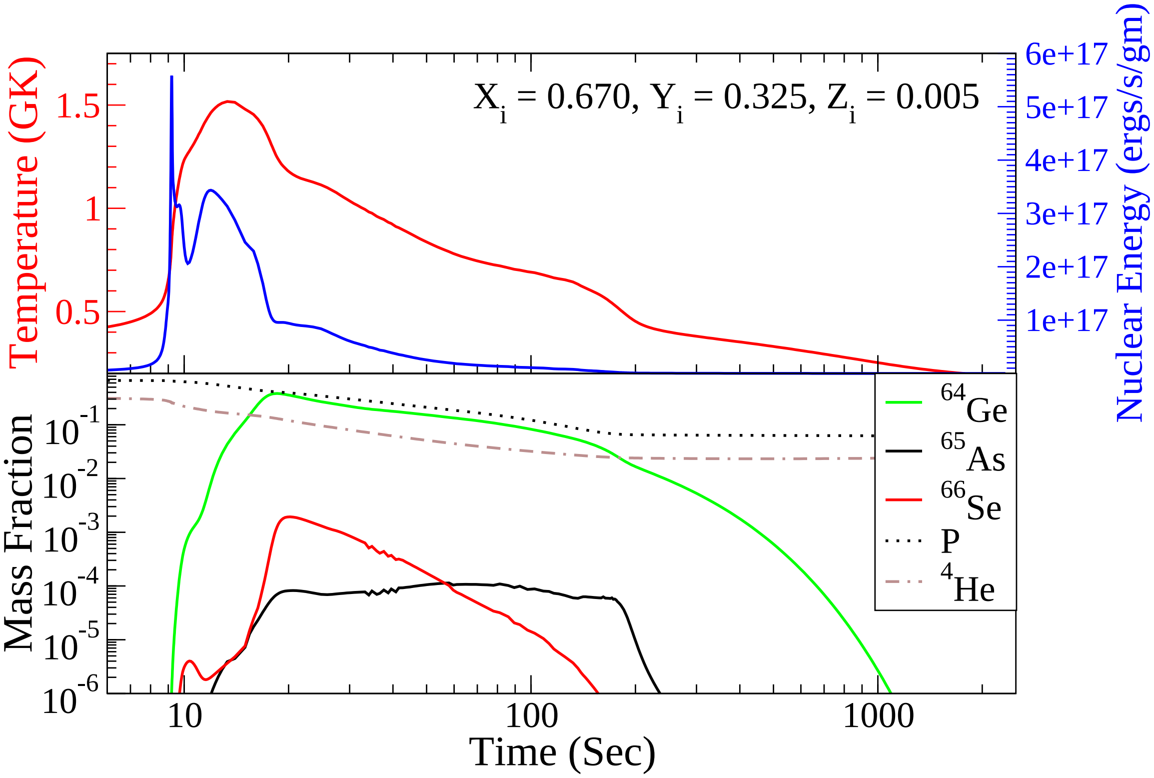

Figure 2.12: Abundances of nuclei in the ^{64}Ge region

narrow resonances that have been observed in the mirror nucleus, ^{66}Ge. The photodisintegration reaction rate, into ^{65}As or ^{64}Ge is calculated using detailed balance. If both the forward and backwards rates are sufficiently high, then nuclear statistical equilibrium will occur between ^{65}As and ^{64}Ge, or ^{66}Se and ^{65}As. Under these conditions there will be an equilibrium abundance that depends strongly on the Q-value of the (p, γ) reaction rate.

If equilibrium is not achieved the Q-value still strongly governs the time spent at the waiting point. The key property for understanding the flow through ^{64}Ge therefore is the Q-value of the ^{64}Ge$(p, \gamma)^{65}$As reaction. Of lesser importance is the structure of ^{66}Se, or its mirror ^{66}Ge. The Q-value is just the difference in mass; thus measurements of the relevant masses are critical. Recently the mass of ^{64}Ge was measured to be $\Delta M = -54343 \pm 30$ keV [25]. The mass of ^{65}As has never been measured. The mass of ^{65}As is given as $\Delta M = -46981 \pm 302$ KeV in the atomic mass evaluation table of 2003 [26]. Combining these results, the Q-value should be -73 keV ± 303 keV.

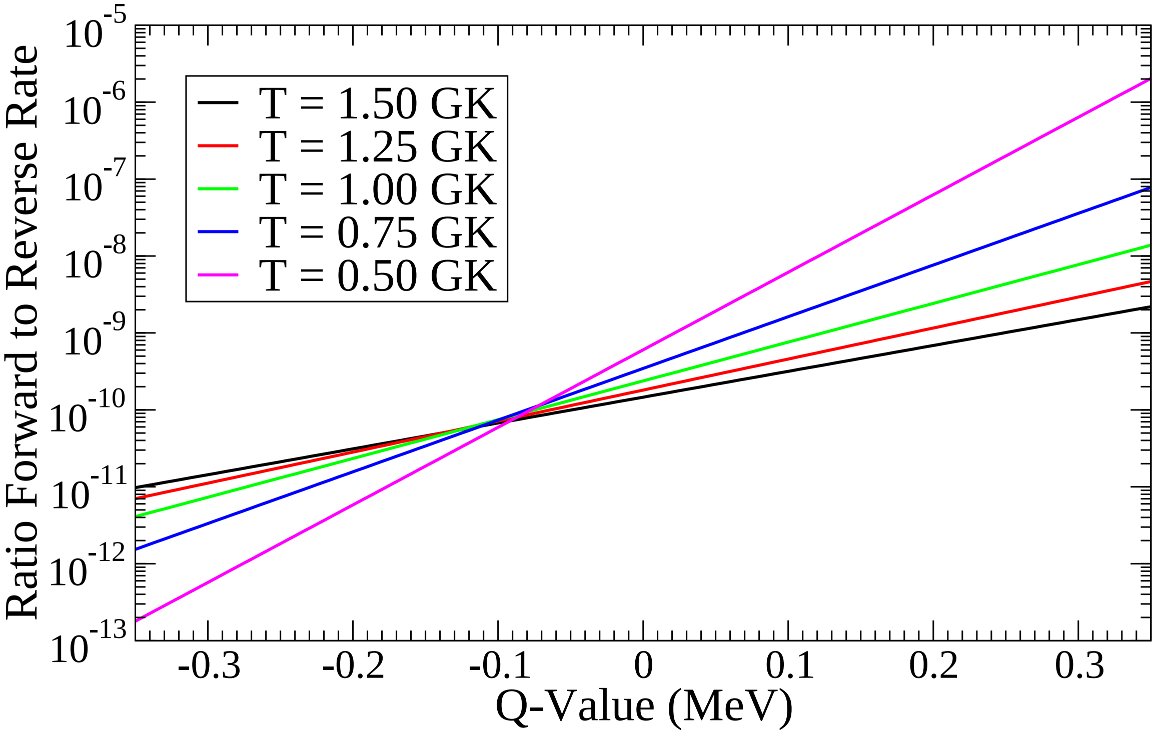

Figure 2.13: Ratio of the ^{64}Ge$(p,\gamma)^{65}$As to the ^{65}As$(\gamma,p)^{64}$Ge rate as a function of the Q-value

Figure 2.13 shows the ratio of ^{64}Ge$(p,\gamma)^{65}$As to the ^{65}As$(\gamma,p)^{64}$Ge rate as a function of the Q-value within this current uncertainty for the Q-value. From this we see the ratio, which defines the abundance of ^{65}As, can vary by up to seven orders of magnitude. To look at this effect the calculation was done again for an accretion rate of $\dot{m}/\dot{m}_{edd} = 0.30$, where nothing is changed in the network other than the ^{65}As$(\gamma,p)^{64}$Ge reaction rate by changing the Q-value to the minimum and maximum value within the current error bars. The results of this are shown in Figure 2.14 and Figure 2.15. Figure 2.14 is a plot of the temperature as a function of time for each of these cases. The solid black line represents the case where the Q-value is the minimum and the dashed line expresses the case where the Q-value is the maximum (The beginning is exactly the same as this is where the burning is below ^{64}Ge). There are clear distinctions between these two calculations later in the burst. Once burning passes ^{64}Ge the higher Q-value calculations defines a higher burst temperature and then eventually cools about 100 seconds earlier than the lower Q-value calculation.

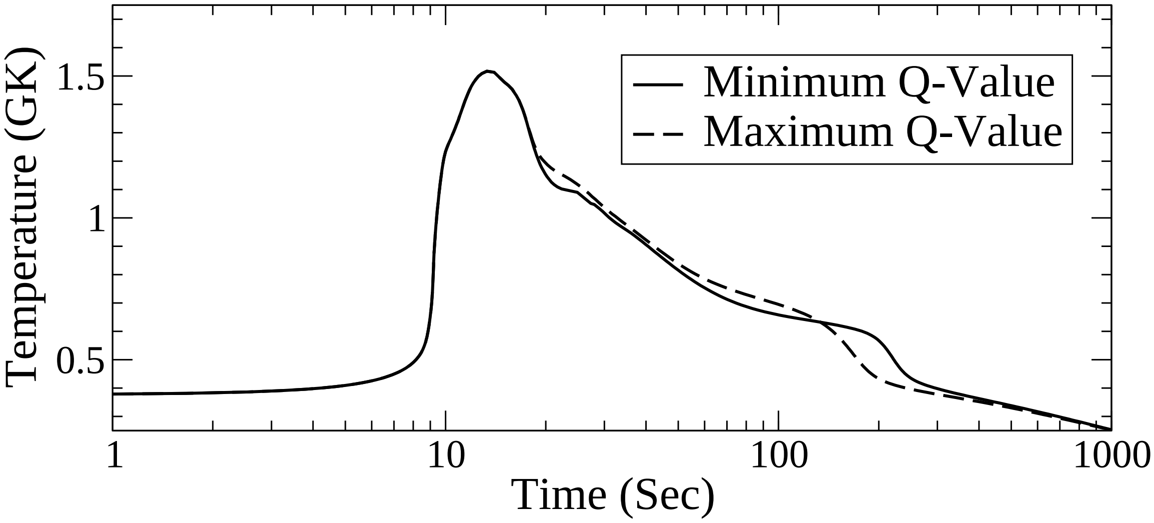

Figure 2.14: Temperature profile for burst with different extreme $^{65}\text{As}(\gamma, p)^{64}\text{Ge}$ reaction rates from the Q-value

Figure 2.15 shows the mass fraction of the waiting point nuclei. The top figure is for the case where the Q-value is a minimum and the lower figure is for the largest possible Q-value within the current uncertainty. From this we can see the abundance of ^{65}As is about 3 orders of magnitude larger in the case of maximum Q-value which causes the abundance to go very quickly past ^{64}Ge up to ^{68}Se. In the top figure there is approximately 100 seconds between the time when ^{64}Ge peaks in abundance until ^{68}Se peaks. For the lower figure with high Q-value this occurs in only 10 seconds. The overall abundance pattern is not significantly changed from this alone as there are still potential waiting points at ^{68}Se and ^{72}Kr. It should be noted that the masses of ^{69}Br and ^{73}Ru are also very uncertain. If the mass of ^{65}As is measured and results in a Q-value that is on the larger end, then measurements of these other masses will become critical. But if the Q-value is closer to the lower end then this will always stall the energy generation and limit the production of heavier elements, regardless of the availability of fuel.

A study was done by Brown et.al [27], in which the influence of the proton separation energies were calculated for each of the key waiting point nuclei. This was done using maximal and minimal mass model predictions in addition to new calculations

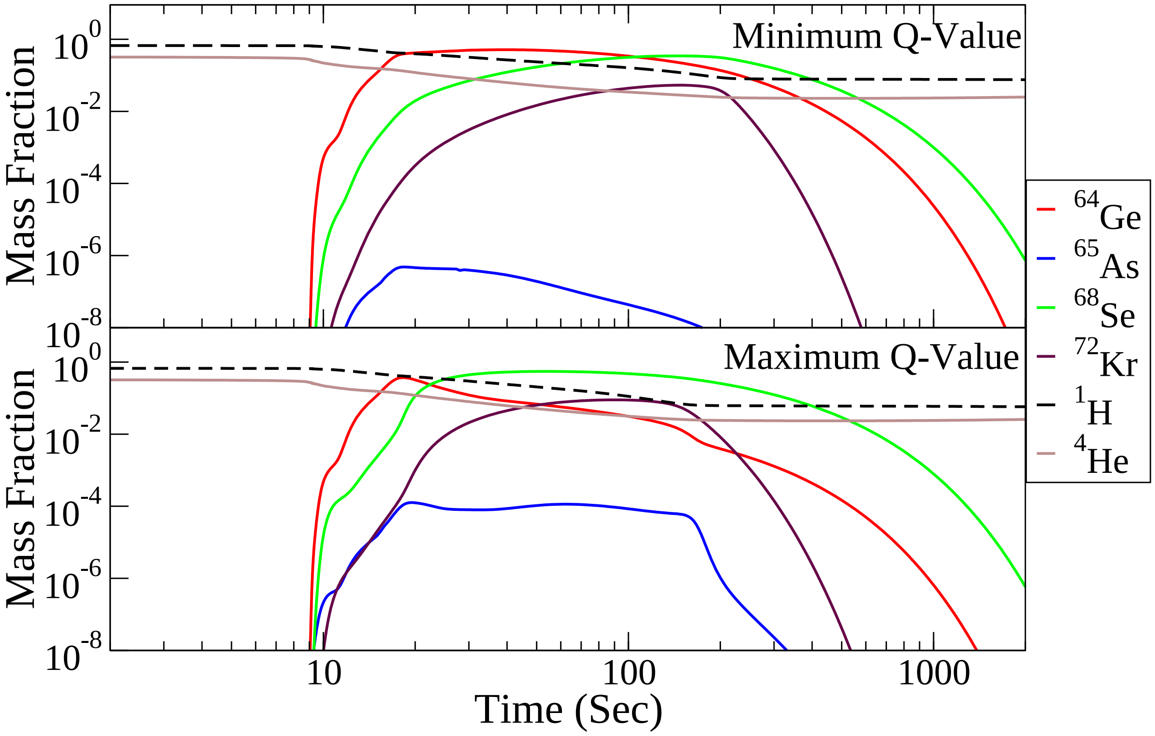

Figure 2.15: Mass fraction of waiting point nuclei for two extreme ^{65}As$(\gamma, p)^{64}$Ge reaction rates

of the separation energy. The conclusions of their work is similar to this as they also point to the need for mass measurements in the range of $A = 64 - 74$ on the rp-process path. There are differences in the burst characteristics between GAMBLER and the work of Reference 27, the burning occurs all the way up to the SnSbTe cycle whereas the GAMBLER calculations suggest that the star cools and prevents all the fuel from being consumed. It is not clear why these two calculated results differ. More detailed investigations of the differences between the cooling in both programs would be required to better understand this.

2.9 Conclusions

Using a 1-zone model which incorporates a large nuclear network, it is shown that for a mass accretion rate of $\dot{m}/\dot{m}_{edd} = 0.01$ or higher there will be nuclear burning up to ^{64}Ge. How far beyond this depends critically on nuclear physics inputs. The most critical of these is the mass of ^{65}As and the recently measured mass of ^{64}Ge. It is also shown that production to heaver rp-process nuclei is not determined solely by the abundance of hydrogen. Indeed, the burst will stall at the ^{64}Ge waiting point regardless of the amount of hydrogen fuel remaining if the Q-value for ^{64}Ge$(p, \gamma)^{65}$As is sufficiently negative. If the Q-value is on the high side of the currently allowed range, burning through ^{65}As can proceed an order more rapidly and the network can proceed to ^{68}Se where the mass of unbound ^{69}Br will become critical. Other properties, such as levels in ^{66}Se, could play a role in these latter processes because nuclear statistical equilibrium is not attained between these abundances. In this case the reaction rate for ^{65}As$(p, \gamma)^{66}$Se could speed up the process from ^{65}As to ^{68}Se. The temperature profile and the luminosity also depend on the Q-value for proton capture on ^{64}Ge and the corresponding mass of ^{65}As. In summary there are a range of accretion rates where a measurement of the mass of ^{65}As can be critical to understanding X-ray bursts on the surface of accreting neutron stars.

Chapter 3

Experimental Design

3.1 Introduction

It was shown in Chapter 2 that the rp-process beyond ^{56}Ni will be affected by the masses of ^{64}Ge and ^{65}As, and possibly by their energy levels when not in equilibrium. An experimental program is therefore necessary to measure these important properties. This will reduce the uncertainty in network calculations and achieve a better understanding of the rp-process occurring on the surface of neutron stars in binary systems.

There are several methods to measure nuclear masses and energy levels for these nuclei. It is important to determine which method will give the necessary resolution to address the nucleosynthesis problems of Chapter 2.

The temperature on the surface of a neutron star during the rp-process X-ray burst was calculated to be between 0.3–1.6 GK, which translates to a thermal kinetic energy of 25–137 keV. The photo-disintegration reaction rate is proportional to $exp(Q/k_bT)$; the required Q-value resolution will be on the order of k_bT. If one recalls Figure 2.13 in Chapter 2, an uncertainty in the Q-value of 25 keV would reduce a 7 order of magnitude uncertainty in the reaction rate down to about a factor of 2–3 uncertainty. The goal is therefore to measure the mass of ^{65}As and ^{64}Ge to 25 keV. For resonant state information the required accuracy in Q is not that easy to characterize because the location of the Gamow window, and the width of the Gamow peak is rather broad. It is nevertheless important to determine the existence of states within the Gamow window. The mass of ^{64}Ge has recently been measured using the Canadian Penning Trap (CPT) [25], however at this time the results have not been published. The unpublished results suggest a final measured mass value accuracy of ±40 keV. We will also measure ^{64}Ge, along with ^{65}As as part of our measurement program.

3.2 Choice of measurement technique

There are several different techniques for measuring nuclear masses, each with its advantages and disadvantages. The techniques can be divided into two categories: direct and indirect methods. Direct methods imply the mass is the measured quantity. (However, all methods are somewhat indirect as they rely on calibrations.) Indirect methods are those where the mass is calculated from measurements of other quantities. Some examples are given below that clarify these distinctions. .

3.2.1 Direct Methods

Time of flight techniques have been widely used in the past for measurement of ground state masses [28, 29]. This is a direct method in which one measures the time, distance, and energy and then calculates the mass. It has been performed using cyclotrons [30], mass spectrometers [31], and storage rings [32]. The resolution one can achieve by time of flight is usually limited by the flight path. Typically one can obtain resolutions on the order of 100's of keV. This resolution is therefore unsuitable for mass measurements relevant to the rp-process.

Penning traps are very powerful tools for precision mass measurement. They provide direct measurements of the mass and are capable of mass resolution of about 10 keV [33, 34]. These measurements are typically quick and fairly straightforward.

This is probably the best currently explored technique for measuring the mass. In order to achieve the optimum resolution a trapped ion must be excited for a sufficient amount of time before extraction. This combined with the time required to produce the rare isotope and capture within the trap make mass measurements of short lived nuclei difficult. Penning trap measurements are also limited to ground state or long lived isomeric states. Information about short lived excited states is not accessible using this method.

3.2.2 Indirect Methods

The beta endpoint technique is an indirect method. In this technique, one measures the beta decay energy spectrum from a beta unstable nucleus and extrapolates the beta spectrum to the beta endpoint where the neutrino is at zero energy [35]. This gives a measure of the Q value of the reaction that is directly related to the mass difference between the parent and the daughter nucleus. The main difficulty with this technique is determination the endpoint of the spectrum. For the specific cases of ^{64}Ge and ^{65}As this requires production of, and implantation of, these nuclei into a detector system. Typically one may hope to achieve a mass resolution of about 50 keV for beta endpoint measurements.

Transfer reactions are another indirect measurement. Here again, the Q-value of a reaction is measured, from which one can calculate the mass of the nucleus of interest, provided the nuclear other particles involved in the reaction have well measured masses. Transfer reactions can have large cross sections suitable for measurements at low beam intensities. The use of hydrogen and deuterium targets can allow high resolution measurements of reactions such as (p,d), (p,t), and (d,p) in inverse kinematics. For example, one can bombard a hydrogen target with a neutron deficient ^{67}As rare isotope beam and use the (p,d) or (p,t) reaction to produce the more exotic ^{66}As or ^{65}As nuclei and measure their masses.

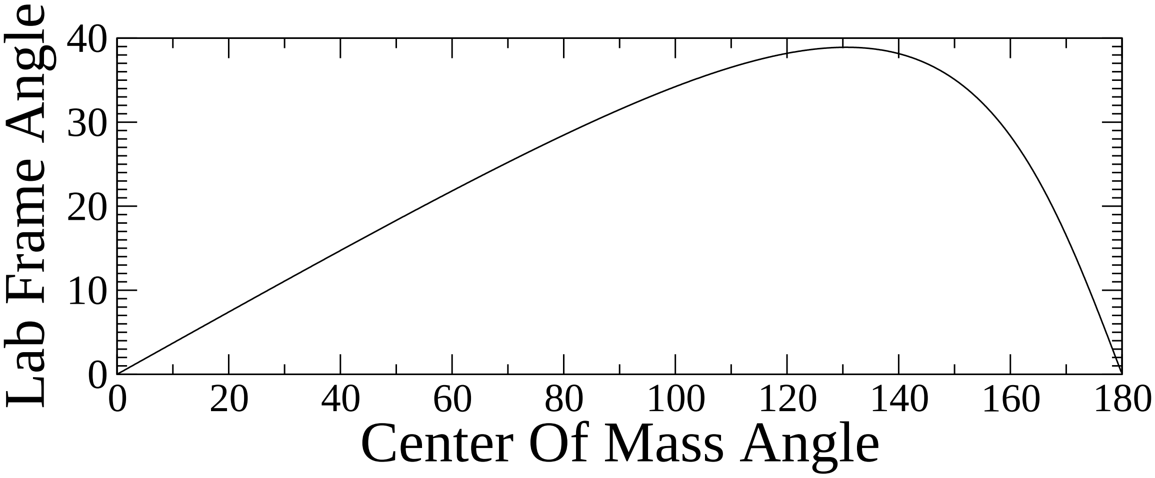

Figure 3.1: Lab Vs. Center of Mass Angle

3.2.3 Using (p,d) in Inverse Kinematics

The (p,d) reaction in inverse kinematics is well suited for fragmentation facilities such as the NSCL. Historically reactions of the type (p,d) were performed with a proton beam impinging on a heavy target. The target nucleus would then transfer a neutron to the proton to form a deuteron. In inverse kinematics, a heavy beam impinges on a proton target. In the center of mass, the reaction is the same however, the kinematics are quite different.

Figure 3.1 shows the center of mass angle Θ_{cm} verse the lab angle Θ_{lab} for a deuteron from the reaction ^{66}As(p,d)^{65}As in inverse kinematics with a beam energy of 60 MeV/u. As one can see, there is a maximum lab angle around 40 degrees. At smaller lab angles there are two different angles for each center of mass angle. This can be understood by looking at a velocity diagram for the deuteron.

Figure 3.2 shows this view for the velocity of the deuteron. The circle represents the velocities of the deuteron corresponding with energy in the center of mass. The velocity of the center of mass is represented by the center of mass velocity vector. With beam energies around 60 MeV/u the velocity of the deuteron in the lab frame is always at forward angles. This can be understood by summing the deuteron velocity vector in the center of mass and the center of mass velocity vector. One can also

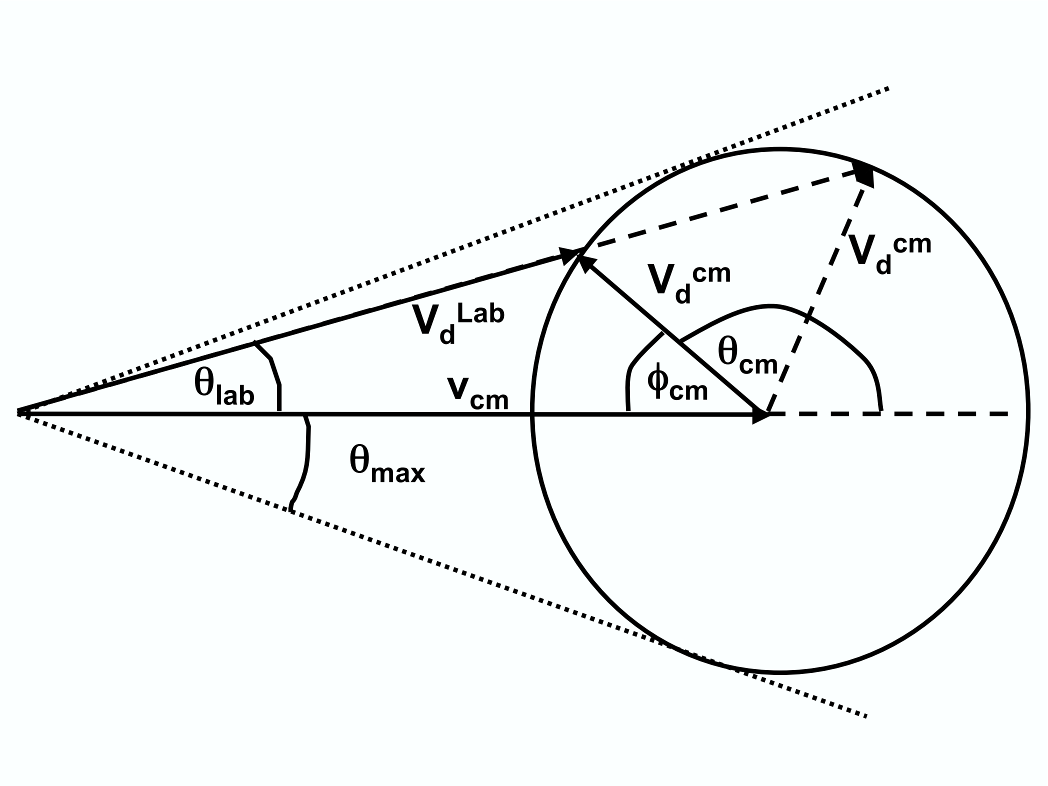

Figure 3.2: Lab frame kinematics

understand why there will be two different deuteron energies at a single angle in the lab. One comes from emission to forward angles in the center of mass frame, and the other from emission to backward angles in the center of mass frame.

The cross section in the lab is also quite different in inverse kinematics. A comparison between the cross section for the ^{65}Ge(p,d)^{64}Ge reaction in the center of mass frame and its value in the lab frame is shown in Figure 3.3. The top graph is the cross section in the center of mass frame. It decreases rapidly with center of mass angle. The lower graph is the corresponding cross section in the lab frame. The cross section is almost constant at small center of mass angles. The solid line represents the the angles between 0–90 in the center of mass, and the dashed-dotted line represents the angles between 90–180 in the center or mass.

Figure 3.4 shows the deuteron energy in the lab frame versus the lab angle in

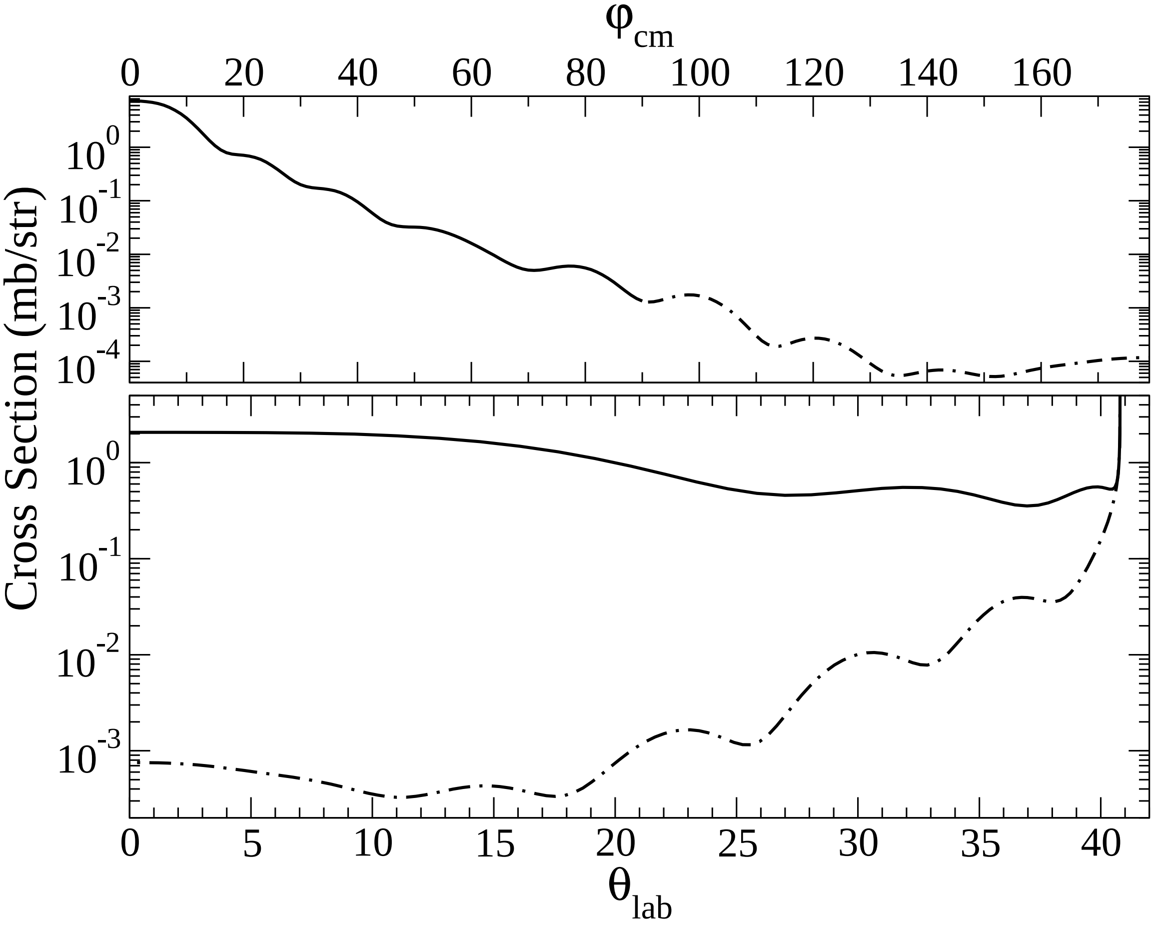

Figure 3.3: Cross section for ^{65}Ge(p,d)^{64}Ge at 60 MeV/u in the center of mass and lab frame

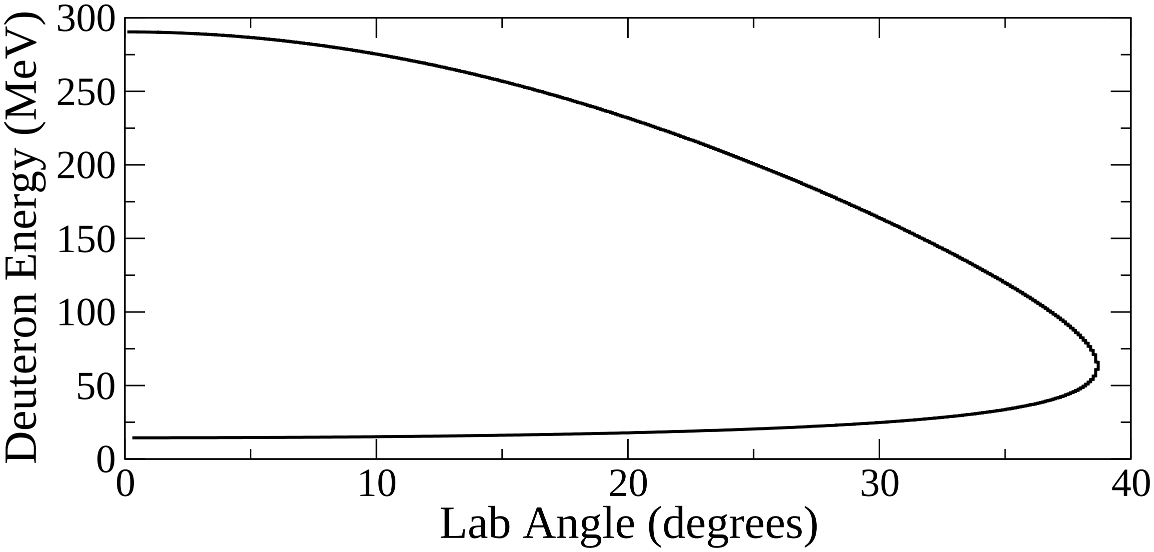

Figure 3.4: Deuteron energy Vs. lab Frame angle from ^{66}As$(p,d)^{65}$As at 60 MeV/u

degrees. The low energy deuterons are from the small values of ϕ_{cm} angles in the center of mass where the cross section is largest. The very high energy deuterons are emitted at large angles ϕ_{cm} in the center of mass frame.

In order to calculate the mass using a (p,d) reaction one implements the conservation of energy and conservation of momentum. Consider a binary reaction of the form $A + p \rightarrow B + d$, then one can write:

$$\mathbf{P}^i_A + \mathbf{P}^i_p = \mathbf{P}^f_B + \mathbf{P}^f_d \tag{3.1}$$

where

$$\mathbf{P}^i_p = (E^i_p, \overrightarrow{P}^i_p) \tag{3.2}$$

is the 4-vector momentum. Solving $P_i \cdot P^i$ for M^2_B will result in:

$$\begin{aligned} M^2_B &= M^2_A + M^2_p + M^2_d + \\ & 2\left(E_A M_p - E_d M_p - E_A M_d + \sqrt{E^2_A - M^2_A}\sqrt{E^2_d + M^2_d}\cos\alpha\right) \end{aligned} \tag{3.3}$$

where M_A, M_p, M_B, and M_d represent the masses of A, p, B, and d respectively. E_A, and E_d are the energies of A and d respectively. The angle α is the angle between P_A and P_d in the laboratory reference frame. From this one can see the quantities that must be measured in order to calculate the mass of B are the energies of the beam particle A and the deuteron d and the angle (α) between the beam and deuteron.

3.3 Beam Characteristics

The experiments will take place at the National Superconducting Cyclotron Laboratory, which is a fast fragmentation facility. Secondary beams are produced by fragmentation of fast stable beams impinging on a beryllium target. The A1900 fragment separator is used to separate the beam of interest from other fragments. The A1900 is not capable of producing a pure beam of ^{66}As or ^{65}Ge.

Figure 3.5 is a LISE++ Monte Carlo simulation of the fragmentation beam produced from the A1900 [36]. This comes from fragmentation of ^{78}Kr at 140 MeV/u impinging on a 768 mg/cm^2 beryllium production target. There is a 170 mg/cm^2 aluminum degrader at the dispersive intermediate image of the A1900. Both ^{66}As and ^{65}Ge are produced in addition to many lower mass fragments that have the same magnetic rigidity as the ^{66}As within the momentum acceptance of 0.5% defined by slits at the dispersive intermediate image of the A1900. The additional lower mass nuclei can help in the measurement of ^{65}As and ^{64}Ge as they will serve as calibration nuclei, reducing systematic effects.

Beyond the A1900 fragment separator the beam is transported to the S800 spectrometer. There are two modes of operating the S800 ion optics system, focused or dispersion matched. In focused mode the beam is transmitted to the target position with a focus at this location. The beam on target should be an image of the beam at the entrance to the S800. This allows the full momentum acceptance of the A1900 to be transmitted to the target position. In dispersion matching mode, the focus is at the focal plane of the S800 instead of the target. At the target position the beam

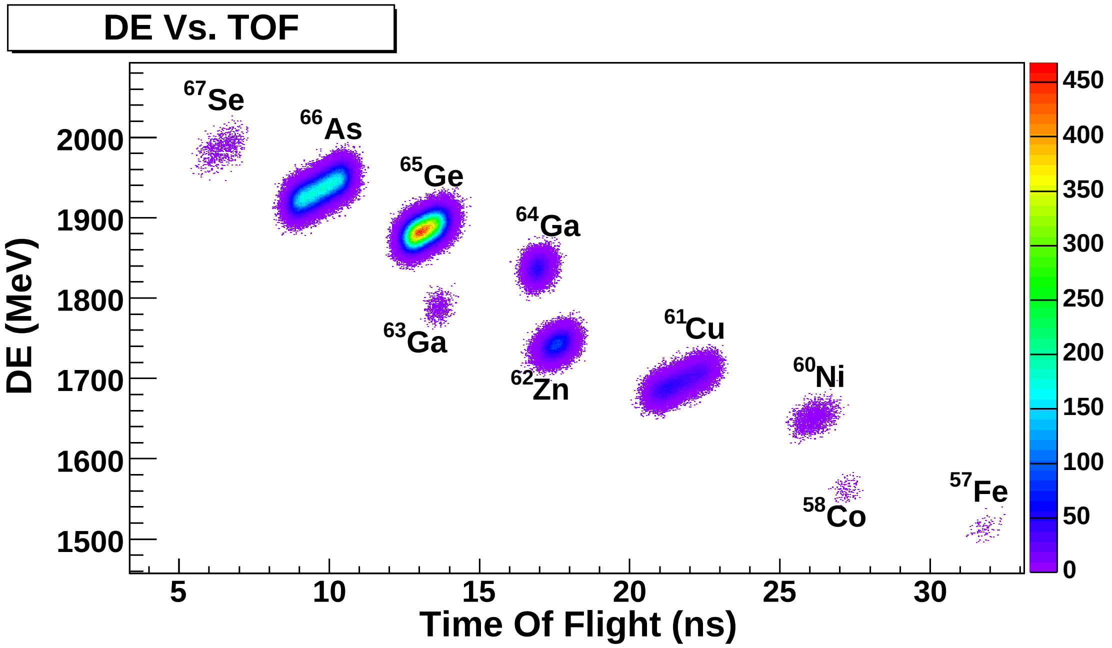

Figure 3.5: DE vs. TOF histogram showing simulated fragmentation beams for ^{66}As and ^{65}Ge

is dispersed in the vertical direction based solely on the the particle momentum. The dispersion at the target position is 10 cm/%dp/p i.e. two beam particles with momentum differences of 0.5% would be physically separated at the target by 5 cm. The beamline is limited to 0.5% momentum acceptance. A measure of the vertical position of the beam particle at the target position would then translate to a measure of the momentum and hence energy of the particle.

3.4 Experimental Resolution

A Monte Carlo simulation of the experiment was done in C++ using ROOT random number generators. The output was recorded in a root file which can be analyzed using the ROOT analysis package.

The program determines how many events to generate based on two input files. One file contains the differential cross section in the lab frame, the other is the angular distribution of charged particle detectors around the target, used for collection of the deuterons. The cross section is calculated using a DWBA program. The cross section and angular coverage are then folded together to produce a probability distribution for outgoing deuterons. The particle beam rate and beam time are given as inputs, as well as the target thickness. All of this is used to determine how many reactions will occur and how many will be detected in our system. The simulations takes into account interactions in the target, the position and energy resolution of the HiRA detector, which is used to measure the deuteron, and the properties of two micro channel plate detectors used to measure the beam characteristics.

3.4.1 Beam Energy Effects

In focused mode one can accept more beam, up to 1.3% based on particle ID constraints in the S800 focal plane. In order to measure the beam energy in this mode one must rely on timing information. The uncertainty in energy from timing can be estimated classically by $E = (1/2)MV^2$, so the uncertainty $\Delta E/E = 2\Delta V/V$. The uncertainty in V comes from the uncertainty in flight time, and flight path. Estimating the flight path variations involves optics calculations and a good measure of the trajectory of each ion. If one ignores this and calculates an uncertainty assuming a timing resolution of 600 ps for the MCP and 200 ps for the plastic, the energy resolution is 0.54%, which will contribute 71 keV to the FWHM of a mass peak. As this estimate ignores the effects from the flight path, it only represents a lower limit on the resolution.

In dispersion matching mode the energy is measured by relating the position at the target to momentum. Therefore a measure of the vertical position of the ion will give one the energy. The uncertainty in energy from this method can be estimated based on the dispersion matching of 10 cm/%dp/p which corresponds to 5 cm/%dE/E. A measure of the position to 1 mm would give 0.02% in energy. This would contribute less then 10 keV to the FWHM of the mass peak.

A systematic shift of 1 mm on the position measurement will only shift the mass peak by 2.5 keV due to the shift in beam energy calculated.

3.4.2 Target Effects

The target nuclei we are using is hydrogen. We have 2 choices for the target, the first is some sort of plastic target, such as polyethylene, which is readily available in many different thickness. The disadvantage of plastic is the contamination of carbon. Polyethylene is only 1/7 hydrogen by mass. The alternative is to use pure hydrogen in the solid, liquid, or gas form. Gas will not work as the effective thickness is too small, even with an extended length target. Liquid and solid hydrogen can work, however they must be cooled using liquid helium. It is also difficult to produce a solid or liquid target that is thin enough and uniform enough in thickness. If one has entrance and exit foil then one has to deal with contamination again. It was decided the technical difficulties of producing a thin windowless uniform solid hydrogen target was not feasible for the purpose here. We will therefore look into the effects on resolution from the polyethylene target.

The target thickness affects the resolution in several ways, the first over all statistics. A thicker target generate more reactions giving more statistics. Thicker targets can have adverse effects on the resolution in several ways. When the heavy beam particle hits the target it will travel some distance into the target before interacting with a proton, causing a (p,d) reaction. The beam particle will loose energy prior to the reaction. The generated deuteron will then transverse the rest of the way out with some new angle. There are potentially 4 effects to consider within the target. The first two are the change in energy and angle of the incoming particle before interaction, the other two are the energy and angle of the deuteron after interaction.

The energy loss of a charged particle traveling through a medium is characterized by the Bethe formula given by

$$-\frac{dE}{dx} = \frac{4\pi e^4 z^2}{m_0 v^2} NZ \left[ln\frac{2m_0 v^2}{I} - ln\left(1 - \frac{v^2}{c^2}\right) - \frac{v^2}{c^2}\right] \tag{3.4}$$

where dE/dx represents the specific energy loss, v is the velocity of the beam, z is the charge of the beam particle, N is the number density of the target, Z is the atomic number of the target, m_0 is the rest mass of an electron, e is the charge of the electron, and I represents the average excitation and ionization potential of the target.

The average energy loss in Equation 3.4 is due to interactions with electrons in the target. This is treated as a statistical process, therefore the energy loss distribution can also be calculated. It will have some statistical distribution in energy, which is called the energy loss straggling. This is typically given in terms of the standard deviation, sigma, of a Gaussian distribution peaked at the expected energy loss. The interactions in the target can also cause the trajectory of the particle to vary, which is called angular straggling.

To give some sense for these effects we note that the energy loss of a 60 MeV/u ^{66}As nuclei in a CH_2 target of thickness 1 mg/cm^2 is about 11.8 MeV, with a straggling width of 273 keV. The interaction depth in the target is random, therefore the energy loss due to the variation in the interaction depth will provide the main contribution to the uncertainty in energy, and the contribution from energy loss straggling will not be significant in comparison. The angular straggling of the beam is only 0.22 mrad and as we see later, this angular straggling will not significantly contribute to the resolution. Therefore in the simulation, the energy loss of the beam particle is considered, but the energy and angular straggling are ignored.

The outgoing deuteron of interest for mass measurements will have an energy between 14–21 MeV. The energy loss in the same CH_2 target of thickness 1 mg/cm^2 will be 64 keV with a straggling of 8 keV. The angular straggling is 1.9 mrad. The pitch of silicon strip detectors in the HiRA telescopes define the detector angular resolution for the deuteron. With HiRA 50 cm away from the target, this corresponds to a standard deviation angular uncertainty in the detection angle of 1 mrad. Angular straggling is comparable to this contribution in angular uncertainty. When one considers the position measurements at the target and upstream from the target, one

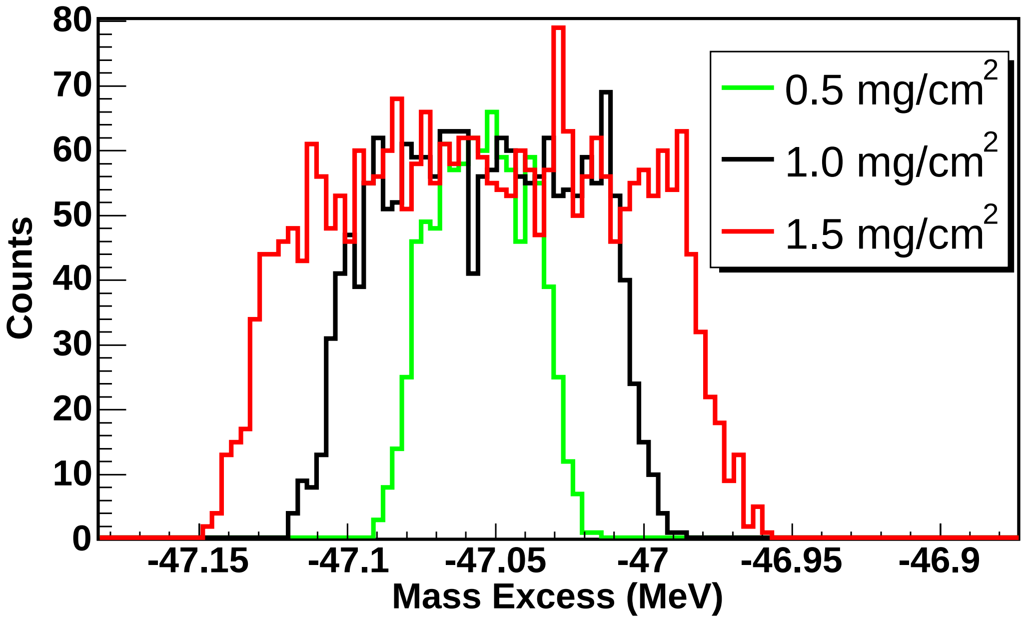

Figure 3.6: Mass peak resolution from target thickness only

finds the total angular resolution is between 3.2–4.8 mrad.

Figure 3.6 demonstrates the effect the target thickness has on the mass resolution. Shown here is the mass spectrum simulated with all numbers measured perfectly. The only effect considered here is the finite thickness of the target. The statistics increases linearly with target thickness, however the width increases simultaneously. Shown here are the results for thicknesses of 0.5, 1.0, and 1.5 mg/cm^2. Table 3.1 gives the value of the FWHM and the uncertainty in the centroid for each target thickness considered.

The actual simulations randomly choose an interaction point in the target. This is done with a uniform probability though the entire thickness of the target. The energy loss of the beam from entrance to interaction point is calculated. This is followed by the calculation of the energy of a deuteron coming out with an angle based on the weighted distribution of cross section and angular coverage. The energy loss of the deuteron is then calculated for the remainder of the target along the trajectory of the deuteron. All of this is done using a large table look up routine that come from the program LISE++. The mass calculation is done by assuming the interaction point is at the center of the target for each event.

Table 3.1: The effect on mass resolution for different thickness CH_2 targets

Thickness mg/cm^2	Number of Events	FWHM keV	Error keV
0.5	99	35.7	3.5
1.0	201	73.9	5.2
1.5	303	107.4	6.1
2.0	404	142.2	7.1
2.5	513	179.2	7.9
3.0	617	213.7	8.6

Table 3.1 show the resolution effects the target has on the final calculation of the mass. The thickness given is the actual thickness of the target, the effective thickness is twice this, as the target will be rotated by 60 degrees with respect to the beam axis for reasons discussed later. The FWHM is $2.35 \times RMS$ for the spectrum and the error is calculated by $FWHM/\sqrt{N}$. It should also be noted that the distribution from the target is not a Gaussian, but more like a square distribution based on the random interaction point. From this one can see that the target itself will not cause a problem in terms of the statistical error in the mass, however the FWHM of the mass peak will be important. Minimizing the FWHM will allow one to separate states that are close to the ground state, or separate states that are in the relevant energy for the rp-process. With this in mind the results would suggest a target thickness of 1.0 mg/cm^2 or less for this experiment.

There are two systematic effects to consider in the target. The first is the absolute thickness. If the thickness is 10% different than the expected value the FWHM will not change, however it mass peak will shift by 3 keV. For thin targets a thickness measurement can be done using an alpha source. There can also be problems if the uniformity is not good as the thickness will depend on the target position. As it will be discused later, the position on the target will be known for each event and the same technique using the energy loss can be used to measure this effect and correct for it.

Table 3.2: Simulated resolution effect from deuteron energy measurement

FWHM resolution in Deuteron Energy (keV)	FWHM resolution in Mass (keV)
30	56
40	75
50	91
60	112
70	131
80	150
90	169
100	188

3.4.3 Deuteron Energy

The Deuteron Energy will also contribute to the mass resolution. The resolution of the deuteron will depend on the energy resolution of the HiRA detector, where the deuteron is stopped. It will also depend on the target as previously described.

Table 3.2 shows the FWHM resolution of the mass for different FWHM resolutions on the deuteron energy. Above 50 keV FWHM this becomes a problem. There are potential systematic problems if the energy calibration is not good enough. If the calibration of HiRA is off by 20 keV this will shift the mass peak by 35 keV which would be beyond the uncertainty with which we intend to measure the mass to. We must be able to calibrate the deuteron energy to better than 10 keV, ideally better then 5 keV.

The energy calibration can be done with a ^{228}Th source which has several energy α's. The highest energy is 8.7 MeV, which is not too far from the expected energy of the deuteron. The pulse hight defect between deuterons and alpha particles should not be to different allowing a calibration with alpha particles. There are also systematic effects from the dead layer on the silicon. Measurements using a source suggest the energy loss in the layer will be around 10 keV which can be corrected for.

Figure 3.7 shows the linear relationship between the resolution in HiRA and the resolution in mass. The slope of this line is 1.88. This means an increase of 10 keV in

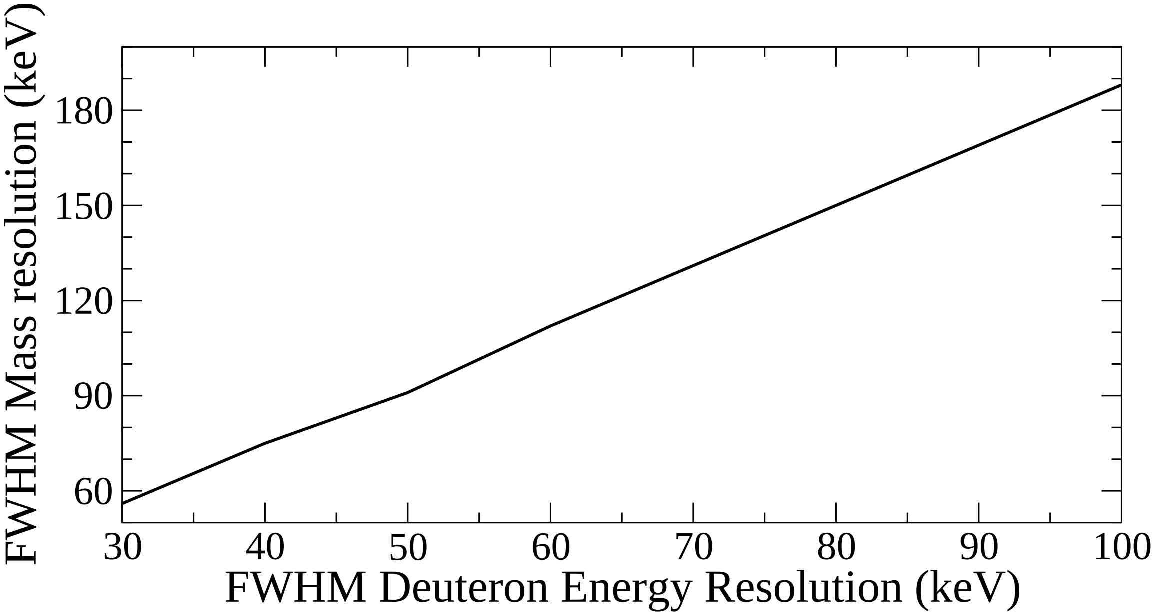

Figure 3.7: Deuteron energy resolution vs mass resolution

HiRA will increase the mass resolution by about 19 keV.

3.4.4 Reaction Angle

The overall mass resolution depends on the angular resolution, this stems from the fact that we use the measured deuteron energy to determine the mass. There is a strong dependence between energy and angle at large angles but not as much at small angles. This is known as kinematic broadening. Figure 3.8 is a graph of the deuteron energy vs the lab angle, as shown in Figure 3.4. This figure shows only the angles where the deuteron energy is below 50 MeV. The slope of this curve represents the kinematic broadening. Thus it is important to understand the various sources of the uncertainty in the scattering angle. Because of the large kinematic broadening at large angles, one expects a greater sensitivity to the angular uncertainty at large angles.

Figure 3.9 is a histogram of the mass calculated assuming no target effects but including deuteron energy, beam energy, and reaction angle effects. Shown in black is the full set of data covering angles up to 24 degrees. Because the kinematic broadening

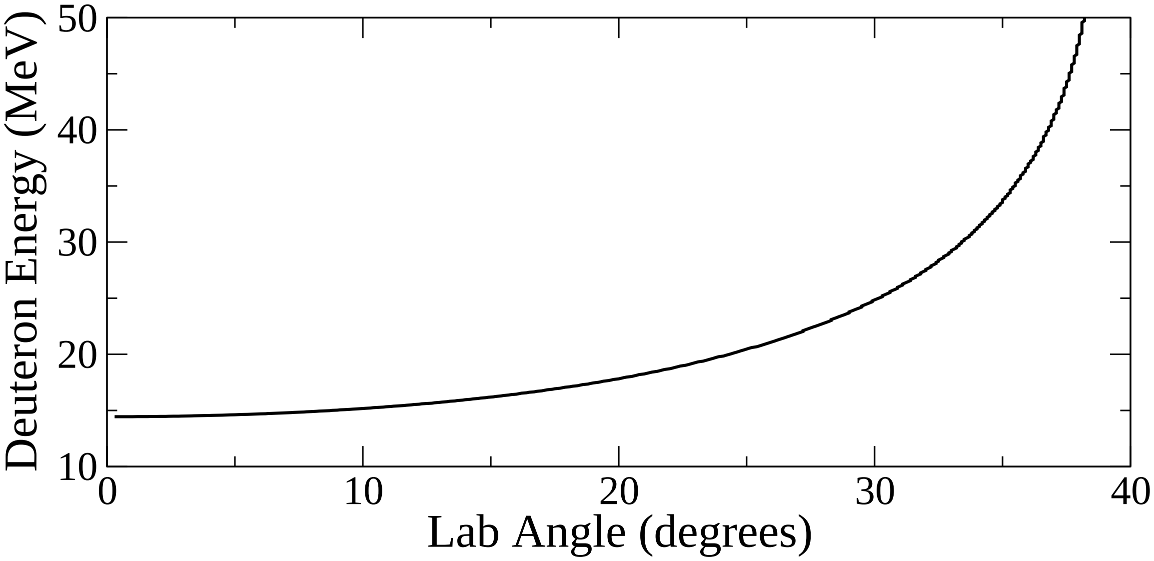

Figure 3.8: Deuteron energy Vs. lab angle at low energy

is less at smaller angles, we might expect a better resolution if the detected angles are limited to smaller angles. The red line is the same histogram, only considering events with reaction angles below 13 degrees. The green peak is also the same, only considering events with reaction angles below 7 degrees. The statistics become very low for smaller and smaller angular cuts however the FWHM of a Gaussian fit to each peak shows the resolution decrease from 120 keV to 112 keV, finally to 96 keV.

The reaction angle effects are the most difficult aspect to simulate as the measurements depend on three different position measurements with many variations on the experimental setup that will affect the reaction angle. There are also effects such as kinematic broadening where the overall resolution will be different at different angles.

The reaction angle is measured directly by measuring the position of the incoming beam particle after the last magnetic element followed by a measurement at the target itself. The outgoing deuteron is measured with a position sensitive silicon strip detector. Therefore the FWHM resolution on angle will depend on the position resolution of all three detectors as well as the physical distance between them. To begin with we look at the effect the silicon detector position resolution has. The detector, which is discussed in great detail in Chapter 4, has a position uncertainty

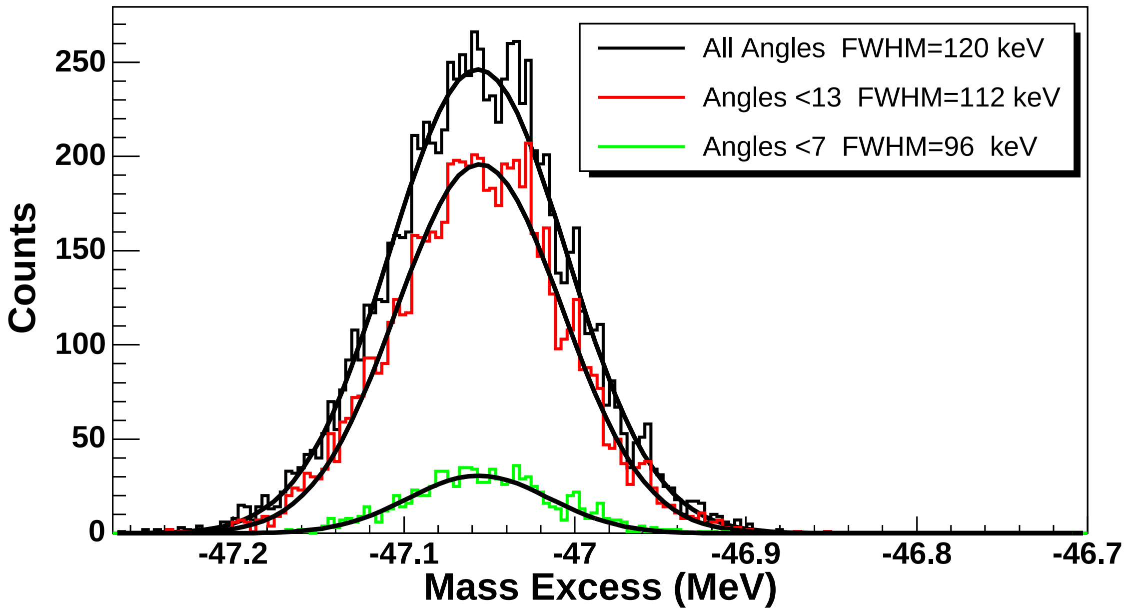

Figure 3.9: Demonstration of kinematic broadening effect

Table 3.3: Simulated resolution effect from position resolution in HiRA

Distance (cm)	FWHM resolution (keV)	Error in FWHM (keV)
35	77	4.0
40	63	3.6
45	52	3.3
50	44	3.2

of 0.9 mm in both the X and Y direction. This comes from the fact that the detector is a double sided silicon strip detector with a strip pitch of 1.8 mm.

Table 3.3 shows the FWHM resolution and error in the FWHM as a function of the distance between the target and the HIRA silicon strip detectors. The range of 35–50 cm is fixed because the chamber is not large enough to allow the distance greater than 50 cm. Below 35 cm the detectors can lose particles that enter the CsI with too large of an angle. The numbers suggest that all distances would be fine with the additional counts compensating for the loss in resolution. There are other factors to consider.

The maximum lab angle for emission of a deuteron is 39 degrees, at 60 MeV/u,

Table 3.4: Simulated resolution effect from position resolution of MCPs

FWHM MCP res (mm)	Mass FWHM res (keV)
0.5	35
1.0	73
1.5	108
2.0	145
2.5	180
3.0	218

however the energy of the deuteron at such large angles will be high enough to punch through the silicon detectors in HiRA and stop in the CsI(Tl) detectors. This will reduce the energy resolution significantly as the energy resolution of the CsI are worse than that of the silicon detectors and would completely dominate the overall energy resolution making it much worse. Thus the practical maximum angle is where the deuteron can be stopped in the silicon detector. For the 1.5 mm thick silicon detectors this is about 24 degrees. With the full HiRA array centered around the beam and at 50 cm from the target the coverage is almost complete up to 24 degrees. Therefore the HiRA array was set at 50 cm from the target, with a 44 keV contribution to the mass resolution, based on its angular resolution.

The incoming angle and position of interaction in the target are measured by two micro channel plate detectors. One is located at the target position while the other is placed upstream at a distance 50 cm from the target. This is the maximum distance that will fit within the scattering chamber.

Table 3.4 shows the effect the position resolution of the two MCPs will have on the mass resolution. To look at the total effect the measured reaction angle will have the simulation was run assuming HiRA is 50 cm from the target and the upstream MCP was also 50 cm from target. This takes into account the resolution of both MCPs which have a Gaussian distribution in X and Y, and the Silicon detector, which has a square distribution in X and Y.

Table 3.5 shows the overall resolution effect on the mass based on the angular

Table 3.5: Simulated resolution effect from total reaction angle

FWHM MCP res (mm)	FWHM angle (mrad)	Mass FWHM res (keV)
0.5	3.2	56
1.0	4.8	82
1.5	6.8	115
2.0	8.9	148

resolution which is defined by the position resolution of the MCPs, and the position resolution of HiRA. An MCP resolution better then 1.5 mm will be important for separating low lying states. The systematic effects are also very important since the reaction angle is calculated by three measured points in space.

In order to measure the absolute positions, a new position measuring system has been developed. The system is called the Laser Based Alignment System (LBAS). It works by mounting a distance measuring laser on two computer controlled perpendicular rotation stages. Both MCPs and the HiRA silicon detectors are mounted on the same table so LBAS can be mounted on the same platform and position measurements can be done relative to each other. This should be sufficient to calibrate to better than 1 mm. A systematic shift of 1 mm will result in a shift of 4 keV in the mass spectrum.

3.4.5 Total Resolution

The contributions for each of the three measured quantities, deuteron energy, beam angle, and beam energy have been investigated individually based on the resolution of the detectors and methods used to measure them. The effects of a finite target thickness has also been investigated. How do they all add up is now the question. First consider the resolution based on the best estimate of the experimental resolutions. With the HiRA array and upstream MCP at 50 cm from target, assuming an energy resolution in HiRA of 50 keV, an MCP position resolution of 1 mm, a target of 0.5 mg/cm^2, one estimates a FWHM mass resolution of 180 keV. With the expected statistics this should give a statistical uncertainty in mass of 18 keV. Any levels that are less then 200 keV apart will be difficult to separate and must be analyzed as overlapping states. If one has enough statistics to limit measurements to small angle ($\theta < 10$ degrees) the resolution improves, but does not drop below 110 keV.

3.4.6 Background

The discussion of resolution prior to this assumes the background from other reactions is small. It was stated earlier that the beam would not be pure. This has the advantage of having calibration reactions occurring at the same time. This is the case if they can be cleanly be separated. Simulations of the beam using Lise++ suggest the contaminations will be in the form of an isotone chain. This will work well as the lower Z nuclei have measured masses. The time of flight of each of these nuclei will also be different, with the timing resolution described earlier it should be reasonable to determine which nuclei hit the target based on the timing alone. The S800 will be used to measure reacted products and can give both A and Z identification. When the (p,d) reaction occurs in the target, the remaining residual nucleus will lose one neutron and no protons. The particles will bend into the focal plane based on the magnetic rigidity

$$B\rho = \frac{mv}{q} \tag{3.5}$$

where B is the magnetic field, ρ is the radius of curvature, m is the mass, v is the velocity, and q is the charge. From this one can see that reaction particles, whose velocity will not be dramatically affected will the have a change in $B\rho$ of 65/64 or 1.5%. The S800 has a beam blocker that can be placed to block the unreacted beam. This will allow only the reaction products to arrive at the focal plane. There will also be reactions on the carbon in the target. Earlier test runs suggested that the rate of deuteron production from carbon break up and the (p,d) reaction to be very similar. Measuring the incoming beam particle by two MCP's and upstream plastic scintilators, along with a single deuteron and no other particles measured in HiRA, and the expected heavy fragment in the focal plane should eliminate any significant contamination in the mass peak. Additional cuts can also be imposed by looking at the Energy vs. Angle spectrum of the deuteron. All of these work to make the experiment nearly free from background and contamination.

3.5 Final Results

Based on the detailed study using this simulation, an experimental mass resolution of 25 keV is possible for ground state masses if all systematic effects are carefully calibrated, the energy resolution of the HiRA detector is around 50 keV and MCP positions resolution around 1 mm. Clearly these are possible and care must be taken on all calibrations.

Chapter 4

The High Resolution Array, HiRA

4.1 Introduction

In 1996 the Nuclear Science Advisory Committee (NSAC) published the long range plan which identified as one of the frontiers, the exploration of nuclei far from stability. The study of rare nuclei is critical in understanding not only the astrophysical processes of nucleosynthesis, but also for understanding basic nuclear structure. Most of what is known (experimentally) about nuclear structure comes from experiments involving stable nuclei. The question of how structure evolves with isospin cannot be understood without continuing such studies towards the neutron and proton driplines. Advances in radioactive beam facility such as the currently running Coupled Cyclotron Project (CCP) at the NSCL, and future projects such as RIKEN's BIG RIPS project, GSI's upgrade, and RIA, the next generation US facility, are making it possible to study more exotic and short lived nuclei.

Using projectile fragmentation, as is done at the NSCL and other places, the rate of production typically drops by an order of magnitude for each additional neutron removed as one approaches the end of an isotope chain. In order to study the most exotic nuclei it is therefore critical to use detectors that will cover most, if not all of the interesting cross section. The High Resolution Array (HiRA), was proposed

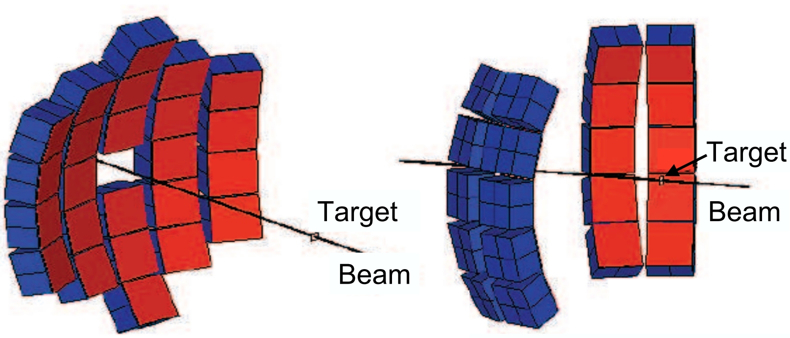

Figure 4.1: Two configurations for HiRA. On the left HiRA is configured at forward angles for transfer reactions or breakup reactions. On the right HiRA is configured for elastic scattering near 90° in the lab.

to fulfill this need of the scientific community for a highly granular, large solid angle charge particle detector.

HiRA is a multi-institute collaboration between the NSCL at Michigan State University, Washington University of St.Louis, The Indiana University Cyclotron Facility (IUCF) at Indiana University, and Instituo Nazionale di Fisica Nucleare (INFN) in Milano, Italy. HiRA is a second generation detector. Many of its features are based on the Large Area Silicon Strip Array (LASSA) [37]. HiRA consists of twenty identical detector telescopes which can be setup in many different configurations depending on the experimental requirements.

Figure 4.1 shows two possible configurations of the telescopes. Some experiments, such as (p,d) transfer reactions in inverse kinematics, require particle detection at very forward angles in the lab frame, while other experiments such as elastic scattering, require particle detection around 90° in the lab. HiRA's modular design facilitates the reconfiguring of detectors as the science dictates.

Figure 4.2 is a representation of the detectors within a HiRA telescope. A telescope consists of two silicon strip detectors followed by four CsI(Tl) crystals, each covering one quadrant behind the silicons. Also contained within the telescope are the pre-amplifiers for the photo-diodes used to readout the CsI(Tl). The silicon detectors will be discussed in detail in Section 4.2 and the CsI(Tl) detectors will be described in Section 4.3.

Each telescope has 100 independent electronic channels for energy and 96 channels for time. The CsI(Tl) are not used for timing. These electronic channels add up to almost 4000 signals to process for the entire array. Traditional electronics, which consists of pre-amplifiers for each channel, 16 channel CAMAC shaper discriminator units, all going into CAMAC or VME ADCs and TDCs cost about $400 per channel. For HiRA this would add up to 1.6 million dollars. It is clear that a new lower cost electronic readout scheme is needed for this array and for any future detector arrays that implement large area highly segmented silicon strip detectors. A major component of the HiRA project, led by the Washington University group, is the development of high density relatively low cost electronics designed for silicon detector signals, in the form of an Application Specific Integrated Circuit, or ASIC called the HINP16 chip. This will be discussed in detail in Section 4.4.

4.2 Silicon strip detectors

Silicon detectors have been widely used for charge particle detection over the past 40-50 years, given the relatively low mean energy for electron-hole production, 3.6 eV. The energy resolution is far superior to scintillators. For comparison a typical scintillator detector with photomultiplier readout takes ∽100 eV to produce one information carrier (photo-electron). Silicon detectors also produce very linear energy response to signals over a large dynamic range of deposition energy with relatively little Z dependence, for $Z < 15$, on the energy response. By segmenting the contacts into strips or

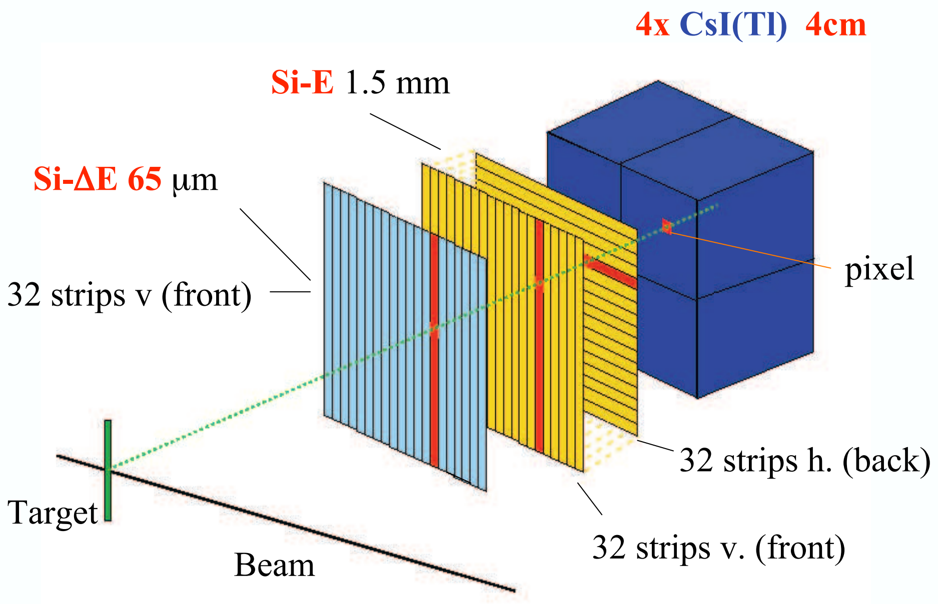

Figure 4.2: Each HiRA telescope contains 2 silicon strip detectors and 4 CsI(Tl) crystals as shown here

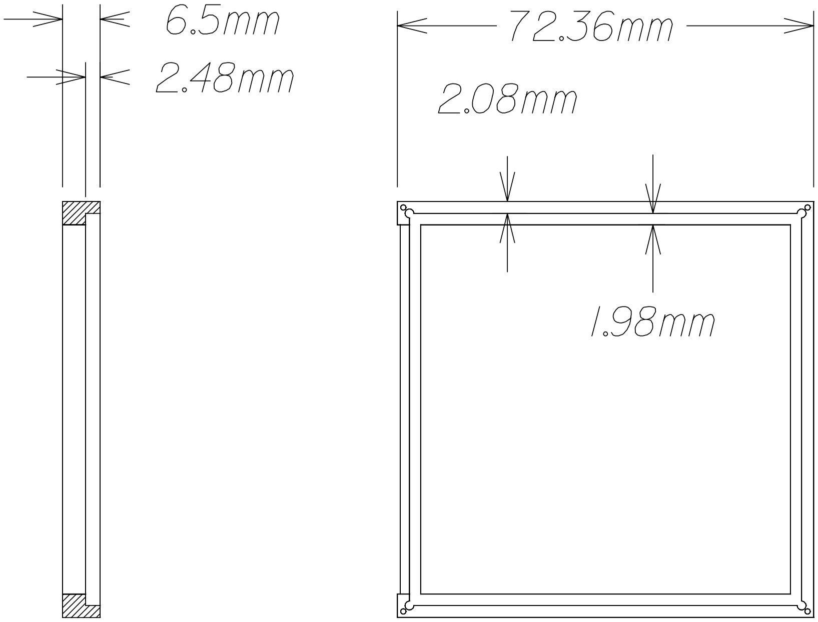

Figure 4.3: The silicon DE frame for HiRA

pads, excellent position resolution can also be achieved. Typical collection times on fully depleted silicon detectors are ≤50 ns, giving excellent timing properties as well. Drawbacks to silicon detectors are the limitations to the size and thickness that can be fabricated, and they are prone to radiation damage.

4.2.1 Silicon detector design

The design for the silicon detectors in HiRA was managed by the Indiana University group who worked closely with the manufacture, Micron Semiconductor [38]. There are several components that make up the HiRA silicon detectors: the silicon wafer, its frame, which supports the silicon, and the cabling from the silicon wafer to an external connector. As with its predecessor LASSA [37], the design for HiRA is optimized for close packing of silicon detectors so as to cover large solid angle. For this reason it was necessary to design a special frame for the silicon detector. Commercially available frames had bulky support structures that prevented close packing.

A frame for the single sided HiRA silicon strip detector is shown in Figure 4.3. The

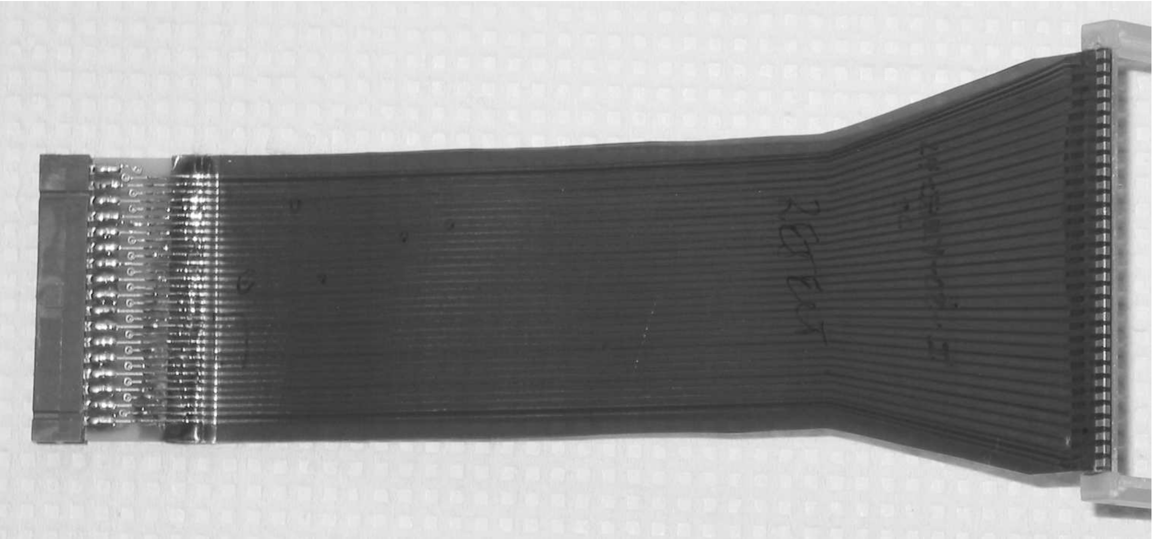

Figure 4.4: The silicon DE frame for HiRA

frame is constructed out of G-10 material with an outer dimension of 7.236 cm. There is an inner ridge where the silicon wafer is epoxied into place. This ridge is recessed into the frame, protecting the silicon and also allowing detectors to be stacked on top of each other. The outer ridge is 2 mm wide and has four through holes, one in each corner, for alignment dowel pins. There is a recessed ledge on one side of the frame and can be seen on the left in Fig. 4.3 where the cable is attached and is recessed enough for wire bonds to stay below the upper surface of the frame. For the frame of the double sided detector another ridge, this one from the bottom, is used for attaching a second cable for the 32 strips on the back side.

In order to readout the signals from the detector, a flexible polyimide cable is used. Figure 4.4 is a picture of a HiRA cable with connector. This cable is epoxied with a sharp 90° bend to the recessed ridge. This allows the cable to go straight back. On the top of the cable there are gold contact pads which allow wire bonding to the silicon surface. HiRA uses three wire bonds from each strip to the cable pad. These wires are very small and can be broken by accidental contact. The cable is 0.246 mm thick, which is thicker than the LASSA cable for more durability. At the other end of the cable there is a small printed circuit board which connects to a standard 0.1” spacing 34 pin female header. The cable is epoxied to the PC board and the traces are soldered on. There are 32 strips on a surface which connect to traces going to pins 2 through 33 of the connector. Pins 1 and 34 are used to connect the back plane of the single sided detector to the ground. On the double sided detector these pins do not connect to the silicon wafer.

There are two different types of silicon detector for HiRA. One is a single sided thin (65 μm) detector and the other is a thick (1.5 mm) double sided detector. The thin detector is denoted “DE” as it is used to measure the energy loss by the particle passing through the detector. This energy loss is used in ΔE vs. E or ΔE vs. Time of Flight particle identification techniques. The other thicker silicon detector, will be denoted as the “E” detector. It is combined with ΔE to get total energy loss or with the ΔE to contribute in ΔE vs. E particle identification plots.

Both the E and DE detectors were built by Micron and carry the catalog designation BB7-65 and BB7-1500 respectfully. The detectors are made of bulk n-type silicon with P+ implantation to form the junction near the front. The surface of both detectors have an active area of 62.3×62.3 mm^2. There are 32 strips on the front (junction) side of the DE and E with a strip pitch of 1.95 mm. There is a gap of 25 μm between active strips and between active strips and the outlying guard ring structure. The guard ring structure consist of ten concentric rings around the strips taking up 2 mm on all sides. The ten rings are all left floating with respect to the front or back voltages. This structure was added in an attempt to reduce the surface leakage current, particularly on the end strips.

Leakage current can occur in two primary ways on a silicon detector and can strongly affect the energy resolution [39]. The first is through the bulk of the wafer due to the impurities and defects of the silicon and through the thermal generation of electron-hole pairs within the depletion region. This effect is strongly dependent on temperature and can be reduced by active cooling. The HiRA silicon detectors run with leakage currents below 1 μA for DEs and on the order of 1 μA for the E’s at room temperature typically.

The second source of leakage current comes from surface currents. This can result in breakdown of the detector. With the thick E detectors a relatively large reverse-bias voltage must be applied in order to fully deplete the full 1.5 mm thick silicon detector. This can create a large potential difference between the edge of strips and the outer edge of the silicon wafer which is epoxied into the frame. The floating guard ring structure allows the voltage to drop from strip edges gradually from ring to ring reaching zero voltage by the outer most ring. This reduces the surface leakage current and prevents discharge between strips and grounds.

On the back (ohmic) side of the DE is a single aluminum electrode. . The E has 32 strips on the back (ohmic) side. These strips are perpendicular to the strips on the front side. The pitch on the back of the E detector is also 1.95 mm but it has an inter-strip gap of 40 μm as opposed to the 25 μm on the front. With strips on both sides this creates an effective pixel based on the strips hit on the front and the back. If the detector is mounted 35 cm from the target, which is the designed distance, the angular resolution is $\pm$ 0.15°. There is no guard ring structure on the back which is at ground while voltage is applied to the front during typical experimental setups. Figures 4.5 and 4.6 show the front and back of the E detector. Figures 4.7 and 4.8 show the front and back of the DE detector.

The bid requirements for the HiRA silicon detectors specified that all strips on a detector work with no strip resolution above 100 keV and an average strip resolution of 40 keV or less. Additionally, the voltage for full depletion on the E detector must be below 400 Volts. The depletion voltage for thin DE detectors is typically 7–10 V and does not create any problems. However when dealing with voltages above 500 V difficulties arise with the cable and the connector because such voltages may exceed the voltage rating for these components.

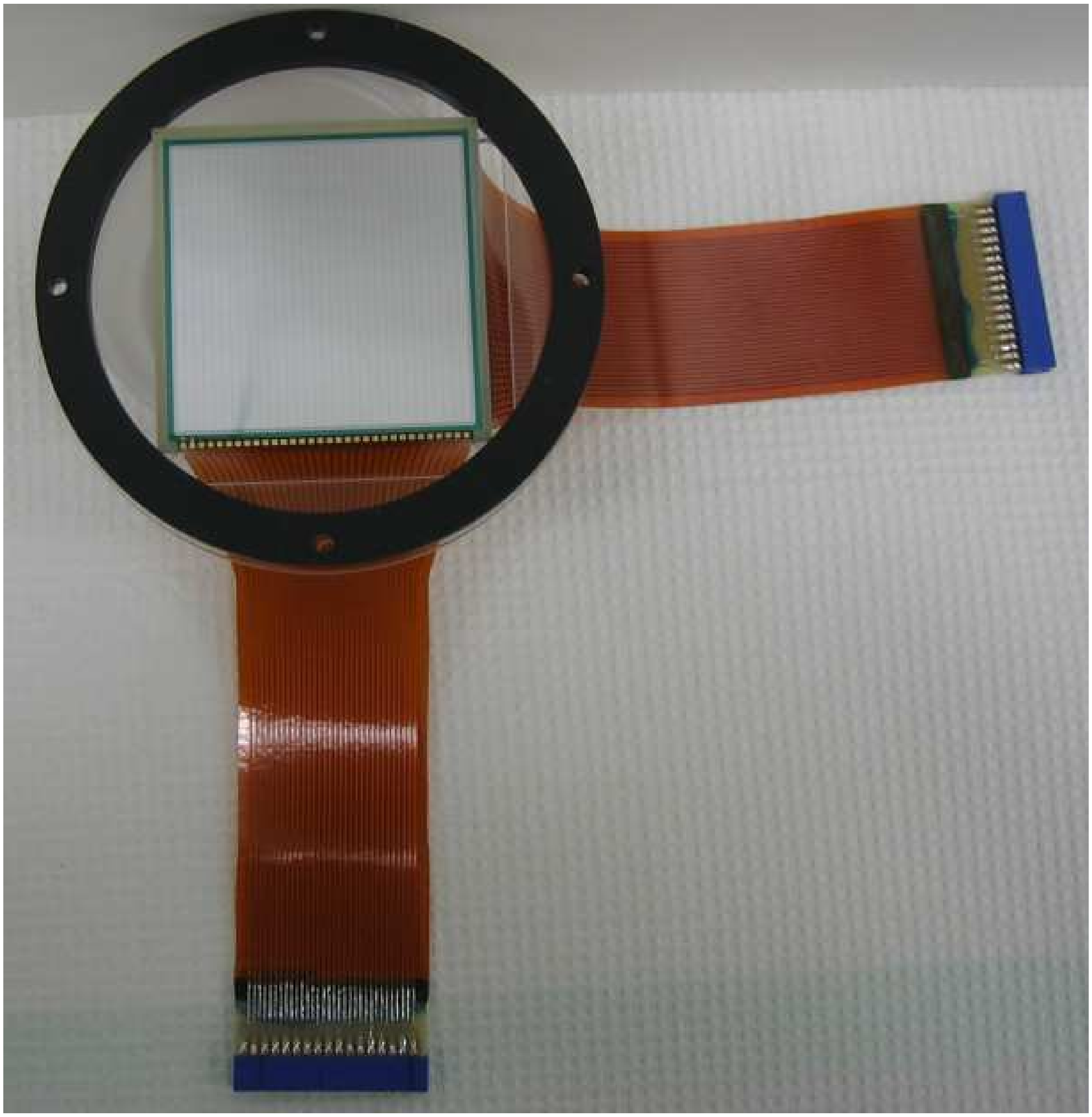

Figure 4.5: Picture of the front side of an E detector

Figure 4.6: Picture of the back side of an E detector

Figure 4.7: Picture of the front side of a DE detector

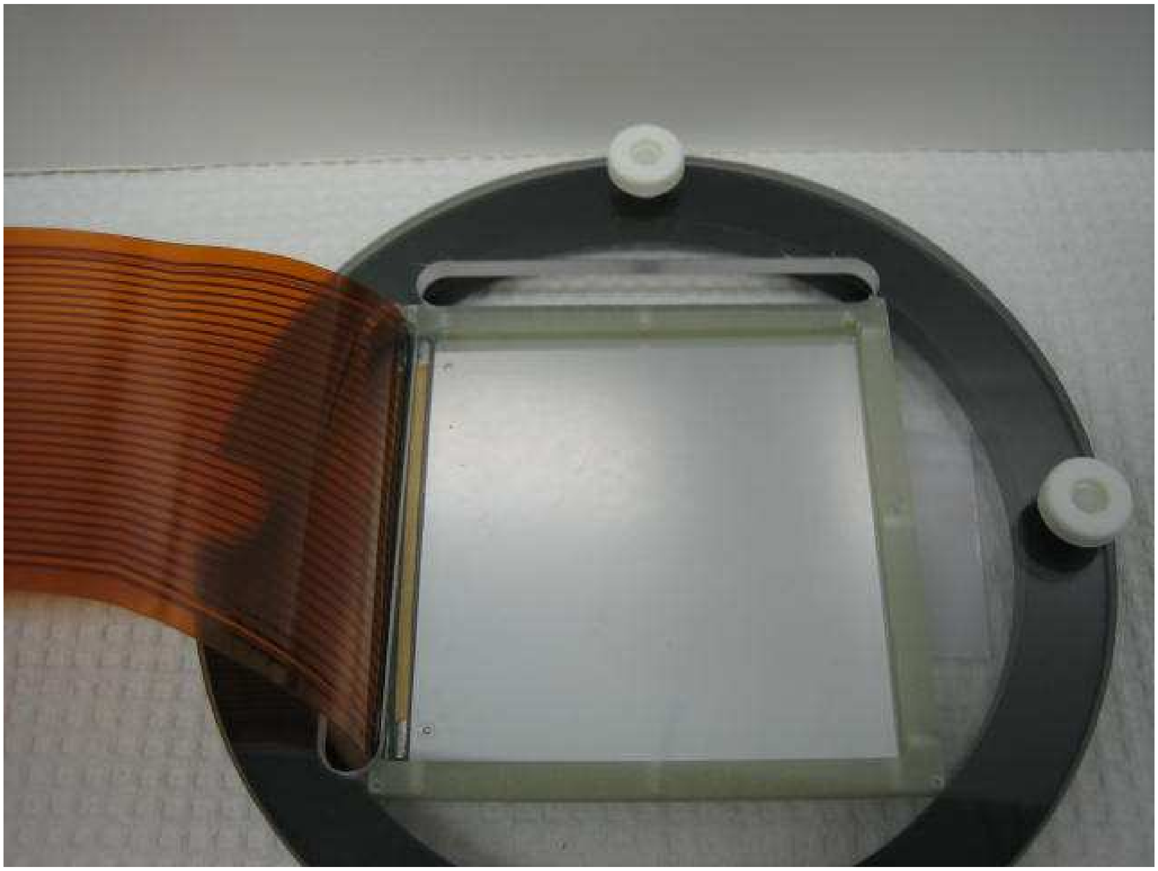

Figure 4.8: Picture of the back side of a DE detector

4.2.2 Testing of silicon detectors

Upon receiving detectors from Micron, the detectors were subjected to a series of test at Indiana University and then Michigan State University. The first test was a visual inspection of the silicon, wire bonds, and cable. After that, the detectors were tested in vacuum where the bias voltage and leakage current were measured. As this was done for all strip integrated together, no information is known about the leakage current per strip. The full depletion bias voltage was measured by irradiating the back side of the detectors with an ^{241}Am α source and measuring the amplitude and FWHM of the signal as a function of the negative bias voltage applied to the front of the detector. As the bias voltage increases the measured α particle energy rises and plateaus once the detector is fully depleted. These numbers are taken at room temperature and documented. The source is also used to measure the approximate resolution for each strip to make sure there are no bad strips.

At this point the detectors are ready to be mounted into the HiRA telescopes. The E detector is mounted first. It is then tested to verify full functionality and the energy resolution is measured. The procedure for measuring the resolution is as follows. The detector is placed inside a vacuum chamber with no foil between the detector surface and the α source. The ^{228}Th source has a thin 50 μg/cm^2 gold layer as a window. The alpha activity is 1.2 μC. The ^{228}Th source is a very nice calibration source as it contains eight different energy alpha particles with substantial branchings. Of these, five are separated by more than 100 keV making them very easy to fit and extract the peak location and full width half maximum (FWHM). The highest alpha energy is 8.7 MeV giving a larger signal than the ^{241}Am source which has the most intense peak at 5.5 MeV.

The source was placed approximately 20 cm's from the detector, illuminating all strips. The source-detector distance was less than the 35 cm from target to detector distance which means that the collimation of the guard ring was not effective. When particles strike the guard ring they generate signals with reduced energy on the edge strips.

The E detector is connected to a feed-through flange via two 34 pin cables with the 1st and 34th wires removed. They are removed to reduce the chance of shorting out the outer conductors on the ribbon cables which can be carrying a bias voltage up to 400 Volts. These traces are not needed to ground the detectors. The front 32 strips are biased with a negative voltage and the back strips are held at ground.

On the other side of the flange are small printed circuit boards that take the 32 signals and split them into two 34 pin connectors with grounds on every other pin. This circuit board has an input for the bias voltage with bias resistors and decoupling capacitors for each strip on it in order to protect the input to the pre-amplifiers from this high voltage. The two 34 pin connectors are then connected to PC boards that contain 16 individual pre-amplifiers. (These pre-amplifiers were originally built for LASSA and are discussed in Reference 37.) The pre-amplifiers are mounted to the top of the vacuum chamber to reduce noise and cable capacitance between the detector and pre-amplifiers, both of which adversely affect the energy resolution.

The output of the pre-amplifiers are then routed to CAMAC double wide modules that contain 16 channel shaping amplifiers and 16 channel leading edge discriminators made by Pico Systems [40]. The OR of the discriminators is used to setup a gate for the ADC and trigger the computer for data acquisition. The outputs of the shapers go into 32 channel CAEN VME ADCs. We pulse all the pre-amplifiers with a BNC PB-5 precision pulser in order to monitor drifts and account for electronic noise in the system. The data was then exported into a ROOT file for analysis.

Figure 4.9 is a histogram for an average EF strip. There are red triangles indicating the peak finding algorithm peak locations. The FWHM is then measured and a Gaussian fit is performed excluding the low energy tail which is non-Gaussian for α particles. There is also a pulser peak (not displayed) which is used to measure the electronic component of the overall resolution. Table 4.1 gives the FWHM resolution for each of the alpha peaks as they were measured and the intrinsic value (FWHM_{corr}),

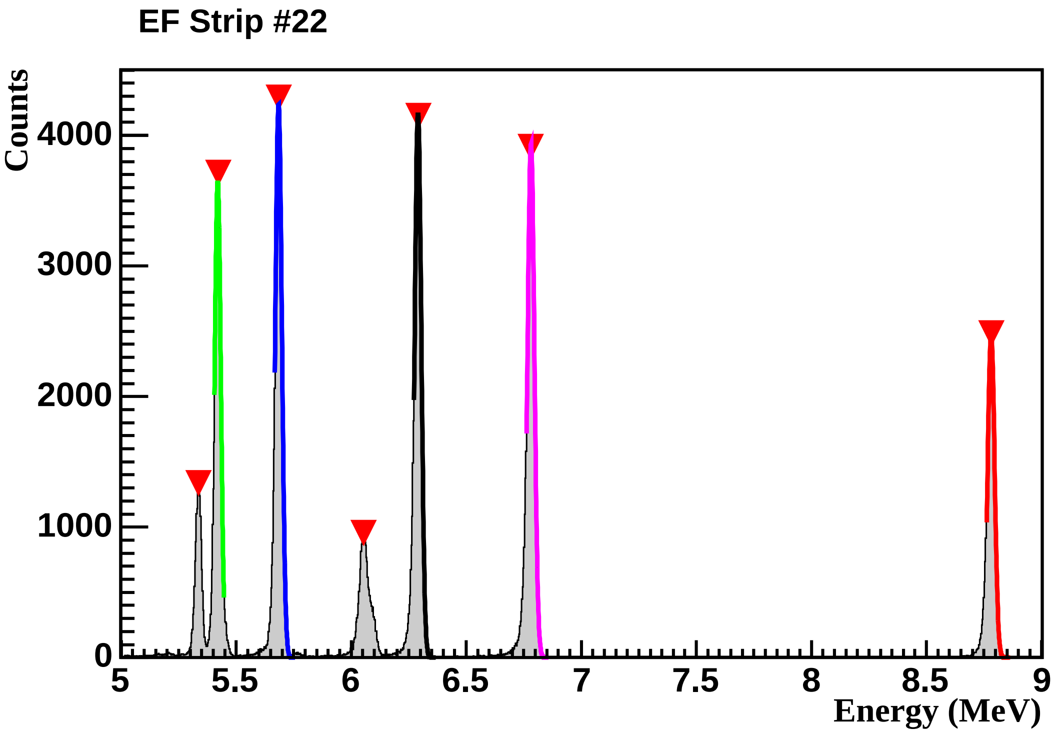

Figure 4.9: Energy spectrum of the ^{228}Th alpha source on a single strip on the front of an E detector. The red triangles are locations of peaks found by the peak finding function. The colored lines on 5 of the eight peaks are Gaussian fits.

Table 4.1: The energy resolution for each peak in 4.9 given raw and after subtracting electronic noise.The α energy is given in MeV and the FWHM are given in keV

Peak Color	Energy	FWHM	FWHM$_{corr}$
green	5.423	31.6	26.6
blue	5.685	33.4	28.7
black	6.288	33.2	28.4
pink	6.778	35.2	30.7
red	8.784	33.8	29.1

where the electronic noise contribution is subtracted in quadrature. The overall resolution is then taken to be the average resolution of the 5 strongest alpha peaks. For strip shown in Figure 4.9 the intrinsic energy resolution is 28.6 keV FWHM.

This procedure is performed for every strip of all E detectors. After that the DE detector can be mounted and tested in the same fashion. A histogram of energy resolution for all EF, EB, and DE strips is shown in Fig.4.10. These are the FWHM corrected for electronics noise. From this the absolute resolution of the entire HiRA

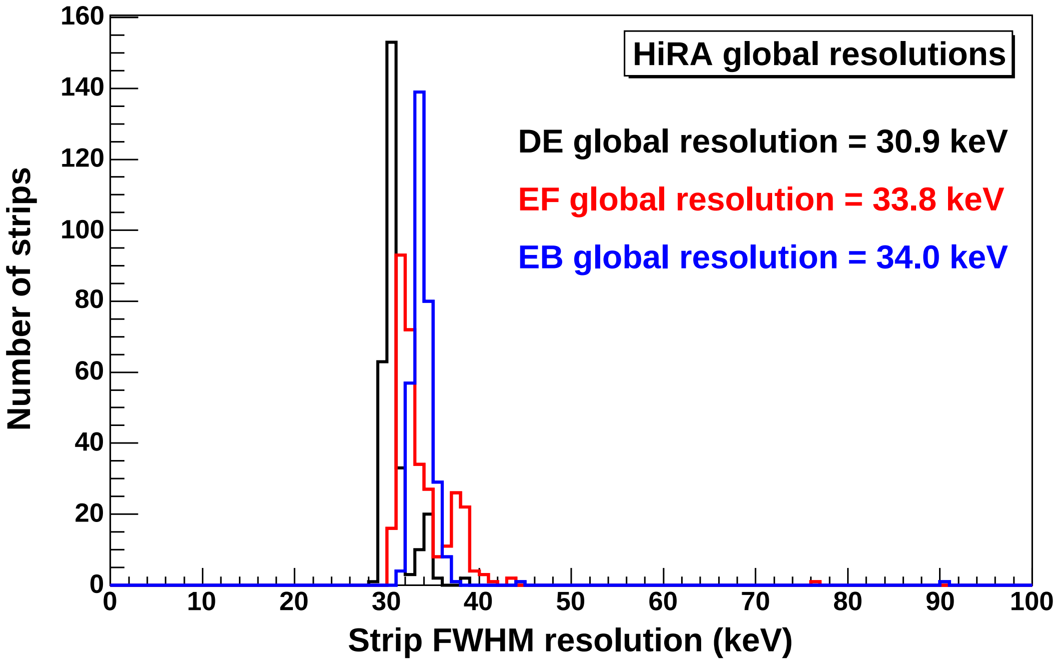

Figure 4.10: Histogram of energy resolution for all strips on all E an DE detectors

detector is determined.

4.3 CsI(Tl) crystals

Each HiRA telescope contains four CsI(Tl) crystals arranged in quadrants behind the 1.5 mm silicon detector. The crystals are 4 cm deep. The 4 cm thickness is sufficient to stop protons up to ∽115 MeV, alphas up to ∽465 MeV, and ^{12}C up to ∽2.7 GeV. Figure 4.11 show a side and front view of the CsI(Tl) crystals. The crystals are cut so the front of each one is 3.5×3.5 cm and the back is 3.9×3.9 cm. Two of the sides are cut straight back and the other two are cut at 5.3°. This allows all four to be tightly packed behind the silicon detectors and all particles that hit the silicon will stay in the crystal assuming the target is located 35 cm from the detector. Behind each crystal is a 1.3 cm thick light guide that covers the entire crystal. A photo-diode is attached to the back of the light guide. The photo-diode has a thickness of 0.3 mm and an active area of 18×18 mm^2.

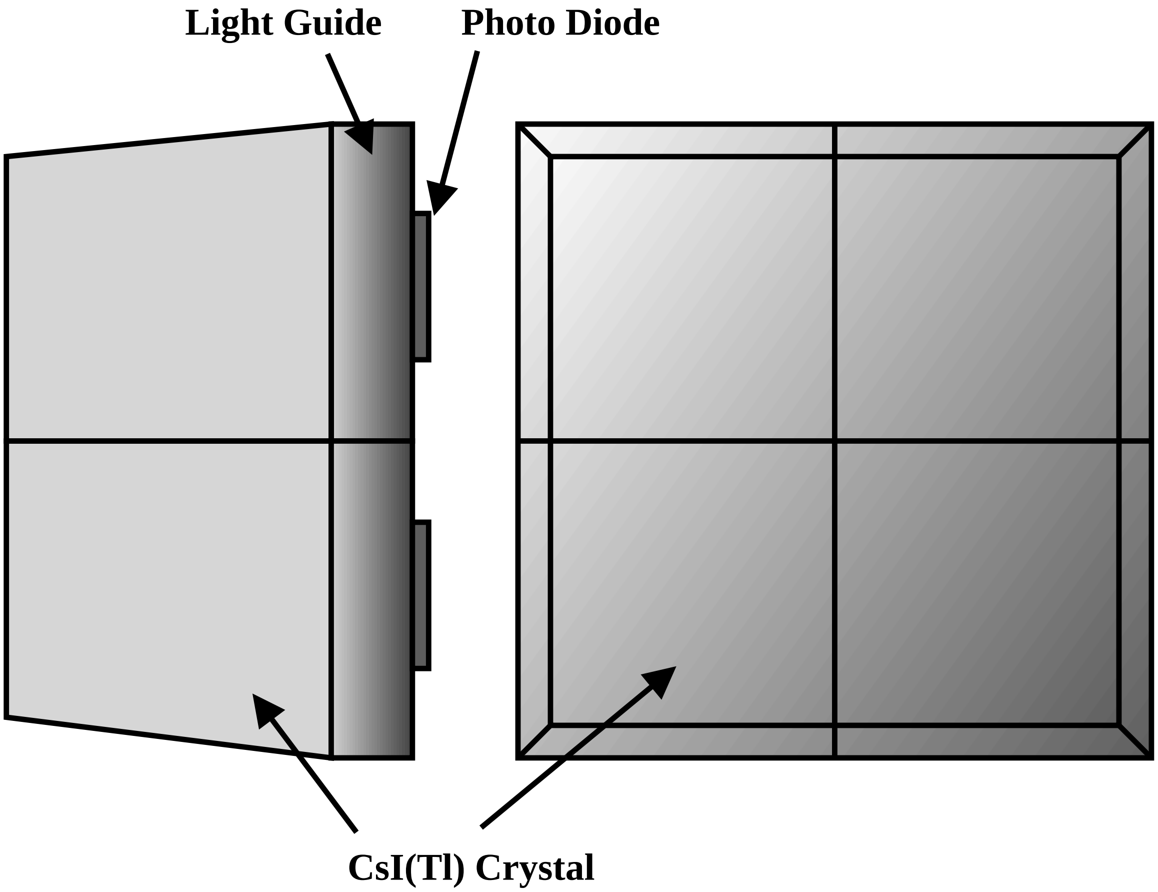

Figure 4.11: Side view and front view of a HiRA crystal, light guide and photo-diode assembly. The two inner sides of the crystal are cut perpendicular to the front and the rear faces of the crystal and the two outer sides of the crystal are cut at an angle of 5.3° from the perpendicular in order to back the active area of the silicon detectors when the telescope are placed at a distance of 35 cm.

Scintillators fabricated from thallium doped CsI (Cesium-Iodide) crystals have been extensively used for the detection of energetic charged particles [41–46]. This wide spread use stems from the facts that CsI(Tl) crystals can be readily machined, perform satisfactorily at room temperature, are not as hygroscopic as Na(Tl) crystals, and produce light with a spectrum that is well suited for readout via silicon photodiodes [41, 43, 45].

4.3.1 Crystal selection

While excellent resolution is achievable for highly uniform crystals, the resolutions of actual crystals are negatively impacted by local and global non-uniformities in the light output of the crystal [41, 44, 45]. Variations in the light output of the order of 0.5% have been observed between ionization trajectories through the crystal that are separated by as little as 3 mm [45]. These observations suggested that better resolution would be achieved if such local light output variations could be controlled [45]. Light output variations within scintillators have been explored in a variety of contexts because they are important for many scintillator applications. The corrections for light output variations vary from application to application, however. When scintillators are used for energetic γ-ray detection [47] or within large-scale sampling calorimeters [48], large volumes of these scintillators of the order of 102–104 cm^3 can be excited by a cascade of particles produced by the interaction of the incident particle with the scintillator. In such cases, the resolution is influenced by light output variations over distances of the order of centimeters, by statistics and by the degree to which the produced particles are confined to the scintillator volume. In contrast, charged particles with energies of 20–150 MeV/u activate comparatively small volumes along their trajectories in the crystal characterized by transverse dimensions of the order of millimeters; the major deposition occurs near the end of each trajectory where the stopping power attains maximum values characteristic of the Bragg peak. For such particles, the cascade of ionized electrons remains within the detector, the statistical accuracy can be very high; however, the light output uniformity over much smaller lateral dimensions of order of millimeters becomes critical. If a high degree of uniformity can be achieved or if the non-uniformity can be well characterized and the trajectory of each track defined by another detector, the energy resolution can be remarkable. To achieve such resolutions, it is important to control or characterize the light output uniformity and to understand how it depends on the charge or mass of the incident particle. Only then can the potential resolution of such devices by realized.

To investigate how the optimum resolution might be obtained, tests with eight sample crystals were undertaken along with surface scanning with an alpha source. Based on these test, the HiRA crystal order specifications were set, and testing procedures for all HiRA crystals were defined.

4.3.2 Crystal preparation

Light output in thallium doped CsI occurs through the transfer of a small fraction (<10 %) of the energy lost in the crystal by the incident ion to the excitation and subsequent radiative decay of thallium dopant ions. The thallium is incorporated into the CsI lattice in molar concentrations of the order of 0.1 % during crystal growth [49]. In general, while the light output is caused by the competition between the radiative deexcitations of the thallium dopant ions in the CsI(Tl) crystal and the non-radiative deexcitation of the crystal by other decay modes [50, 51], the ionization density of a specific ion dictates the amount of light produced. The competition between radiative and non-radiative deexcitations depends on the thallium doping concentration, the temperature and, possibly, other chemical or physical properties of the crystal.

The observations of local non-uniformities in light output by Reference 45 suggest that changes in the growth procedures for the CsI(Tl) crystals, an accurate compensation of the observed non-uniformities, or a combination of these techniques might lead to an improved energy resolution. The origins of the non-uniformities observed

Table 4.2: Crystals used in testing

crystal #	Crystal Type
0	Normal
1	Annealed
2	Normal
3	Annealed
4	Normal
5	Annealed
6	Super-doped
7	Super-doped
8	HiRA Crystal
9	HiRA Crystal

in Reference 45, however, are not understood. They may include local variations in the thallium doping concentrations and possibly, the presence of crystal defects or contaminants [50].

Ten crystals, numbered 0 through 9, were studied using two beam tests and alpha source scans across the crystal surface. Because the average light output of CsI(Tl) increases strongly with molar doping concentration below about 0.1 % and then remains roughly constant above this concentration, the sensitivity to local variations in doping concentration may be minimized by maintaining a high average thallium concentration. To address this possibility, two ($30 \times 30 \times 40$ mm^3) test crystals (crystals 6 & 7 in Table 4.2) were prepared with higher nominal thallium concentrations (about 0.5–0.6 % molar concentration or 1000–1200 ppm Tl as compared to the typical doping concentration of 0.15 %–0.35 % molar concentration or 300–700 ppm Tl). We label these crystals here as "superdoped", even though the doping level of these crystals may not lie far outside of the typical range of doping levels available commercially. Alternatively, an attempt was made to modify the local relative concentrations of thallium dopant ions and defect sites by thermally annealing the crystals in vacuum, a process that has modified the light outputs of some scintillators [52,53]. To address this possibility, six ($30 \times 30 \times 30$ mm^3) test crystals (crystals 0–5) were prepared. Three of these were annealed (crystals 1, 3, & 5) and three were not annealed (crystals 0, 2,

& 4). No specifications or pre-selection criteria regarding the overall non-uniformity were imposed on the test crystals. Consequently, some of the test crystals displayed larger variations in the light output across the face of the crystal than would be desirable for many applications. We believe this did not negatively impact tests for local non-uniformities that depend non-linearly on the position of the ionization trajectory through the crystal. We did not attempt to differentiate between the non-uniformities along the growth axis and the non-uniformities along the other two Cartesian coordinates of each crystal because the orientation of the growth axis with respect to the final crystal surfaces was not recorded and retained.

An acceptance criterion that the light output varies by less than ±0.5 % across the face of the detector was placed upon the HiRA crystals. The HiRA crystals, with square 3.5×3.5 cm^2 front and 3.9×3.9 cm^2 rear surfaces and a length of 4 cm, were somewhat larger than the test crystals. Figure 4.11 shows side and front views (for a HiRA detector) of the scintillator and photodiode package. Both test and HiRA crystals were prepared by fine polishing the front and rear surfaces, and sanding the four sides with 400 grit paper in the direction from the front surface to the light-guide. Light-guides of 1.3 cm thickness were glued to the HiRA crystals with BC 600 optical cement and to the six smaller test crystals with GE Bayer Silicones RTV615 silicon rubber glue. The larger ($30 \times 30 \times 40$ mm^3) test crystals were used without light guides. Silicon photodiodes with a thickness of 0.3 mm and an active area of 18×18 mm^2 were glued to the rear of the light guide with GE Bayer Silicones RTV615 silicon rubber glue. The sides of the test crystals were wrapped using one layer of cellulose nitrate membrane filter paper and then one layer of Teflon tape. The sides of the HiRA crystals were wrapped with two layers of cellulose nitrate filter paper and one layer of aluminized Mylar. The front faces of all crystals were covered with an aluminized Mylar foil. The light guides were painted with BC-620 reflective paint.

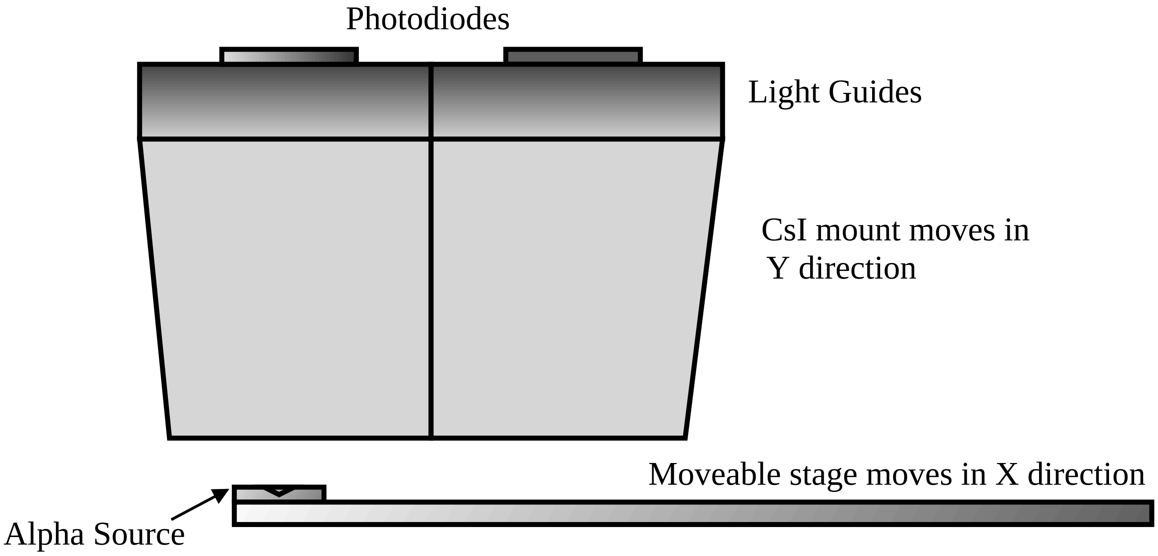

Figure 4.12: Test configuration for the HiRA CsI crystals inside the scanning chamber with a collimated ^{241}Am α source

4.3.3 Alpha scanning

In order to test the position dependence of the response of the CsI crystals to 5.486 MeV alpha particles from a ^{241}Am source, a test apparatus was built, which allows one to move a collimated alpha source and a CsI(Tl) crystal in perpendicular directions inside a vacuum chamber. The configuration was automated such that an energy spectrum was obtained for points separated by a spacing of 3 mm on a 10 by 10 Cartesian grid on the front surface of the test crystals. This grid was centered on the crystals and avoided the edges. At each grid point, the collimated source irradiated a 3 mm diameter area of the crystal surface for 5 minutes before moving to the next grid point. The source test configuration is diagrammed in Figure 4.12. Using the information from the linear drives used to move the crystals and the source, discrete grids in the xy coordinate plane are mapped onto the scintillation crystals. At the coordinate $x = i$, $y = j$, the non-uniformity S_{ij} of light output for scintillation crystals is expressed as:

$$S_{ij} = \frac{(L_{ij} - \langle L \rangle)}{\langle L \rangle} \tag{4.1}$$

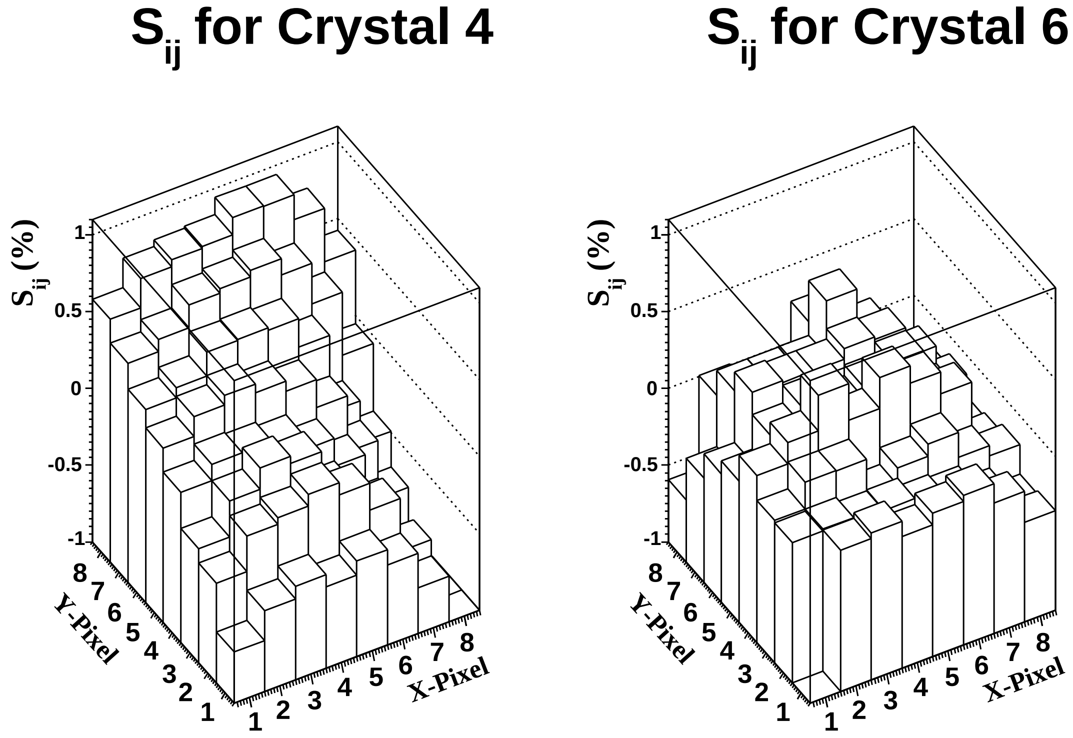

Figure 4.13: The variation of the light output over the face of the detector is show here as a percent deviation from the mean (S_{ij} as defined in Equation. 4.1). Here neighboring pixels are separated from each other by 3 mm in both x and y directions. This result is obtained using 5.5 MeV alphas from a ^{241}Amsource.

where L_{ij} is the centroid of the energy spectrum at position i, j and $\langle L \rangle$ is the average over the entire crystal. In the case of a crystal with a perfectly uniform response, the variance of S_{ij} would be dictated only by the statistical uncertainty of the centroids of the peaks. In practice, the variance of S_{ij} can be dominated by the light output non-uniformity in each crystal.

The centroid of the light output peak was calculated for each of the Cartesian grid points. Figure 4.13 shows the S_{ij} calculated from Equation 4.1 for two test crystals. (In order to minimize sensitivity to edge effects, the outside points are excluded (pixels 0,9) from this figure and for all subsequent plots of the alpha source and the various beam scans.) Some crystals, such as crystal 4 show large global changes in the light output while others such as crystal 6 have relatively small non-uniformities. The overall non-uniformities in light output for the final HiRA crystals were specified

Table 4.3: S_{rms} from alpha scans on all 8 test crystals

crystal #	S_{rms} (%)
0	0.5915
1	0.3396
2	0.6328
3	0.6349
4	0.5395
5	0.4679
6	0.2712
7	0.2204

to be less then ±0.5 %; plots of the overall light output uniformities of HiRA crystals were therefore more similar to crystal 6 then crystal 4. Table 4.3 gives the rms value of S_{ij} from alpha scanning of the 8 test crystals.

Clearly there are global trends that can be corrected for or minimized by the required specifications for HiRA, however there are small scale fluctuations on the order of mm's that cannot be easily corrected for. In order to investigate these small scale fluctuations two methods are used to correct for non-uniformities in the light output. The first characterizes the non-uniformities using a two-dimensional linear fit to the non-uniformity. The resulting non-linearity parameter F_{ij} is calculated as:

$$F_{ij} = A + Bi + Cj \tag{4.2}$$

where the parameters A, B, and C are determined from fitting Equation (4.2) to the non-uniformity across the face of the crystal.

Using Equations 4.1, 4.2, the residual non-uniformity, which could be due to statistical variations in the light output, is defined by subtracting the fitting function from the measured non-uniformity:

$$D_{ij} = S_{ij} - F_{ij} \tag{4.3}$$

In cases where higher-order corrections are desired due to non-linear non-uniformities

Table 4.4: Linear fit parameters for the test crystals determined from α source scanning, α beam measurements, and deuteron beam measurements.

crystal #	Type	Source	A (%)	B (%/mm)	C (%/mm)
0	Normal	α scan	1.496	-0.128	-0.146
		α beam	-	-	-
		^{2}H beam	-	-	-
1	Annealed	α scan	0.832	-0.049	0.0621
		α beam	-0.028	-0.024	-0.010
		^{2}H beam	0.158	-0.048	0.029
2	Normal	α scan	-0.736	-0.090	0.275
		α beam	0.017	-0.055	0.058
		^{2}H beam	0.471	-0.088	0.048
3	Annealed	α scan	0.580	-0.258	0.012
		α beam	0.220	-0.132	0.067
		^{2}H beam	0.153	-0.110	0.071
4	Normal	α scan	-0.516	-0.086	0.218
		α beam	-0.028	-0.051	0.043
		^{2}H beam	-0.097	-0.048	0.082
5	Annealed	α scan	1.342	-0.099	-0.149
		α beam	1.194	-0.113	-0.107
		^{2}H beam	0.892	-0.063	-0.061
6	Super-doped	α scan	-0.136	-0.023	0.015
		α beam	-0.124	0.013	-0.003
		^{2}H beam	-0.145	-0.001	0.034
7	Super-doped	α scan	-0.229	0.000	0.040
		α beam	-0.011	0.018	-0.037
		^{2}H beam	0.333	-0.027	0.019

or where the statistics is much lower, smoothed non-uniformities are calculated using a 3×3 flat smoothing function:

$$SM_{ij} = \frac{1}{N_{points}} \sum_{k=i-1}^{k=i+1} \sum_{l=j-1}^{l=j+1} S_{kl} \tag{4.4}$$

where the summation includes only the values within these limits for k and l at which values of S_{ij} were measured. Consequently, N_{points} = 9, 6, and 4 for points (i,j) in the center, edge, or corner of the detector, respectively. This increases, by a multiplicative factor of N_{points}, the effective number of counts in the grid map and thereby reduces the statistical fluctuations. Table 4.4 give the fit parameters A, B,

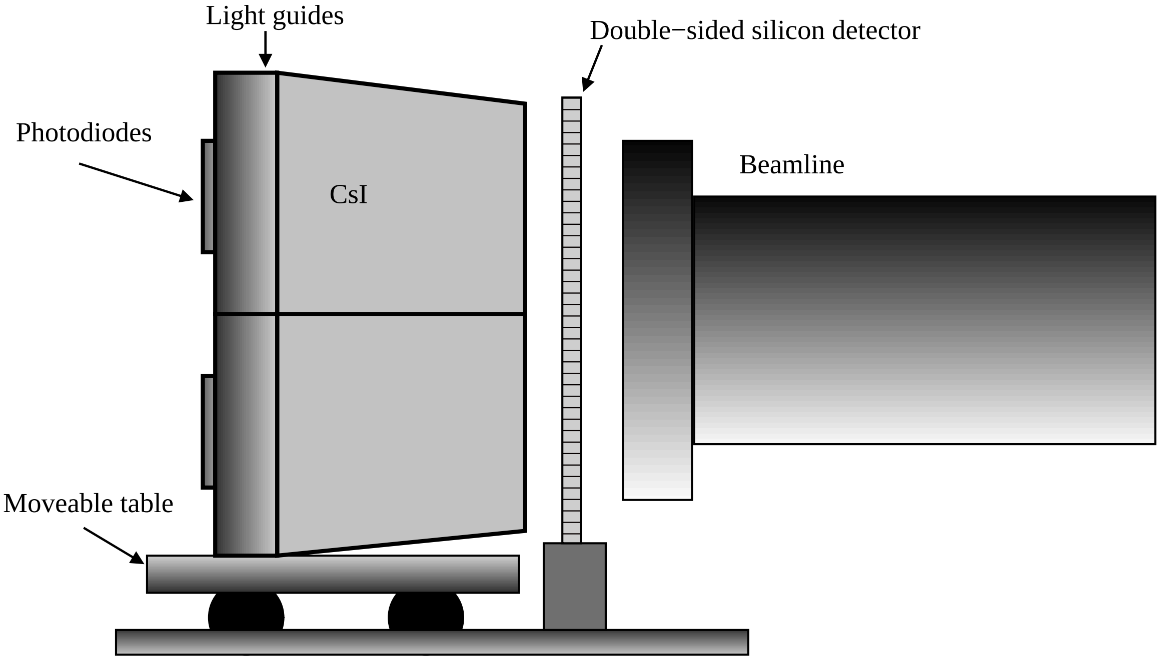

Figure 4.14: Test configuration for the HiRA CsI crystals. In the case of the test at the Texas A&M facility, the silicon detector was stationary with respect to the beam line and the crystals were wrapped separately. In the case of the tests performed at the NSCL, the silicon detector moved with the crystals and the crystals were wrapped as shown.

and C for the source scan as well as the direct beam measurements described in section 4.3.4. For reference, a value of 0.1 (0.05) for B or C implies an increase of 1% (0.5%) in the light output across the 3 cm wide crystal.

4.3.4 Direct primary beam measurements

While alpha source measurements are practical for pre-scanning large numbers of crystals prior to fabrications into an experimental device, such a test probes only the first 30 microns of the crystal or less. As large doping gradients tend to persist throughout a crystal [41, 44, 45], such tests can serve to reject crystals with large gradients of order 1% or more, but many be insificient to provide information about the persistence of small non-uniformities of the order 0.1%.

In order to measure the variation of such small non-uniformities throughout the test crystals, the eight test crystals were scanned with primary beams of 220 MeV alpha particles and 110 MeV deuteron's from the K500 cyclotron at the Texas A&M cyclotron facility. The experimental configuration was placed in air at the end of the Single-Event Effect (SEE) beam-line. A 500 μm thick double-sided silicon strip detector was fixed in position near the exit foil of the beam pipe in front of the crystals. The beam illuminated a circular spot of 2.5 cm diameter on the silicon detector; the 3 mm wide horizontal and vertical strips of this detector divided the beam spot into 100 pixels, each having a size of 3×3 mm^2. The 8 CsI(Tl) crystals were placed behind the silicon detector on a movable computer controlled platform. Thus the light output uniformity was measured over a Cartesian grid for both the 220 MeV alpha and 110 MeV deuteron beams. Figure 4.14 shows a schematic diagram for the beam test configuration.

A relative comparison of the average light output of the eight test crystals from this beam test is shown in Fig. 4.15 (here the data was arbitrarily normalized to that of crystal 6). Somewhat higher than average light outputs were observed for the "super-doped" crystals 6 & 7; however, the range of light outputs is large. On the average, the light output of the annealed and non-annealed crystals was comparable. Because light output prior to annealing was not measured, this comparison does not probe whether annealing enhances the light output of a specific crystal.

With beam energies of 220 MeV for the alpha beam, and 110 MeV for the deuteron beam, the penetration depth for the alpha beam is about 11 mm, and the penetration depth for the deuteron beam is about 22 mm, which are both much larger than the penetration depth $\sim$ 30 μm for the ^{241}Am source. The 3×3 mm^2 spots defined by the silicon detector defined the trajectories of the alphas and deuterons through the crystals. The transverse straggling of 0.5 mm for the alpha beam and 1.3 mm for the deuteron beam did no exceed the pixel spatial resolution. Values for S_{ij} were calculated at each grid point for each detector for both alpha and deuteron runs. Figure 4.16 shows S_{ij} obtained with the alpha beam and deuteron beam for crystals 4 and 6. Again for the beam scans, one observes a roughly linear dependence of S_{ij}

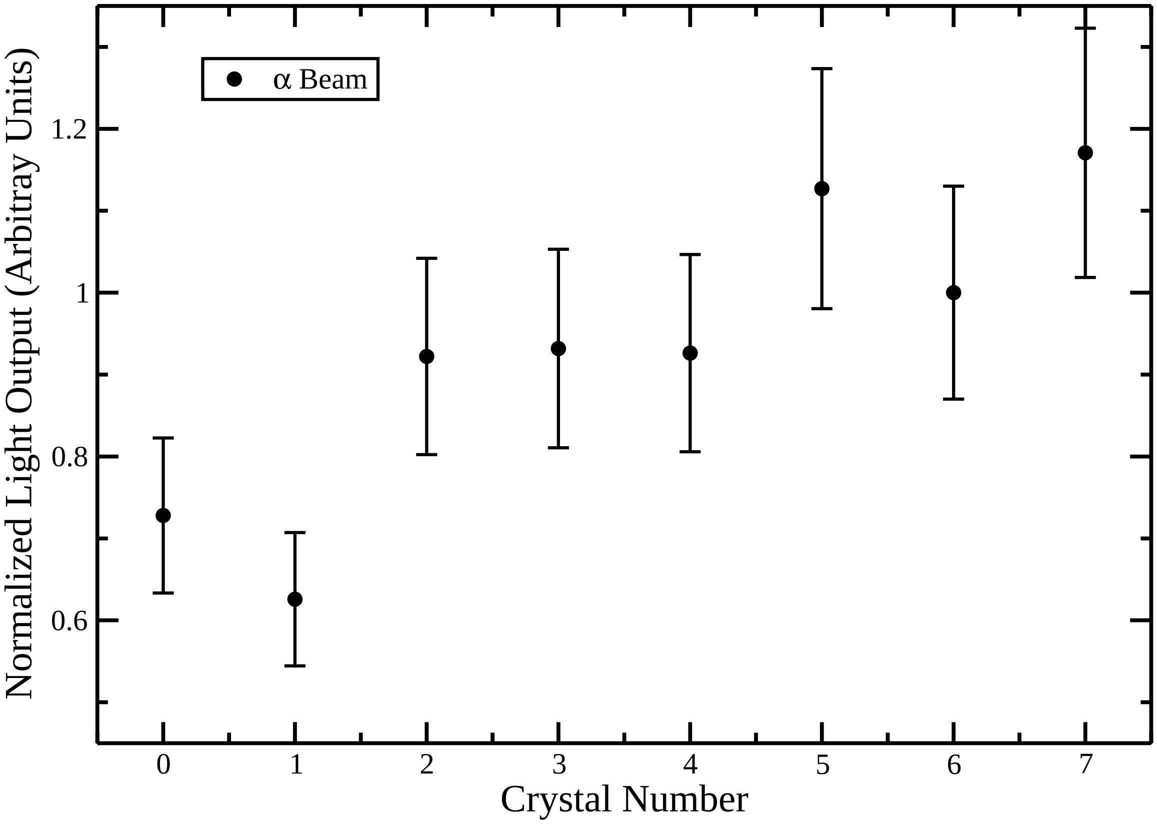

Figure 4.15: Relative comparisons of the light outputs from the eight test crystals. The light output of the HiRA crystals were selected to be within 15% of the light output of test crystal 6. These results were obtained with the 220 MeV α beam; the same results are obtained for the deuteron beam. The error bars are estimated from the reproducibility in the relative light output observed after recoupling the test crystals to the photo-diode and its associated electronics.

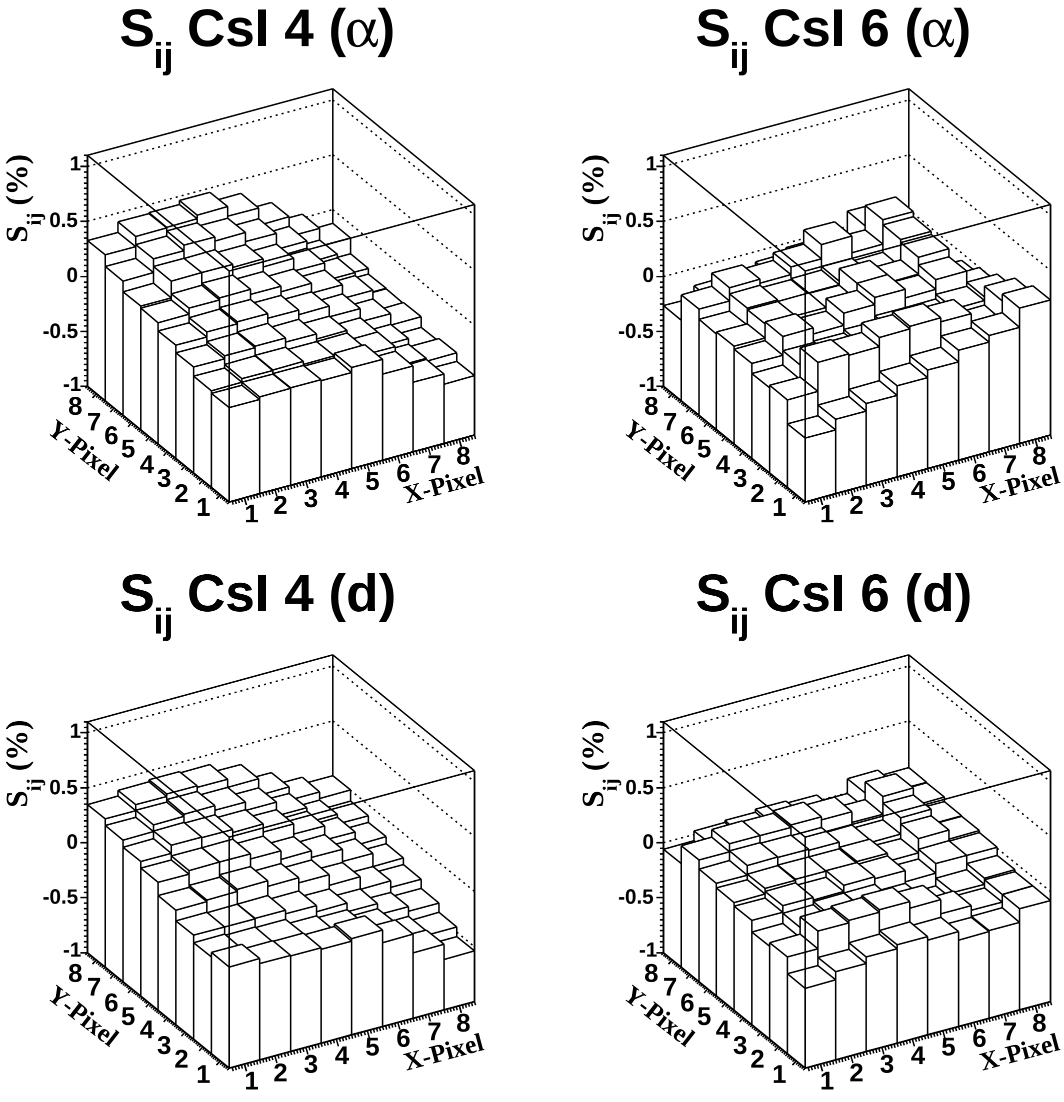

Figure 4.16: S_{ij} obtained for the alpha and deuteron beams for CsI 4 and 6.

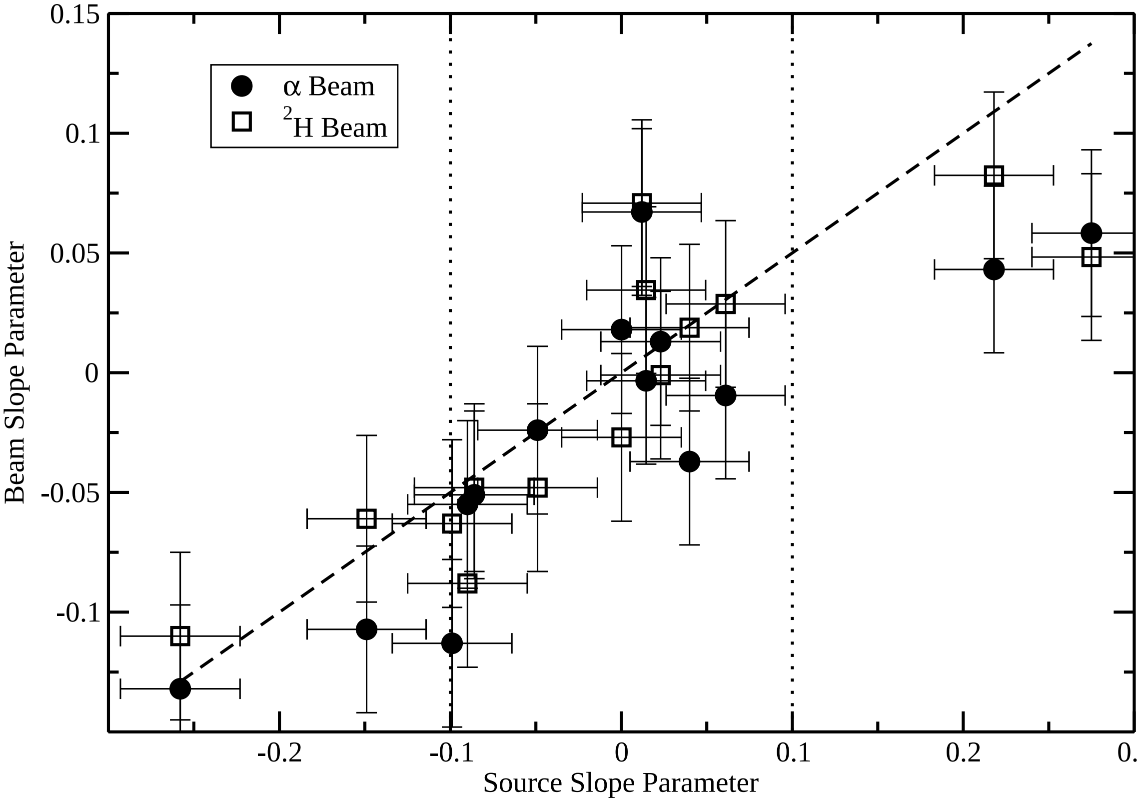

Figure 4.17: Correlation between the slope parameters obtained via the alpha source test and those obtained via the 220 MeV alpha beam test (solid points) and the 110 MeV deuteron beam test (open points). The diagonal dashed line represents a trend-line with a slope of 0.5. The region between the two vertical dotted lines represents the acceptance criteria for HiRA crystals.

on the displacement across the face of crystal 4, while no strong linear dependence of the form given by Equation 4.2. Values for the fit parameters A, B, and C are given in Table 4.4.

Figure 4.17 shows the correlation between the parameters B and C obtained from the alpha source fits and those obtained from the 220 MeV alpha beam (solid points) or the 110 MeV deuteron beam (open points). The slope of the dashed trend-line shown in the figure has a value of 0.5. Thus the alpha source scan is twice as sensitive to the crystal non-uniformity than are the alpha and deuteron beams scans; the alpha source sensitivity is actually more comparable to that for beam particles of much higher Z such as lithium, see 4.3.6 for a discussion of this. Some of the difference between the linear fit parameters of the alpha scan and the beam scans may be due to non-zero gradients along the beam direction; the ^{241}Am alpha-scan particles, the 220 MeV alpha beam particles, and the 110 MeV ^{2}H beam particles have very different penetration depths. However, it will be shown that the light output non-uniformity is larger for particles with larger average stopping powers in the crystal; these average stopping powers are greater for the alpha source than for the alpha beam and both alpha source and beam have a larger average stopping powers than that of the deuteron beam. This is probably the main reason why the non-uniformities observed for the alpha source exceed those for the alpha and deuteron beams.

The correlation between the various scans shows why one can use the alpha source measurements to pre-select the crystals and reject crystals with large non-uniformities. The vertical lines in Figure 4.17 indicate the acceptance criterion alpha source parameter < 0.1; crystals to the left of the leftmost line and to the right of the rightmost line, which displayed large non-uniformities in both the beam and alpha source tests, are rejected under this criterion.

Residual non-uniformities calculated with Equation 4.3 are shown in Figure 4.18 for the same crystals 4 and 6. The residual non-uniformities are zero on the average, but there are regions in which all the neighboring pixels have positive residuals and other regions where all the neighboring pixels have negative residuals. This suggests that a much higher order fit or a pixel-by-pixel correction to the light output uniformity might be a better approach. This is particularly true for crystal 6, which displays some ridges of higher light output for both alphas and deuterons.

By combining the energy deposited in the silicon with the energy deposited in the CsI(Tl) crystal one obtains measurements of the total beam energy of the incident deuteron and alpha beams. These are shown in Fig. 4.19 for alpha particles (top panels) and deuteron's (bottom panels). The left panels are for the less uniform CsI(Tl) crystal 4 and the right panels are for the more uniform CsI(Tl) crystal 6. The dotted lines are the overall crystal energy spectra without correction for the light output non-uniformity. The dashed lines are the crystal spectra corrected with the

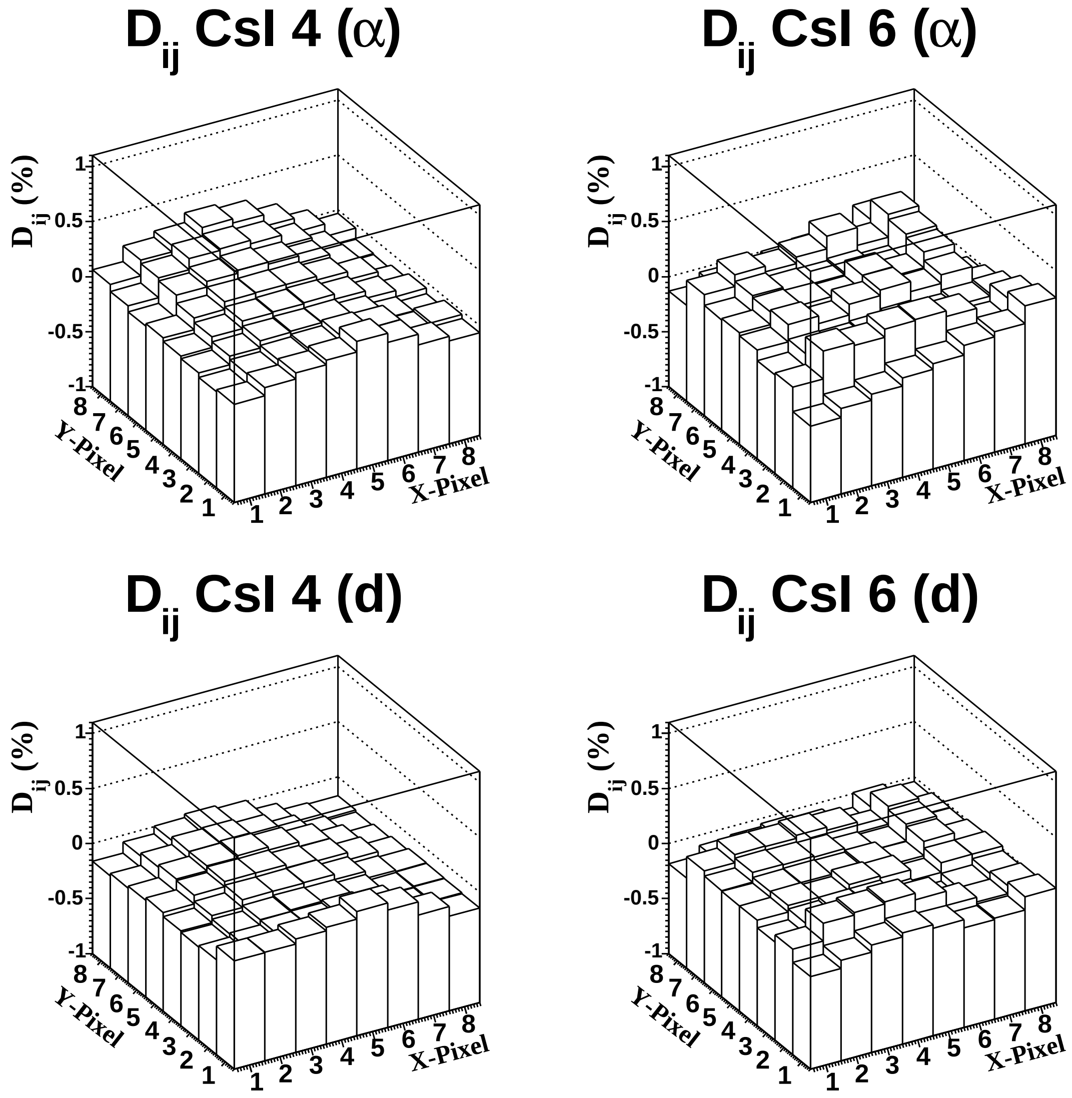

Figure 4.18: D_{ij} for crystals 4 & 6 from alpha and deuteron beams

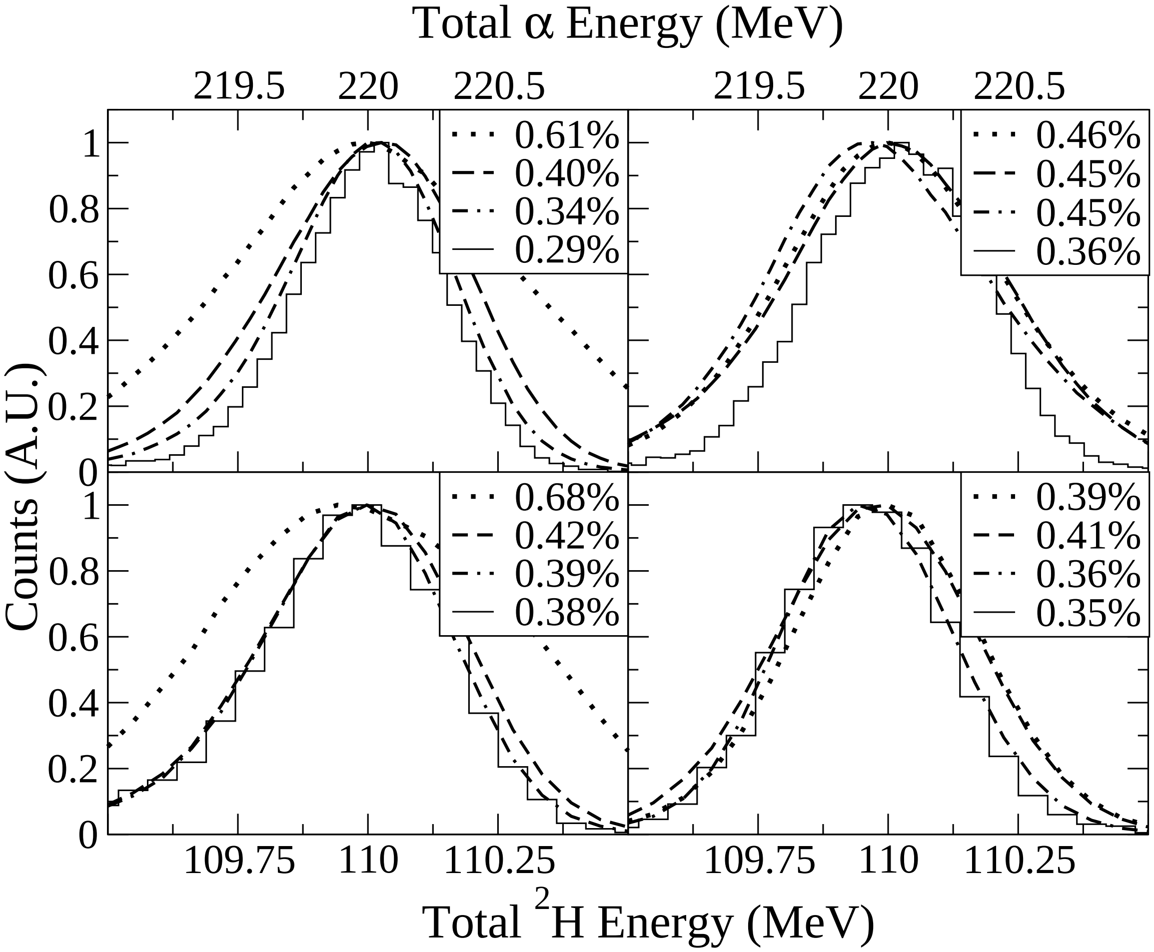

Figure 4.19: Left panels: crystal 4 with large non-uniformity. Right panels: crystal 6 with small non-uniformity. Bottom panels: Results for 110 MeV deuterons. Top panels: Results for 220 MeV alpha particles. In all panels, the dotted lines are the uncorrected energy spectra. The dashed lines are the spectra corrected with the linear correction for the light output non-uniformities. The solid lines are spectra for particles that enter into one randomly chosen pixel in the detectors. The dot-dash line is the crystal spectra corrected using the smoothing algorithm.

linear fit for the light output non-uniformities. The solid lines are spectra for particles that enter into one randomly chosen pixel in the detectors. This latter spectrum has the same resolution (e.g. crystal 6: $\sigma \approx 0.15$ % or 0.16 MeV for deuterons, 0.15 % or 0.33 MeV for alphas) as one would achieve by a pixel-by-pixel correction for the light output non-uniformity across the crystal. The difference between the solid histograms and dashed lines reflect the degree to which the non-uniformities can be modeled by a linear dependence. Crystal 4 is more linear in its non-uniformity then crystal 6; the corrected non-uniformity of crystal 4 shown in figure 4.18 is smaller than the corresponding corrected non-uniformity of crystal 6. Thus, the corrected resolution for crystal 4, shown by the dashed line in the left panel of figure 4.19, is smaller that that of crystal 6, shown in the right pannel. The dot-dash line comes from a correction done using the smoothing function given by Equation 4.4 It is concluded that the non-uniformity varies linearly across the face of crystal 4, while the variation is more complex across crystal 6.

The energy resolution of the beam makes a negligible contribution to the resolution of a single pixel given by the solid histograms. The electronic noise (determined by a precision pulser) contributes $\sigma_{noise} \approx$0.1 MeV to the single pixel resolution. This corresponds to rms contributions of 0.1 % for deuterons and 0.05 % for alphas. Subracting this electronics noise contribution, one obtains rms intrinsic (noise corrected) resolutions of about 0.11 % ($\approx$0.1 MeV) for deuterons and 0.14 % ($\approx$0.3 MeV) for alphas.

4.3.5 HiRA crystals

There was no obvious superior manufacturing method for suppressing the local variations of the light output that occur over distance scales of the order of a few mm, and local variations are always present. Based on the results with these 8 test crystals the order was placed for the 80+ crystals needed for the full HiRA array. When the crystals were received each one was visually inspected for cracks or faults and then measured. The physical dimensions of each crystal are important for a few reasons. First, in order to mount properly with 3 other crystals in the support structure they must be very close in size. Secondly, particles that punch through the crystal can be used to calibrate the energy, but only if the depth is known precisely. The surfaces were also studied as the sides must be sanded and the front and back fine polished. Enough of ∼100 crystals received were of incorrect thickness, or with polishing blemishes, that it became necessary to work on them. A lapping machine apparatus was built to sand the back side of all crystals to the same thickness and also to polish surfaces that were sanded down or that needed additional polishing. The light guides and photo-diodes were attached in the same fashion described previously. Surface scans using the same ^{241}Am α source occurred on all test crystals. Crystals that did not meet our specifications were sent back and replaced.

4.3.6 HiRA beam tests

A test using a similar configuration to that of the Texas A&M experiment, and described in Figure 4.14, was used to test 4 of the new HiRA CsI(Tl) crystals. This experiment was performed using secondary projectile fragmentation beams from the CCF at Michigan State University. Secondary beams of 53 MeV protons, 48 MeV ^{3}He, 40 MeV deuterons, 105 MeV ^{3}He, 158 MeV ^{6}Li, and 243 MeV ^{7}Be were produced by fragmenting a primary ^{40}Ar beam at 140 MeV/A on a Be target and selected by magnetic rigidity with the A1900 separator. For each beam, a 1% separator momentum acceptance was used corresponding to an energy resolution of 2 %. The experimental configuration was placed in air in the N3 vault. A 1.5 mm thick double-sided HiRA silicon strip detector was fixed in position in front of the four CsI(Tl) detectors to form an energy loss telescope. This telescope was mounted on a movable platform in front of the exit foil of the beam pipe. Computer controlled stepping motors were used to move each crystal to illuminate uniformly most of its surface area with the beam. In this fashion, the light output for each HiRA crystal was measured over a 256 pixel cartesian grid with a pixel size of 2×2 mm^2 for all fragmentation beams. This 2 % beam energy is not as good as the primary beam resolution from Texas A&M, however this test provided information from many more nuclei and multiple energies for some, as well as a finer grid size based on the 1.95 mm pitch of the HiRA silicon detector in front of the CsI(Tl) crystals. The statistics for many of these beams was quite low.

Figures 4.20 and 4.21 show S_{ij} obtained for two HiRA crystals (8 & 9) for proton, deuteron, ^{3}He, ^{6}Li, and ^{7}Be fragmentation beams. Unlike the case for the test crystals with larger thallium doping gradients, S_{ij} does not display a strong linear dependence across the face of each detector. In fact, the observed non-uniformities are rather complex and would require rather high order polynomials or Fourier components to achieve a satisfactory fit. On the other hand, the trends for the different particle types are similar in form. The magnitudes of the non-uniformities are larger for more highly charged particles such as ^{7}Be or ^{6}Li than for protons or deuterons. After applying the smoothing function, given in Equation 4.4, to the HiRA crystals a similarity between the smoothed non-uniformities for particles with different charge Z, mass A, or energy E was observed. This similarity was probed by determining a scaling factor $\alpha(Z, A, E)$:

$$SM_{ij}(Z, A, E) = \alpha(Z, A, E) \cdot SM_{ij}(Z_0, A_0, E_0) \tag{4.5}$$

where $Z_0 = 3$, $A_0 = 6$, and $E_0 = 158$ MeV was taken for all comparisons between HiRA detectors tested at the coupled cyclotron facility (CCF). The value of α is then determined by fitting the non-uniformity obtained for particles with Z, A, and E using Equation 4.5 and the reference scan for particles with Z_0, A_0, and E_0.

Some insights into the charge dependence of the non-uniformities can be obtained if one considers an approximate formula for the light output given by Birks [50, 51]

$$\frac{dL}{dx} = a \left|\frac{dE}{dx}\right| \frac{1}{1 + b\left|\frac{dE}{dx}\right|} \tag{4.6}$$

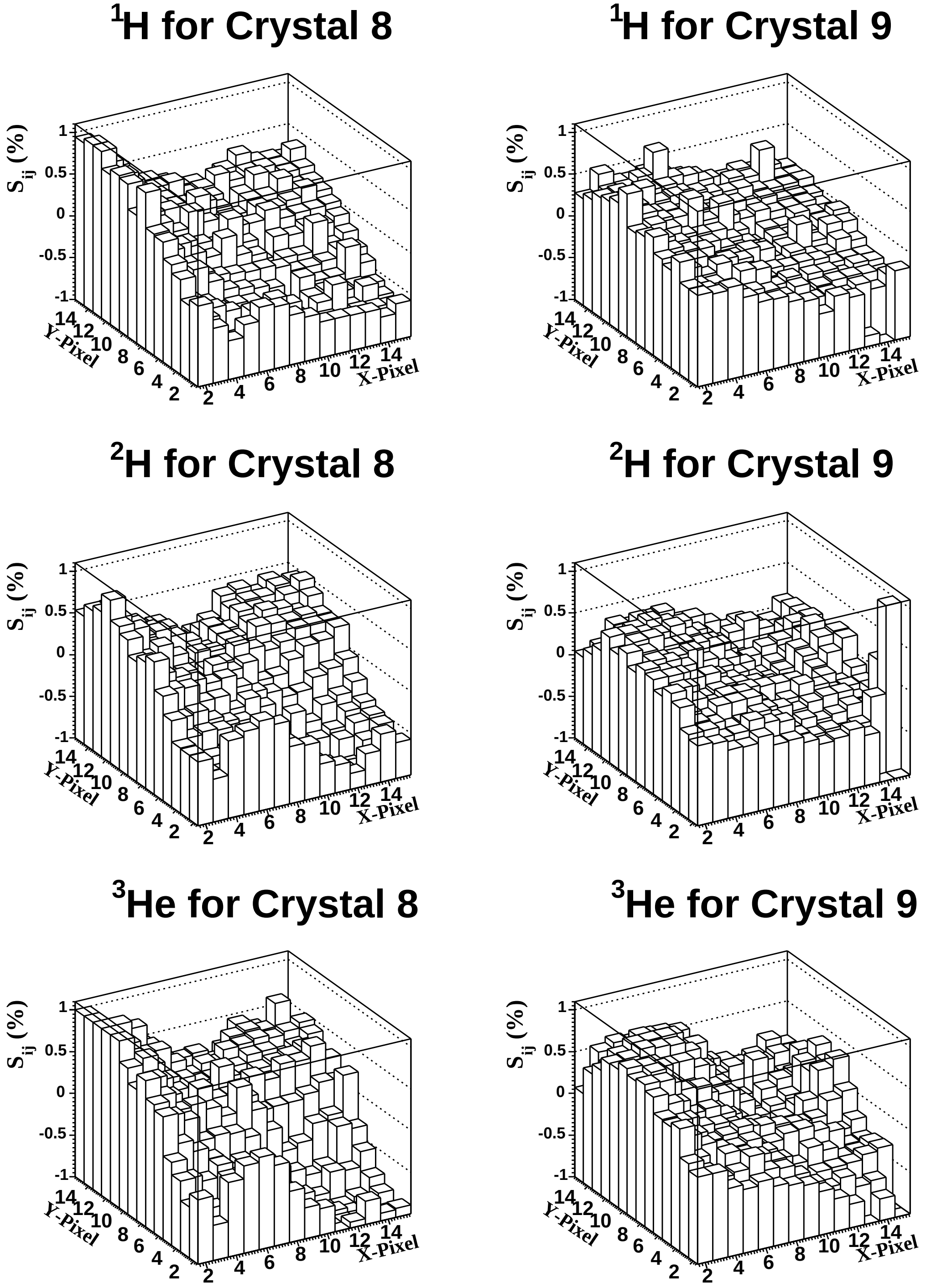

Figure 4.20: Non-uniformity values S_{ij} for HiRA crystals 8 (left side) & 9 (right side) for the indicated beam particles from the CCF at the NSCL. Each pixel is separated in both x and y directions from its neighbor by 2 mm.

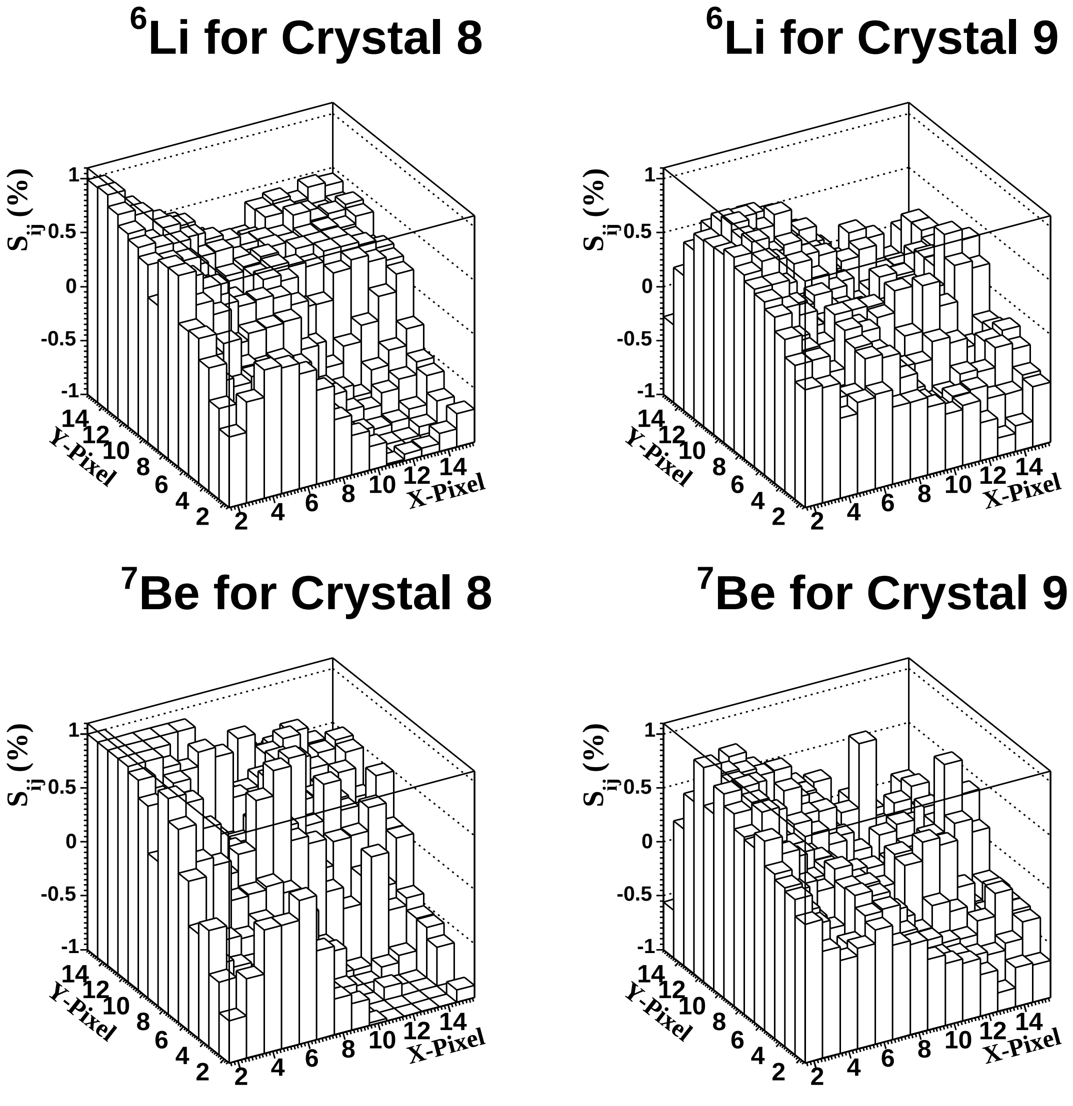

Figure 4.21: Non-uniformity values S_{ij} for HiRA crystals #8 (left side) & 9 (right side) for ^{6}Li and ^{7}Be

where a is a charge independent constant describing the conversion of energy loss into light and b is a charge independent constant describing how the light is quenched in regions of higher energy loss due to a saturation of the CsI(Tl) activation centers near the region of high ionization density. This later factor is responsible for the observed fact that $\frac{dL}{dx}$ decreases with charge [44, 45, 49–51]. It explains the stronger non-linearities in the energy calibrations for heavily ionizing particles and, in the context of this simple model, is the likely origin of the charge dependence of the non-uniformities shown in Figs. 4.20 and 4.21. Approximating the stopping power by

$$\left|\frac{dE}{dx}\right| \approx c\frac{Z^2}{v^2} \tag{4.7}$$

where c is a constant and v is the velocity of the particle and integrating Equation 4.6 over the ion's range in the CsI(Tl) detector, yields

$$L \approx aE\left[1 + \frac{bcAZ^2}{E} ln\left(\frac{\frac{bcAZ^2}{E}}{1 + \frac{bcAZ^2}{E}}\right)\right] \tag{4.8}$$

Both the constants a and b in Equations 4.6 and 4.8 may depend on the position where the ion traverses the crystal; of these two, only the position dependence of b can give rise to the non-uniformities displayed in Figures 4.20 and 4.21. According to Equation 4.8, the sensitivity to b is proportional to the stopping power; this suggests that the scaling factors $\alpha(Z, A, E)$ may also be proportional to the stopping power. A plot of $\alpha(Z, A, E)$ as a function of AZ^2/E is examined in Figure 4.22. Error bars are derived by considering the increase in α necessary to change the χ^2 value for the fit by one. A monotonic dependence of $\alpha(Z, A, E)$ on AZ^2/E is observed in support of this ansatz. There may exist a more accurate scaling relationship that this one depending on AZ^2/E, but a more complete set of data would be required to demonstrate it. This scaling behavior suggests that a practical correction to these non-uniformities may be obtained by measuring them for highly ionizing particles and scaling them down to obtain the corresponding corrections for more weakly ionizing particles. This

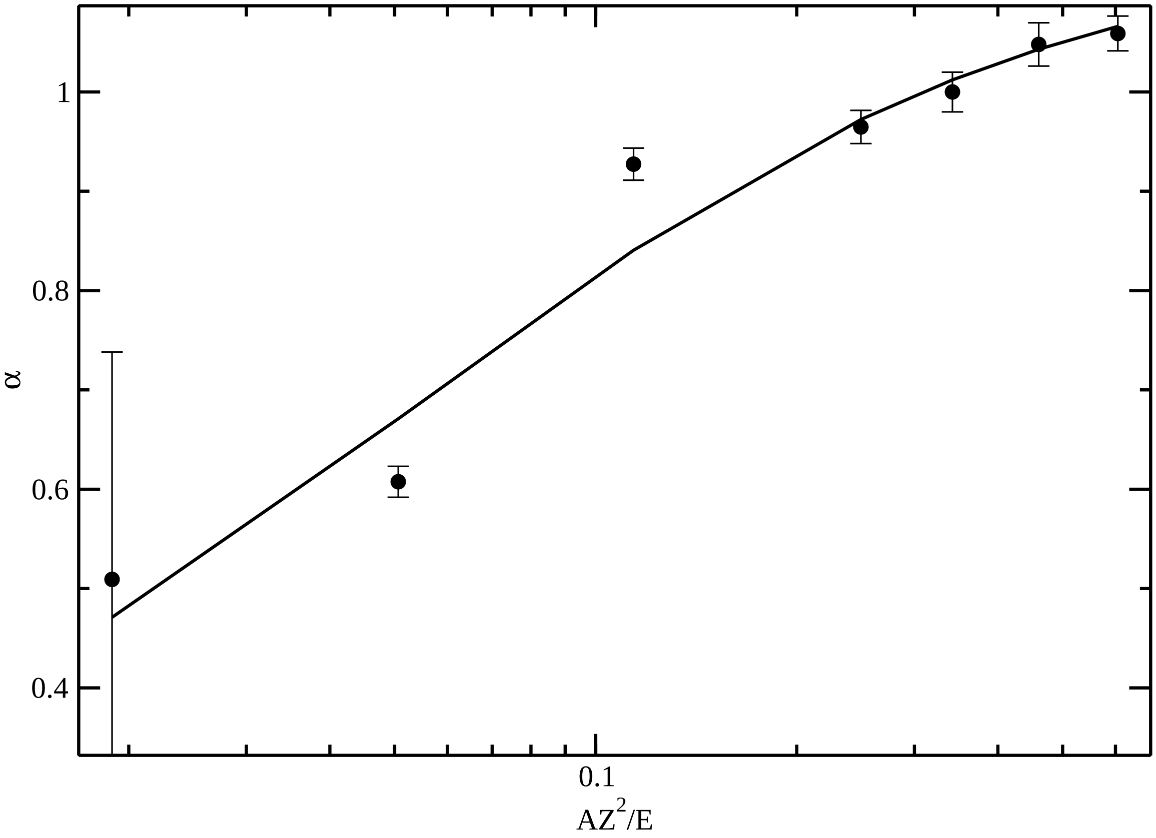

Figure 4.22: Scaling factor α, which describes the non-uniformity of specific isotopes with respect to that for ^{6}Li at E = 26 MeV/A for various particles and energies. By construction, we have a value of $\alpha = 1$ at $AZ^2/E = 0.34$ corresponding to the ^{6}Li fragmentation beam. The line is the fit to the non-linear term in Equation 4.8.

information can be used to design a full scale calibration for the full HiRA array when experiments demand the highest precision energy resolution in the CsI(Tl) detectors.

4.4 Electronics

With advances in silicon detector technology, larger detectors are being fabricated with smaller strips or pixels. These improvements are helping to advance nuclear, particle, and space based physics, however better resolution generally requires more electronics to process the signals. This cost for electronics can far exceed the cost of the silicon detector. Additional problems arise when size constraints exist. The power consumption for processing signals can also be quite high. For these reasons many of the larger projects in high energy physics or in space based physics have turned to Application Specific Integrated Circuits, (ASIC's) for signal processing. For the intermediate energy nuclear physics community, the complexity of devices have reached the threshold for discrete electronic signal processing. For the HiRA project a full set of high density electronics has been developed including the HiRA ASIC called HINP16. The supporting electronics will be discussed in detail below.

4.4.1 Application Specific Integrated Circuit (ASIC)

The HiRA detector is designed to be a versatile device that can be used in a variety of ways for a number of different types of experiments. For some experiments the energy deposited in the silicon detector is of the order of 50 MeV with particle multiplicities of the order of 1 per event. Some require timing resolutions around 1 ns, others require energy depositions around 500 MeV with particle multiplicities greater then 20. This makes designing a single ASIC difficult as the name suggests they are application specific. The HiRA ASIC contains charge sensitive amplifiers, pseudo constant fraction discriminators, shaping amplifiers, time to analog converters, and a sample and hold circuit along with the digital logic necessary for communication and multiplexing the signals out. There are 16 individual channels within each chip. Figure 4.23 is a block diagram representation of the functionality of the HiRA ASIC chip. The ASIC is fabricated in the AMIS 0.5 μm, N-well CMOS, double-poly, triple-metal high-resistance process through MOSIS [54].

The first element of the ASIC, the charge sensitive amplifier (CSA) consists of two different amplifiers as well as the option to bypass it completely. The choice of CSAs allow for high gain and low gain settings depending on the experiment or detector connected to the ASIC. The low gain CSA gives a dynamic range of $\backsim$500 MeV. The high gain setting allows particles up to $\backsim$100 MeV. The CSA takes up a large physical area on the chip as the large gain requires a large resistance for the load resistor and this is done with a large volume on the chip. If a larger gain is required then the chip

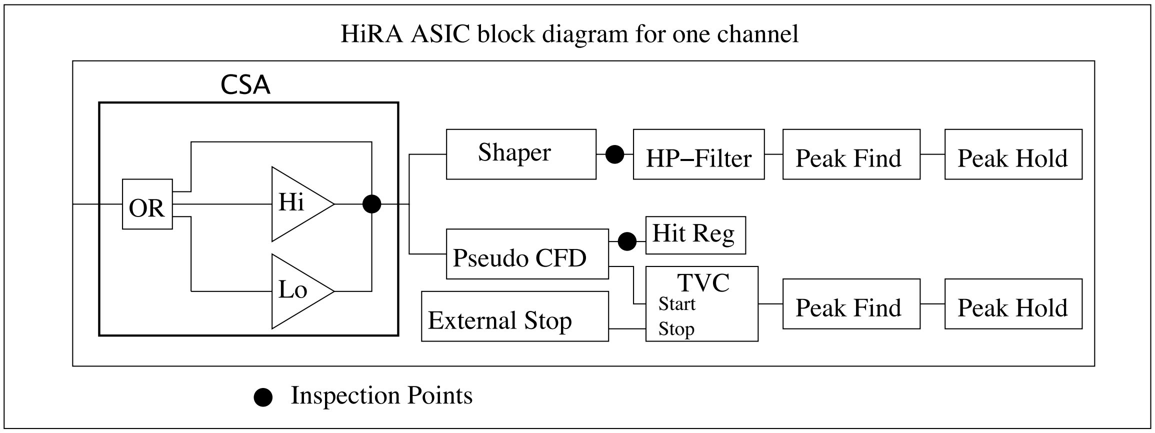

Figure 4.23: Block diagram of the HiRA ASIC.

can accommodate an external pre-amplifier, by bypassing the on-board CSAs.

After the signal is amplified by the CSA or external pre-amplifiers it is split with part of the signal going into the pseudo CFD after passing through a high pass filter. The pseudo CFD is a leading edge discriminator triggering a zero-cross discriminator. The other part is going to a shaping amplifier which will shape the signal into an approximate Gaussian shape, with a shaping time of about 1 μs. The signals can be positive or negative. The shaper is a unity gain amplifier so all the chip gain comes from the CSA.

The discriminator has a computer controllable trigger threshold which can be set both positive and negative for either input level and is controlled by an external DAC, for each of the 16 channels individually. The discriminator output has two functions. There is a hit register which can be used to determine trigger criteria. If the hit register for a channel is triggered the shaped signal will go through a peak find circuit and the peak value will be held until it is read out or forced clear. The discriminator will also start a Time to Amplitude Converter (TAC) which has two time settings of $\backsim$150 ns and $\backsim$1 μs. This is stopped by an external common stop signal. The peak of the analog time is then determined by a peak finding circuit and then stored until it is read or forced clear.

The chip also has a computer controlled external display of the signal after the

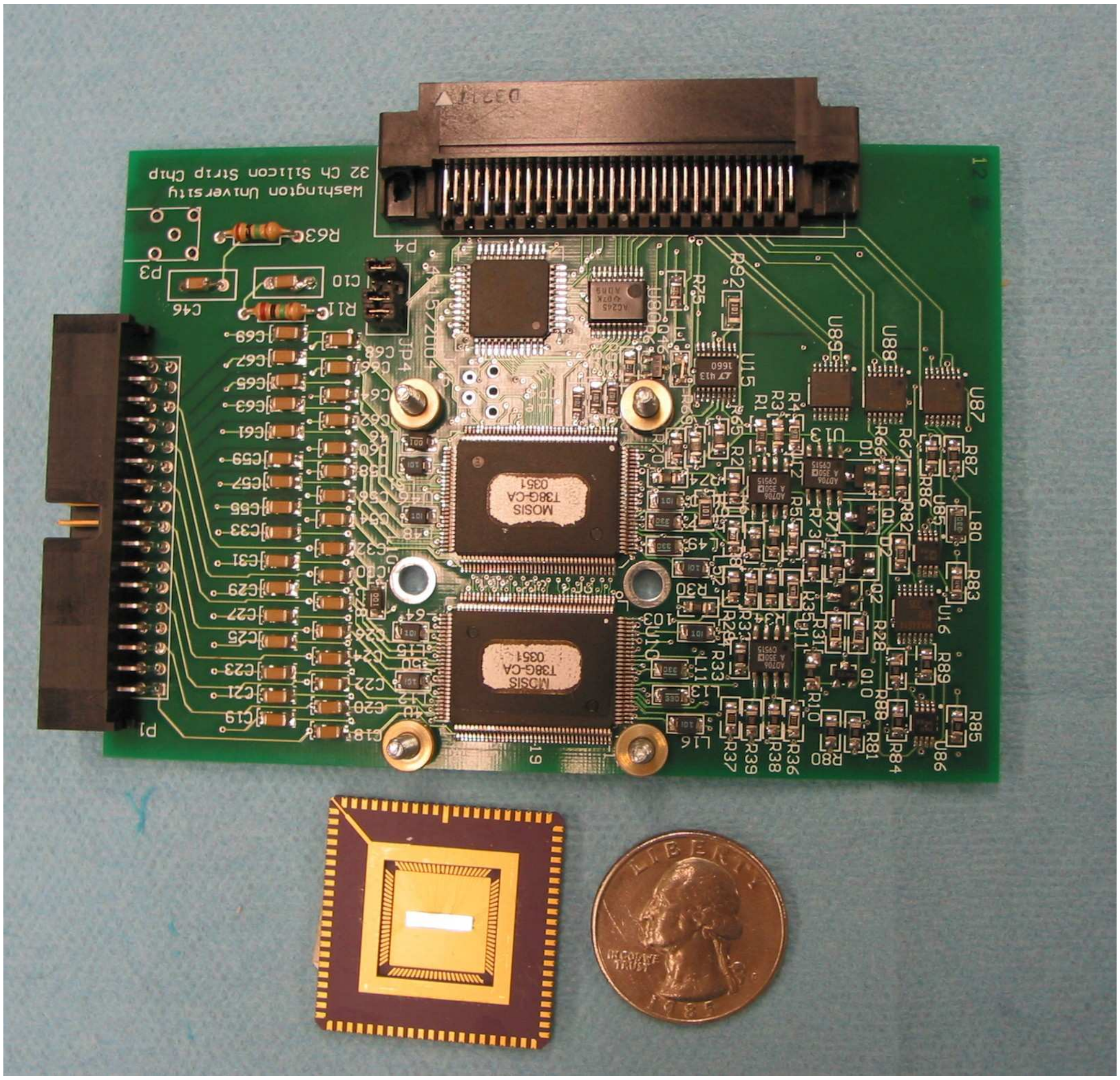

Figure 4.24: Picture of the HiRA chipboard. There are two ASICs on this board in the middle of the board. Below the board is a 4 channel prototype ASIC with the cover off exposing the actual chip inside the packaging. A US quarter is displayed next to it for size reference.

CSA, after the shaper, and the discriminator logic signal as denoted by solid black circles on Fig. 4.24. There are also 3 computer controlled Or signals which can be set to have any number of the chipboard Or signals. There are three Sum signals, which are also controlled by computer. The Sum signal represents an analog level based on the multiplicity. There are 6 linear inputs for pulsers. They are divided into 3 for even channels and 3 for odd channels. These are configured by jumpers on the motherboard.

4.4.2 HiRA electronics

The HiRA silicon detectors have 32 strips per surface, so two ASICs are used per surface. The ASICs are mounted on chipboards in pairs along with several other components. Figure 4.24 shows one of the chipboards with two ASIC chips on it. Below the chipboard is a 4 channel prototype chip with the cover off exposing the actual ASIC. A US quarter is placed next to it for size comparison. Additionally on the chipboard are bias resistors and decoupling capacitors for the bias voltage going to the detectors as well as a computer programmable logic device (CPLD) which was added to correct some communication problems with the chip. There is a differential amplifier on each chipboard for the Energy and Time signals. These signals are multiplexed out of the chips and into the differential amplifier generating a differential signal between -1 V and +1 V.

Each surface of silicon on a detector requires one chipboard therefore three are used for each telescope. An additional circuit board called the “motherboard” is used to organize several chipboards and merge the input and output signals. The first set of experiments with HiRA utilize detectors aligned in towers, as will be described in Section 4.5, which allow up to 5 detectors to connect together. A motherboard was built that can accept 15 chipboards, which are needed for a tower.

The motherboard contains a field programmable gate array (FPGA) circuit. There are many level translators between the FPGA and the other circuits on the chipboards because the logic used by the FPGA is TTL and the communication with the motherboard goes via low voltage differential signals. The FPGA is used to communicate with up to 30 chips on the 15 chipboards that the motherboard can service. For each motherboard there are two linear outputs. One contains the sequence of energy values for all channels that have a valid hit register event. The other carries the corresponding time values from the TVCs. In addition to this, there is logic information coming out on a high density logic control cable to communicate the address of each energy and time value sent out from the motherboard.

Outside of the motherboard, one only needs two VME modules to handle all information with the electronics. The first is a SIS3301 105 MHz sequencing ADC that contains 4 pairs of sampling ADCs. Each motherboard uses one pair from the sampling ADC. The connection from the motherboard to the ADC is via a dual lemo cable. There is an external clock input that tells the ADC when to sample each of the four pairs. The control of the readout and the storing of addresses from each motherboard along with the ADC clock, is handled by an XLM80 universal logic module made by JTEC. The XLM80 contains an additional FPGA which is programed with the trigger logic sequences for the silicon detectors.

Figure 4.25 is an oscilloscope trace of the energy signals of one motherboard. The two components of the differential signal are shown in dark blue and pink. The light blue trace on the top is a NIM signal which serves as the trigger for digitization of the ADC samples. The energy is determined by measuring the difference between the dark blue and pink traces at the time the light blue logic signal is true. This trace is for a motherboard with 8 channels read. The vertical scale is 500 mV per division and the horizontal scale is 4 μs per division.

The ASICs were designed to run in sparse readout, where the discriminator for a specific channel is required for readout of that channel to occur. This is highly desirable as the readout time for an entire tower can be quite long. There are situations where one might want to force read electronic channels that did not trigger their

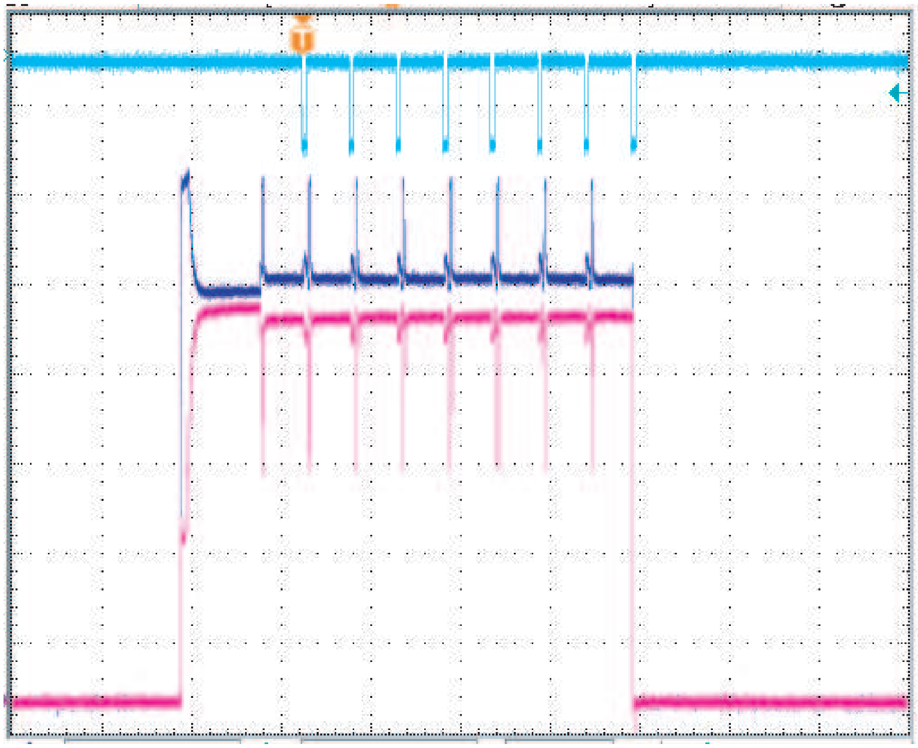

Figure 4.25: Oscilloscope trace of motherboard energy signals

discriminators. For this reason software was developed to force the discriminators on all channels to trigger, initiating a full read of all detectors connected to this motherboard.

While the silicon signals are all being processed by ASICs, XLM80, and SIS ADC, the photo-diodes used to readout the CsI(Tl) are processed in a more traditional system. There are individual pre-amplifiers housed within the HiRA telescopes that are connected to Pico Systems 16 channel CAMAC shaper discriminator units housed in a CAMAC crate outside of the chamber. The shaped signals are processed by CAEN 32 channel VME peak sensing ADCs, also mounted in a rack outside the chamber. Both are read and controlled by the VME based Data Acquisition System.

4.5 Mechanical

The mechanical design for HiRA was primarily done at Michigan State University, with important contributions from INFN Milan. Figure 4.26 shows a 3-d rendering

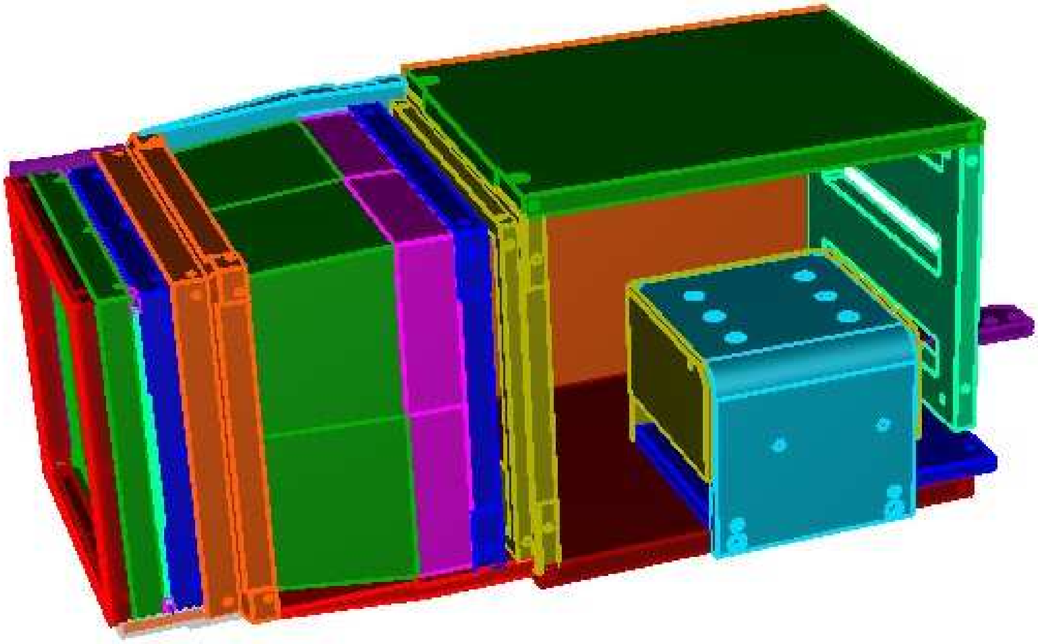

Figure 4.26: Technical drawing of a HiRA detector box

of the detector structure. Shown in red are two frames. The front frame with a foil attaches by 4 dowel holes and is used to enclose the box, electronically shielding the detectors in the box. Moreover, if the foil is to be a high Z material, it shields the detector from soft X-rays and electrons. Behind that is a collimator frame which can prevent low energy particles from entering the silicon frame or dead area of the silicon wafer. This frame has dowel pins epoxied in the corners. On the front side of the frame the pins insert into holes in the front frame and on the back they stick into holes in the frame of the DE detector, providing alignment. The frame for the DE detector is shown in green and was described in Section 4.2. Behind the DE there is a small frame that can be used to hold an α source as described in Section 4.5.3. Behind the source frame is the frame to the detector described in Section 4.2. This stack of frames mounts to the orange frame in Fig.4.26, which has dowel pins on the front which insert into the E frame for alignment.

This frame also acts as a mount for the CsI(Tl) crystals as there is a ridge on the inside which is slightly smaller than the crystals. The 4 crystals, shown in green, are wrapped together and sit in the front frame. A support piece for the crystals, shown in blue is behind the crystals. It screws into the side plate and pushes the crystals against the orange front frame. Behind the crystal box, there is a smaller copper box shown in blue that contains CsI(Tl) pre-amplifiers. This copper box is connected to cooling bars. This area of the box in the back is also used for the silicon cable to mount to a PC board that is not shown here. This board is used to re-align all three cables to come out of the telescope horizontally, simplifying cable routing between telescope and chip electronics.

4.5.1 Electronics structure

The detectors are mounted within the unit of telescope as previously described, however the electronics also need to be mounted within the chamber in order to optimize the energy resolution. A box was designed to mount one motherboard with 15 chip-

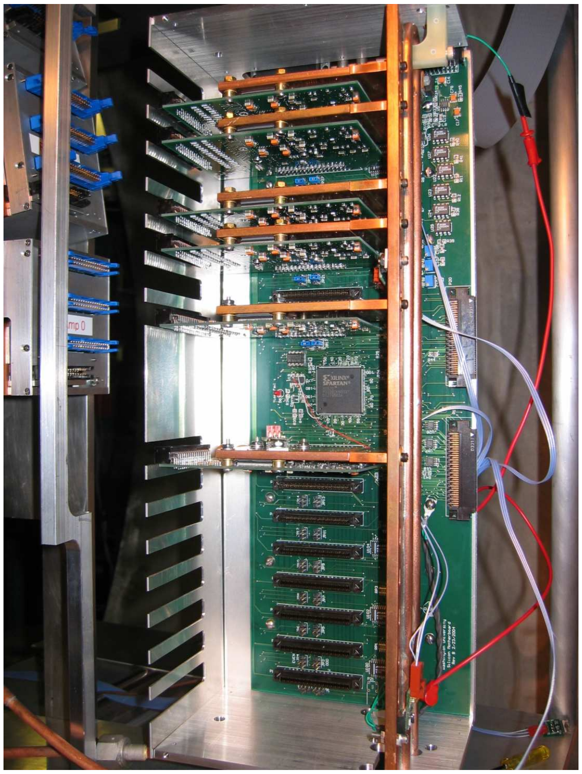

Figure 4.27: Image of a motherboard inside its shielding box. Also shown are the cooling bar configuration designed to keep the ASICs cool in vacuum.

boards on it. Each chip needs active cooling in vacuum as they draw about 1.5 Watts per chipboard. Figure 4.27 shows a picture of one of these boxes open. There is a copper bar on the back side of the box with copper fingers attaching each chipboard to the copper bar. These copper fingers are attached to the chipboard with thermally conductive, electrically insulating foam padding between the top of the ASCIs and the copper finger. The copper bar in the rear is thermally isolated from the box by a plastic connection at the bottom. This is done to reduce the thermal load on the colling system. The whole system is cooled by water flow from a refrigerator unit outside of the vacuum chamber.

4.5.2 Supporting structure

While the individual HiRA telescopes can be mounted in many different configurations some work has gone into standardizing how telescopes will be mounted for

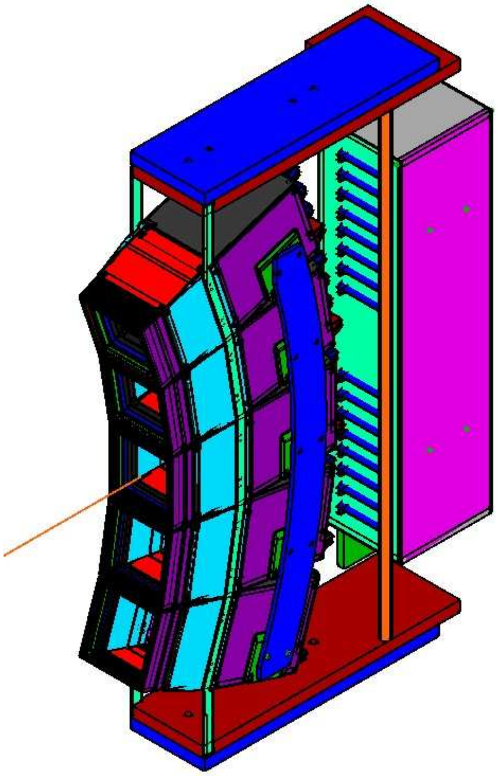

Figure 4.28: 3-D rendering of a HiRA tower unit

most experiments. This is necessary as telescopes must have cooling for the CsI(Tl) pre-amps. The electronics box also needs to be mounted in close proximity to the detectors. Figure 4.28 shows a 3-D rendering of a tower unit. In the figure, five telescopes are shown mounted using keys along the sides. There is a copper cooling bar that is shown in blue here which attaches to the CsI(Tl) pre-amp boxes on the back of the telescopes. The silicon electronics box is mounted to the tower behind the detectors which will minimize the length of cable between the detector and the electronics.

For experiments where HiRA is placed at forward angles, around the beam, a mounting system for towers has been designed and built. Each tower is placed on a rail system allowing access by sliding along the rail. There are dowel pins to lock a tower into position during an experiment. The whole system resides on a large plate. Figure 4.29 is a 3-D rendering of this full system. Also shown here are the micro

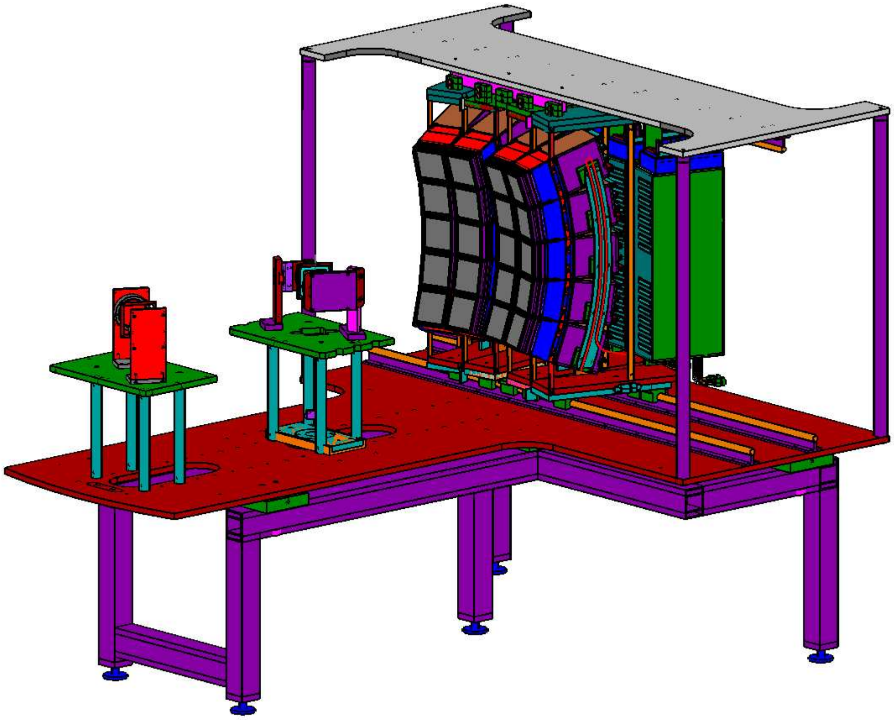

Figure 4.29: 3-D rendering of the entire HiRA system

channel plate detectors which are described in Chapter 5.

4.5.3 Pin source design

Figure 4.30 shows the front area of a HiRA detector. There is a slot on one side of the silicon box. This is designed to fit a calibration source between the silicon detectors. The telescopes were designed such that they can be mounted together using “keys” which connect the sides of two telescopes. The keys fit along the ridge show in Fig. 4.30 near the back. The keys use two screws and can also take two dowel pins as well.

Each telescope of HiRA has two silicon detectors, the second one being completely behind the first. This makes access to the second detector difficult in order to calibrate using α sources. For every experiment using the silicon detectors an α calibration is required. Any time silicon detectors are handled there is a risk of accidental damage. Minimizing the number of times detectors are mounted and unmounted is advisable. Therefore, in the designing of HiRA a small slotted frame is mounted between the DE

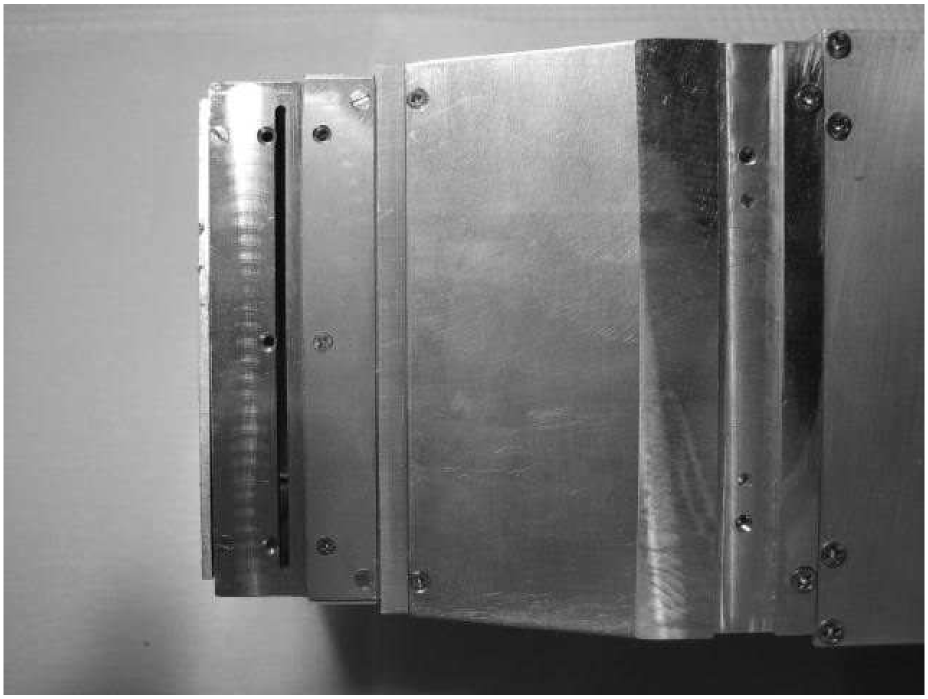

Figure 4.30: Image of the front part of a HiRA telescope

and E detector. The frame thickness is 1.7 mm, which does not affect the experimental design however it is enough to slide a thin frame, with an α source on it, between the silicon detectors. The mounting frame has dowel pins epoxied in each of the four corners with both ends sticking out for alignment and mounting of the silicon detectors.

Figure 4.31 is a picture of one of these source frames. The pin is a 0.5 " dowel pin. This pin is activated by electroplating the tip with daughter nuclei from a ^{228}Th source. The source can be generated in 24 hours or less and then glued into the frame. There are three strong alpha lines from this source at 8.785 MeV, 6.050 MeV, and 6.089 MeV. The primary deposition on the pin is ^{212}Pb which has a half-life of 10.6 hours. There is a small amount of ^{224}Ra deposited on the pin as well. It has a half-life of 3.62 days. This adds three more alphas with energy of 5.685, 6.288, and 6.778 MeV. As there is no additional material between the radioactive nuclei and the surface this source can produce very sharp energy spectra.

The pin source is capable of hitting all pixels on the E detector as shown in Figure

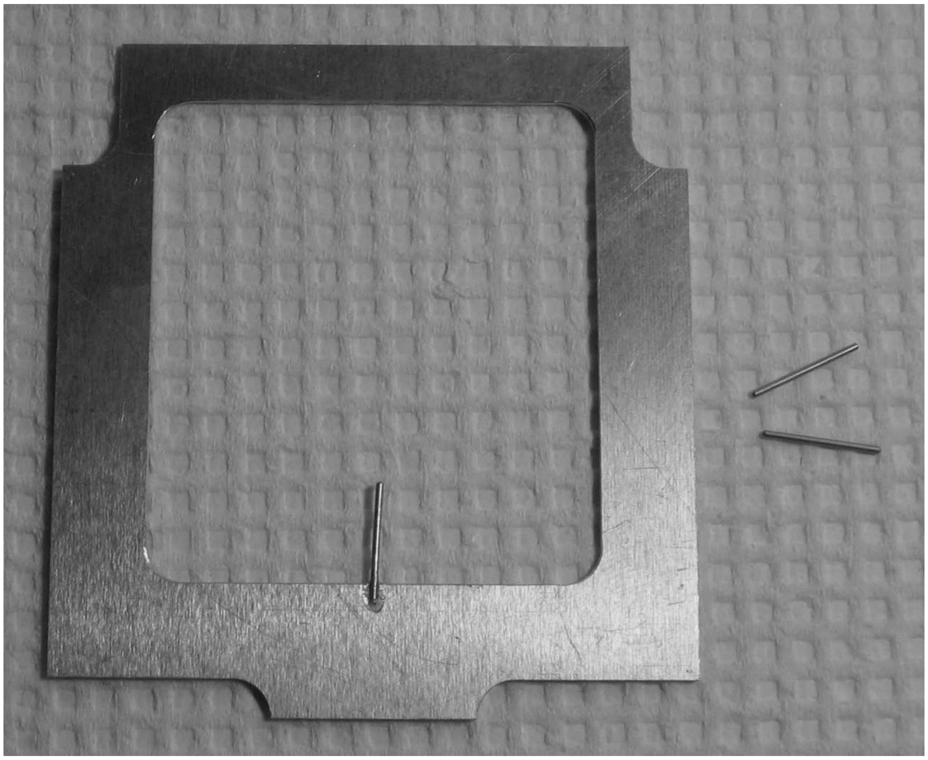

Figure 4.31: Image of the α source frame used to calibrate the E detector without removing the DE detector. Extra pins are shown on the right.

4.32. Due to the close proximity to the silicon surface, a few mm, the α particle strikes the surface will large angles for pixels that are not near the center. The dead layer on the surface of the silicon will shift the energy of the alpha particles and diminish the energy resolution. If there is enough data from reactions with the beam, one can calibrate using only the pixel or pixels directly in front of the pin source, thus avoiding problems with angle and dead layer measurements.

4.6 Calibrations using pin source

Given the nature of double sided silicon detectors it is possible to calibrate the energy for all strips if one can accurately calibrate a single strip on the front surface and the back surface. Using the pin source, Strip 16 on the front and back are calibrated. Figure 4.33 is a histogram of strip 16 on the front surface of a E detector taken with a pin source inserted between the DE and E detector. This histogram is gated on

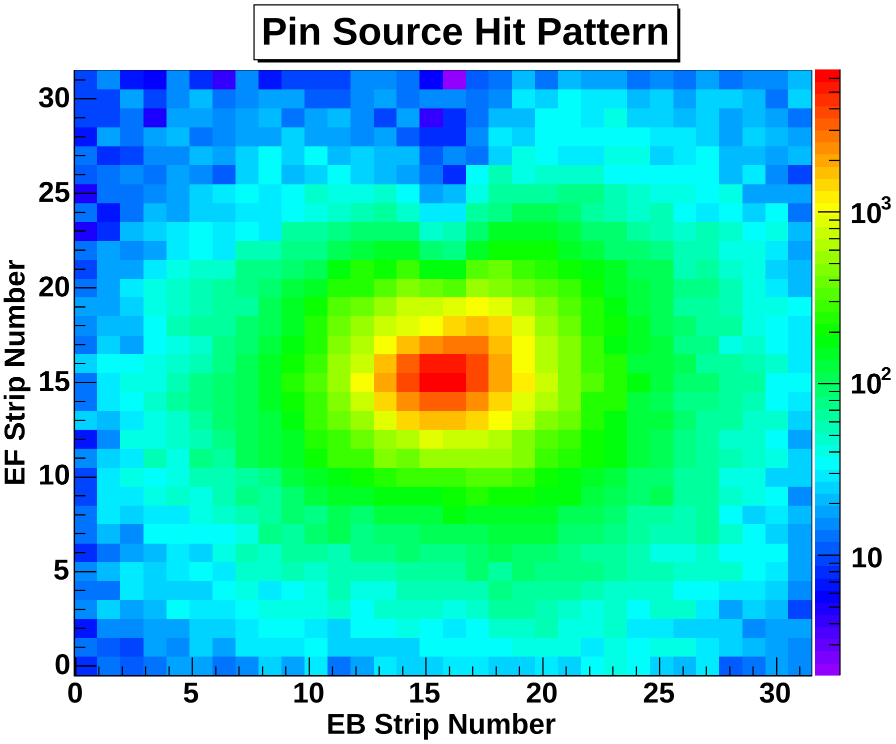

Figure 4.32: 2-D hit pattern for α particles from a pin source inserted between the DE and E detectors.

multiplicity 1 events on both front and back, requiring a signal in strip 16 on the back. This effectively selects α particles that hit the central pixel, 16-16. This pixel should have zero incident angle giving the most accurate energy measurement. The two high intensity alpha peaks are fitted, and a linear calibrations is done for these two strips. New parameters are then generated with strips 16 on EF and EB calibrated in MeV.

For every particle incident on the silicon, the energy is measured in one strip on the front, and one strip on the back regardless of where the particle hits the surface of the detector. The energy measured for each should be exactly the same. All particles that are incident on EF_{16} can be used to calibrate the corresponding EB strip. Figure 4.34 shows the profile in X from a 2D histogram of counts vs the energy deposited in EF_{23} or EF_{29} and in EB_{16}, where the latter has been calibrated using the pin source. The vertical lines represent the error bars from the profile. Larger errors are due to a small number of particles with that particular energy. The slope for each of these

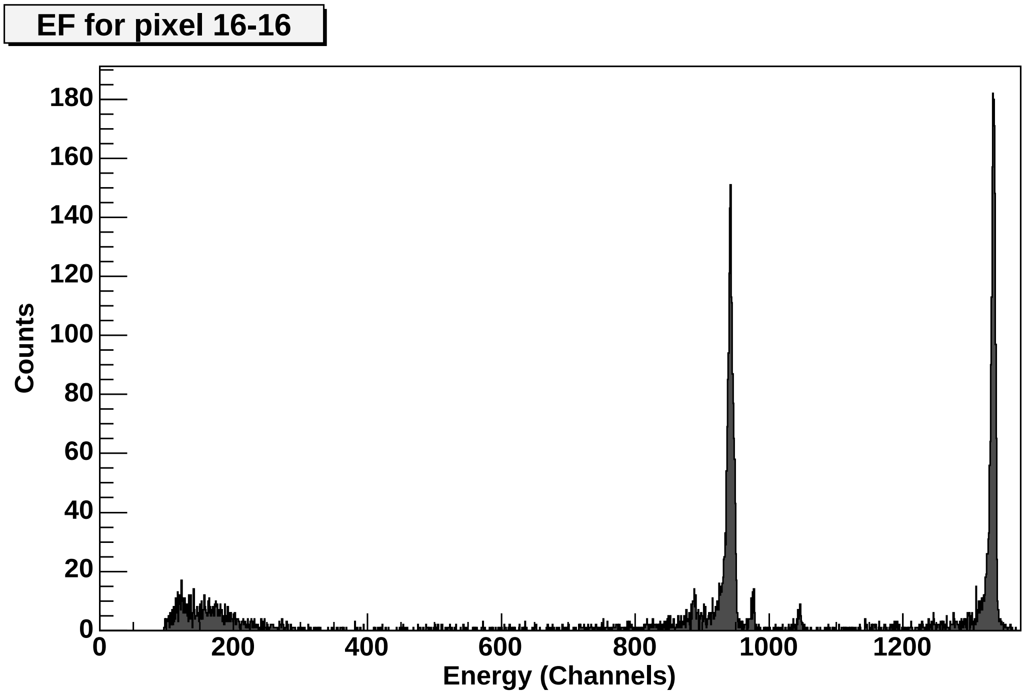

Figure 4.33: Raw energy spectrum for strip EF_{16} gated on pixel 16-16

lines is different. A linear fit of the form:

$$EB_{16} = M \cdot EF_i + B \tag{4.9}$$

is done where M is the slope of the lines shown in figure 4.34 and B is the Y-intercept. EF_{23} and EF_{29} are then calibrated using these parameters.

After applying these corrections, EF_{23} and EF_{29} when plotted against EB_{16} show the same calibrated relationship. This is shown in Figure 4.35.

4.7 Particle identification

Of critical importance in HiRA is the ability to identify the masses and charges of particle, in addition to energy. To do this HiRA relies on the technique of ΔE vs E identification. The principle of this is the Bethe Formula given in Equation 3.4. It shows that the energy loss ΔE is proportional to AZ^2/E. Therefore a plot

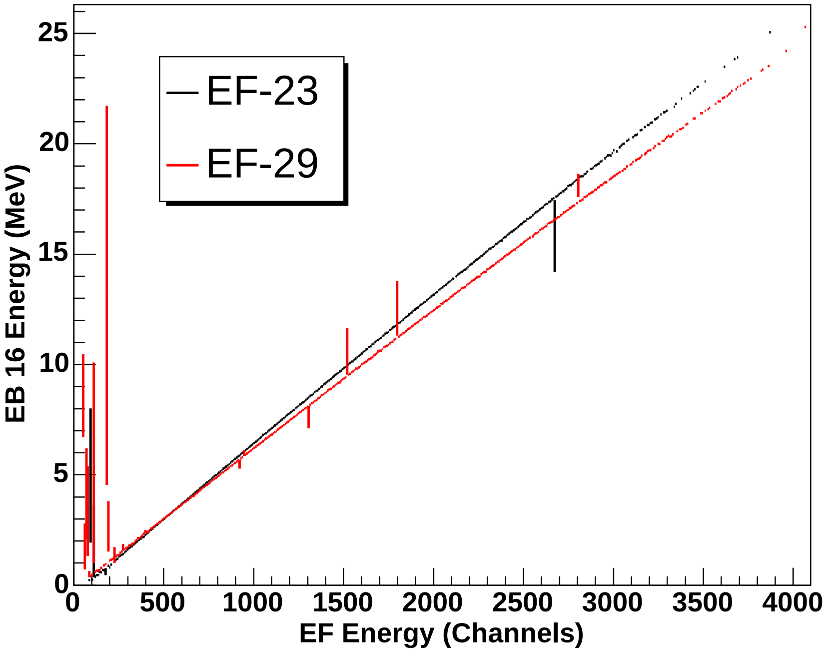

Figure 4.34: Profile histogram for two strips on the front surface, EF_{23} and EF_{29} vs the calibrated EB_{16} Strip

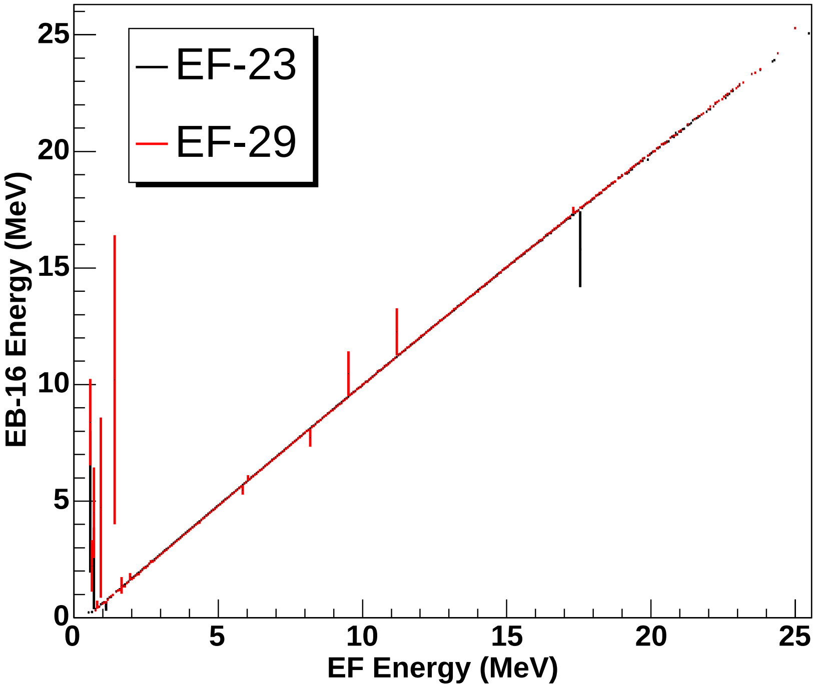

Figure 4.35: Profile histogram for two strips on the front surface, EF_{23} and EF_{29} vs the calibrated EB_{16} strip after cross calibrations from back strip

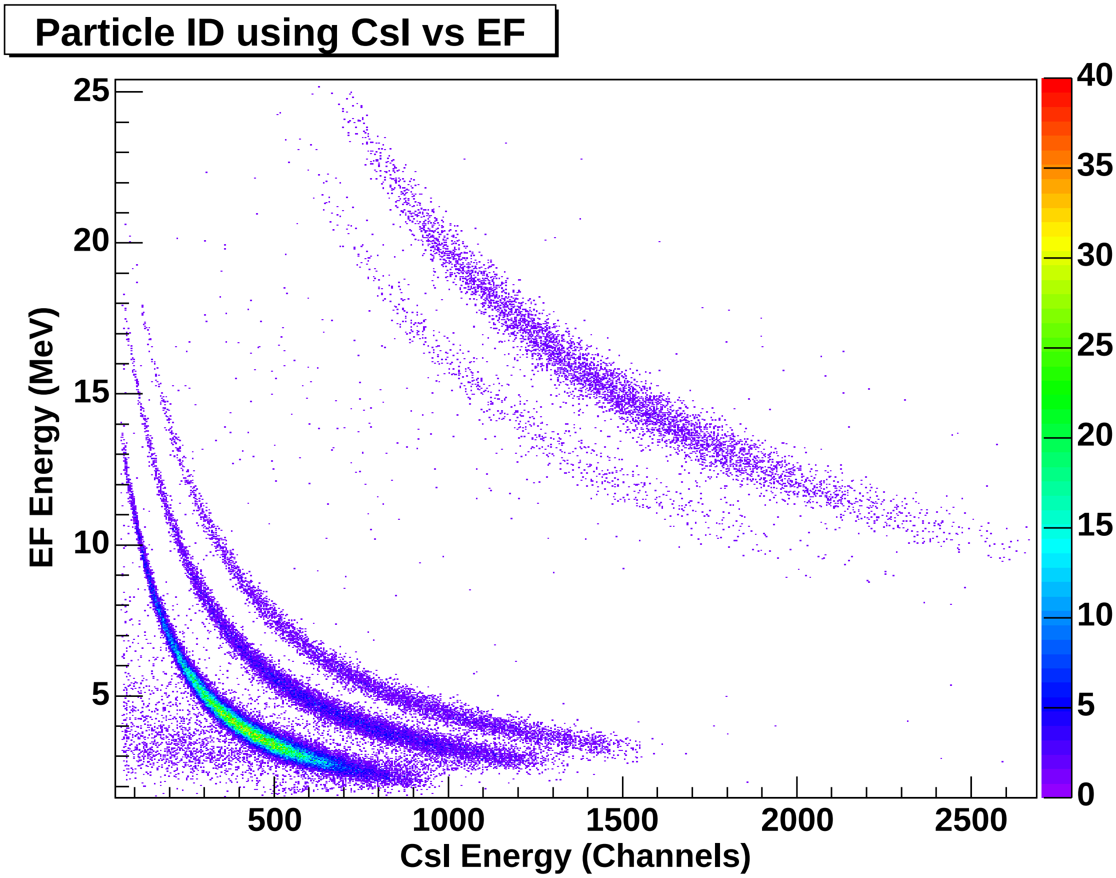

Figure 4.36: Particle identification plot using EF vs CsI

of ΔE vs E will identify AZ^2. There are two types of ΔE vs E plots that are used to identify particles detected with HiRA depending on the incident energy. For high energy particles that penetrate into the CsI detectors the EF or EB is used as a ΔE detector, with the particle stopping in the CsI, which is labeled as the E detector. Figure 4.36 is a ΔE-E plot for particles produced by a ^{40}Ca beam impinging on a plastic target. One can see lines corresponding to p, d, t hydrogen isotopes as well as lines corresponding to ^{3}He and ^{4}He, with little above this.

If the energy of particles is lower, then the particles can stop in the second silicon detector. In this case the DE detector measures ΔE and EF or EB gives the residual energy. Figure 4.37 represents the corresponding ΔE-E plot obtained in the beam described above. Clearly HiRA can identify both the charge number (Z), and the mass number (A) for such light charged particles. No data was measured for heavier

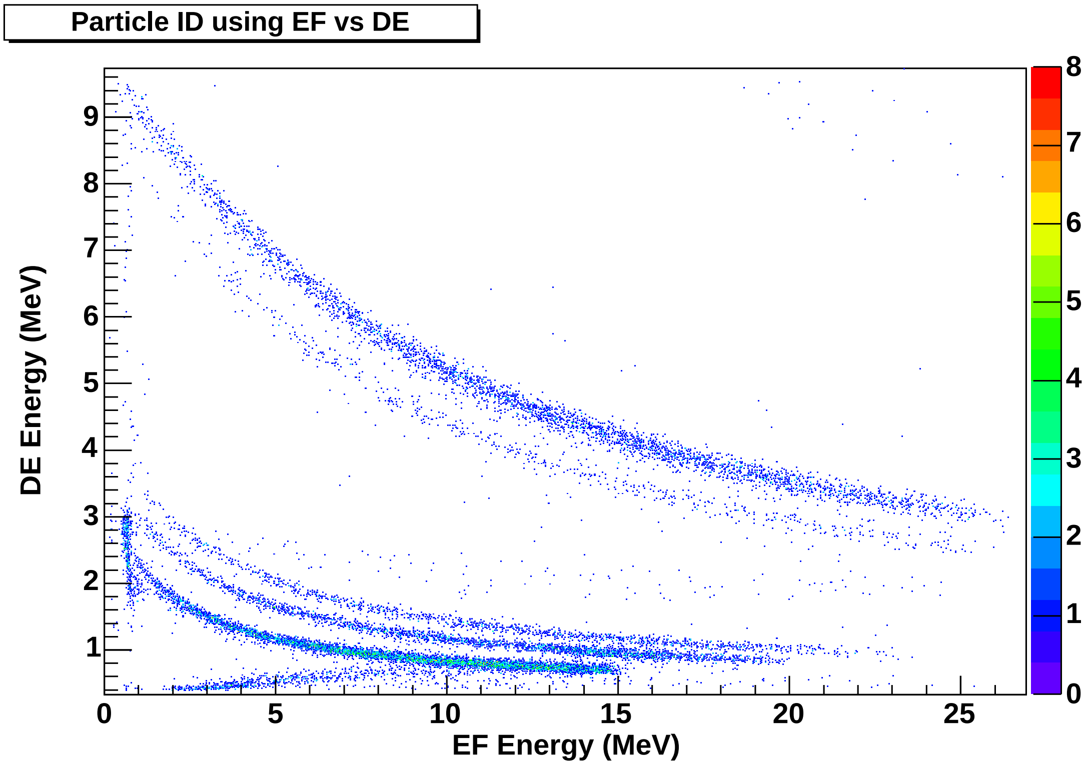

Figure 4.37: Particle identification plot using DE vs EF

fragments however HiRA is expected to allow identification up to oxygen isotopes.

Chapter 5

Beam tracking detectors and the full experimental setup

5.1 Introduction

The HiRA detector is only one component needed to perform (p,d) transfer reaction mass measurements. Beam tracking is required for the determination of the reaction angle and the beam energy required to reconstruct the mass. This chapter will cover the detectors used for this purpose. A full description of the experimental setup will then follow.

5.2 Beam measurements using Parallel Plate Avalanche Counters (PPACs)

Using the simulations described in Chapter 3, it was determined that a measure of the incident beam angle striking the experimental target has a dramatic effect on the mass resolution. Initially, Parallel Plate Avalanche Counters (PPACs) were going to be used to determine this beam angle. PPACs have been used at the NSCL for position sensitive particle detectors for quite some time, making it the natural choice.

The traditional PPACs used at the NSCL consist of an entrance foil, with aluminum strips evaporated on the surface in the horizontal direction, a center foil, and an exit foil, with strips evaporated on the surface in the vertical direction. Isobutane gas fills the region between these foils. The strips are connected by a chain of resistors. The signals are measured on both sides of the resistor chain. The voltage difference across the resistor chain provides a measure of the X, Y coordinates for the beam particle trajectory through the gas. This method gives position resolution better than 1 mm, however it is limited in overall beam particle rate acceptance.

The PPAC signal has two components. The first component, which is quite fast, comes from the electron signal. The second component comes from the drifting ions. The fast signal is a few nanoseconds wide, while the slow ion signal is about a microsecond long. The slow ion signal is larger in total signal amplitude. When using a resistive chain, the signal to noise ratio is low, requiring one to use the ion signals. One must operate at voltages near the breakdown point. The use of slow signals limits the acceptable rate as pileup of the signals will occur at modest beam rates. The high voltage required to amplify the signal adequately above the noise will prevent the detector from being used above 1×10^4 particles per second (pps). For the experiments of interest in this thesis beam rates of 1×10^6 pps are anticipated.

To improve the rate limits of a PPAC one needs to operate with lower voltages to reduce the possibility of sparking. One also needs to reduce the likelihood of pileup on electronic channels. Individual strip readout will simultaneously solve both of these problems, or at least improve them. Individual strip readout will reduce pileup as the beam rate on each strip is significantly lower then the overall beam rate. Without a resistive chain connecting all strips, the noise is lower, therefore the detector can be operated at a lower bias voltage while still providing an adequate signal to noise ratio.

The strip pitch is about 1.25 mm, which requires a large number of electronic modules to process all signals using traditional electronics. To avoid using large amounts of CAMAC and NIM electronics the PPACs signals are processed with Front End Electronics (FEE) boards designed for the STAR Time Projection Chamber (TPC) at the Relativistic Heavy Ion Collider (RHIC) at Brookhaven National Lab.

These FEE boards contain ASIC chips that have charge sensitive amplifiers, shapers, a switched-capacitor array (SCA), and a 10 bit ADC for each strip. The SCA is an analog storage device that saves the wave form from each strip. The SCA is constantly sampling and storing until a trigger is given from some external detector. The FEE boards then digitize the waveform for each strip. The SCA has 32 elements, with an element width that can be programed between 25–100 ns each. This requires a trigger decision to be made within 3.2 μs after the event. After this time the SCA will overwrite the existing data with current data.

Beam tests were performed to measure the resolution and rate capabilities on these detectors. The multiplicity of strips with signals above threshold was about 5. One can calculate a centroid peak to better than the width of a single strip (1.25 mm) with this multiplicity. The beam rate these detectors can handle will vary with beam species, in the initial beam test with a ^{78}Kr beam at 60 MeV/u the PPACs counted at a rate up to 5×10^5 pps, but then they began to spark. This was significantly better than with the original PPACs, however it was not sufficiently stable to allow the use of the modified detectors for experiments described within this thesis. Moreover, one would not place these PPACs near the target because they have a thickness of about 10 mg/cm^2 of plastic, which is ten times as large as the thickness of the actual target. If placed near the target, these detectors could produce a high background.

By placing the PPACs in the intermediate image of the S800, the magnetic elements between the PPACs and the target largely eliminate the PPAC induced background from the experiment. However, this placement has several disadvantages. First, ion optics calculations are necessary to determine the position at the target. It is not clear how accurately this can be done, or how stable the result might be. Second, some losses of beam from charge exchange occur whenever one puts material such as a PPAC in the beam. This reduces the actual beam transmitted to the target. Based on these complications a new tracking system using micro channel plates was pursued.

5.3 Micro Channel Plate detectors

Micro Channel Plate detectors (MCPs) are extensively being used for particle tracking at Oak Ridge National Laboratory (ORNL) [55–57]. They have the advantage over PPACs of requiring less material to be inserted in the beam. In collaboration with Dan Shapira of ORNL, a tracking system using MCPs was developed at the NSCL. A description of the design of this system will follow. The results of initial tests will also be given.

5.3.1 MCP design

A micro channel plate is a thin plate made by packing many small glass tubes very close together and coating them with material having a low work function for electron emission. Figure 5.1 shows a graphic illustration of an MCP. The horizontal lines represent the inner surfaces of an electron tube. The dimension of the tube are not drawn to scale. Typically, the diameter of a tube is about 10 microns while the length is typically about 1 mm. When an electric field is applied between the front and back of the plate, each glass tube acts like a small continuous channel photomultiplier. An electron that strikes the inner surface of a tube will cause the emission of additional secondary electrons, thus generating an avalanche of electrons that emerges on the other end of the tube.

The MCPs in our system have an outer diameter of 50.05 mm with an active diameter of 40 mm. The channel diameter is 10 μm with a center to center distance between adjacent channels of 12 μm. The thickness of the plate is 0.46 mm. The plate is cut with the glass tubes at an angle of 8 degrees from normal. Two plates are used

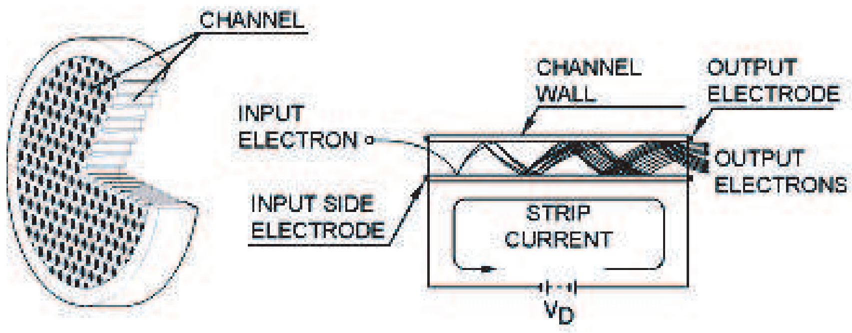

Figure 5.1: Schematic design of a Micro Channel Plate

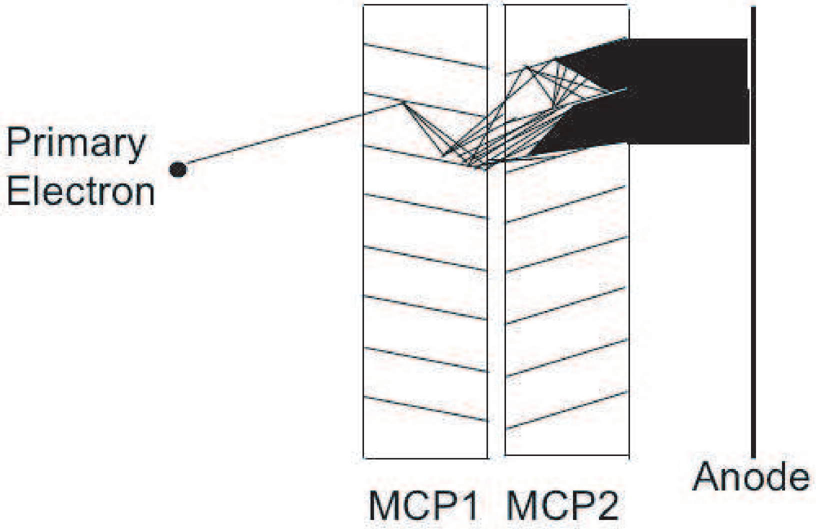

Figure 5.2: View of chevron style MCPs

in our MCP system, with the second plate oriented so that the 8 degree slant of its channels are oriented in the opposite direction, as shown in Figure 5.2. This is done to avoid electrons passing through without contact with the walls, and to prevent ions from traveling in the opposite direction and generating additional delayed secondary electrons. The electron gain from each plate at 1000 V bias is 10^4 corresponding to a total gain of between 10^7–10^8 through the pair of plates.

Behind the MCPs is an anode which collects the charge emitted from the MCPs. The anode is made of a thin resistive layer. The charge from the electrons cascading out of the second MCP is collected on the anode and collected at four corners on the anode. The position is determined from relative signal amplitudes of these 4 signals.

Figure 5.3 shows a schematic view of the MCP detector system. When a beam particle strikes the foil, secondary electrons are emitted. The foil is at a voltage of -1000 V with respect to the front surface of the MCP. This voltage accelerates the electrons from the foil to the MCP. The magnetic field created by the permanent magnets, behind the target and MCP, confine electrons along a narrow trajectory to the MCP. The position where the electrons are emitted from the foil is strongly correlated with the position on the MCP.

In order to use the MCPs for measuring the incoming angle and position on target they must achieve position resolution consistent with the requirements detailed in Chapter 3. In addition to position resolution, they must function at a beam rate of 1×10^6 pps and have a high efficiency for detection of heavy mass beams at such rates. Timing resolution sufficient to identify beam particles within an isotone chain would also be ideal. Most of these properties can be tested using alpha sources. A cyclotron beam is required however to determine the efficiency for heavy particles at high rates.

In the traditional design of the detectors, signals from the corners would go through charge sensitive amplifiers, shaping amplifiers, and into ADCs. The difference in the amplitude of the digitized pulses was used to determine the position. Such a readout gives very good resolution, typically better then 1 mm. The time it takes to process shapers and ADCs is on the order of several microseconds. Pileup in such electronics would limit the rate to about 10^4 pps.

The electronic readout system therefore required changes in order to achieve rates up to 1×10^6 pps. In the revised system the four corner signals are amplified by fast amplifiers, and digitized by QDCs. The amplified signals have a total width of less than 30 ns. This prevents significant pileup from occurring in the electronics at rates below 1×10^6 pps. A QDC gate of 50 ns is used for the corner signals, which corresponds to a probability of about 5% at 1 MHz.

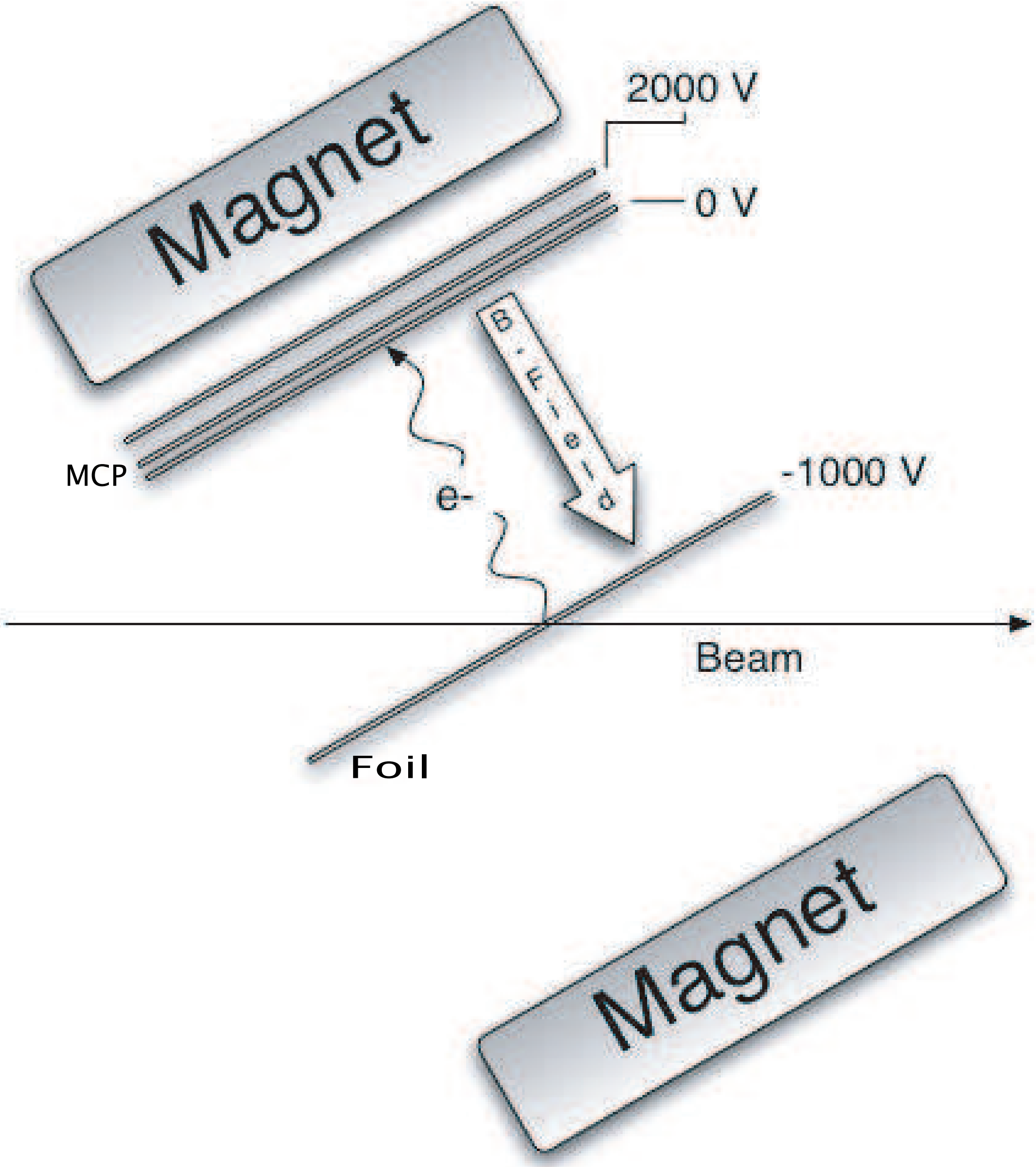

Figure 5.3: Schematic design of MCP setup

5.3.2 Position resolution

When a charged particle strikes the foil, secondary electrons are emitted. The number of electrons will depend on the work function of the target material and the energy loss near the surface. For 8.7 MeV alpha particles the number of secondary electrons emitted is typically 1, with^{40}Ca at 47 MeV/u, 10 secondary electrons are emitted. Increasing the number of emitted electrons improves the position resolution because it increases the signal amplitude.

The electrons emitted from the target foil have an energy that is typically less then 10 eV. They are emitted in random directions so some momentum is in the direction towards the MCP and some is perpendicular. There initial transverse momentum is non-zero. The magnetic field created between the two permanent magnets acts to confine the trajectory of an electron in a helical orbit as it travels towards the MCP. The radius of curvature of the electron trajectory is defined by the magnetic field between the target and MCP. For low energy electrons the radius is given by:

$$r \sim 3.37\sqrt{E}/B \tag{5.1}$$

where E is the initial electron energy perpendicular to the MCP. E is given in eV, and B is the magnetic field in Gauss. For electrons with a transverse energy of 3 keV accelerated in a 100 G field, the helical confining radius is 0.6 mm, i.e. the diameter is 1.2 mm. If the magnetic field is increased to 500 gauss, the diameter decreases to 0.24 mm. Thus, the use of very strong permanent magnets leads to improved position resolution. In our MCPs the field at the target has been measured to be 300 G and the magnetic field is 500 G at the MCP. A resolution of 0.25–0.5 mm could therefore be achieved. The exact value depends on the radial trajectory of the electron. The distance between the centers of neighboring channels in the MCP is about 12 μm. This is much smaller than the diameter of the helical electron orbit. This spacing of channels therefore has a negligible influence on the position resolution.

In addition to the magnetic field there is an electric field which is mostly parallel to the magnetic field. Increasing the strength of the electric field decreases the drift time from foil to MCP and improves the timing resolution, but does not influence the position resolution.

The resistive layer can be non-uniform and these non-uniformities can not be adjusted. The fast amplifier also has no gain adjustment. Therefore position spectra must be calibrated offline. The fast amplifiers used for the corners of the anode are ORTEC FTA820A which have a rise time ≤ 1 ns and a gain of $200 \pm 10\%$. The anode signals are then integrated by a CAEN V792 QDC.

A pedestal subtraction is done for each of the four corner signals. The position is then calculated by taking the difference between two signals on each side over the total signal. The spectrum is rotated and a linear calibration is done to display a mask calibration in units of mm. The corners have non-linear effects which can be corrected for by a global 2-D fit using the function:

$$\begin{aligned} X_{cal} &= X - a_1 + a_2 X + a_3 Y + a_4 X^2 + a_5 Y^2 \\ &\quad + a_6 X^3 + a_7 Y^3 + a_8 XY + a_9 X^2 Y + a_{10} Y^2 X \end{aligned} \tag{5.2}$$

where a_i are fit parameters and X, Y are the measured coordinates. Y_{cal} is also calibrated this way.

In order to calibrate the position of the MCPs a thin plate is attached to the target. Holes are drilled in this plate at known positions. The target foil is attached directly on this plate. The plate is thick enough to stop alpha particles. A plastic scintillator is placed behind the target. α-particles that hit the foil where there is a hole in the plate are stopped in the plastic. A MCP 2-D spectrum in coincidence with the plastic is shown in Figure 5.4. The holes are 3 mm apart, most holes have diameters of .75 mm but five larger holes were drilled with 1 mm diameter so as to provide a clear identification of the orientation for the mask. From this histogram the

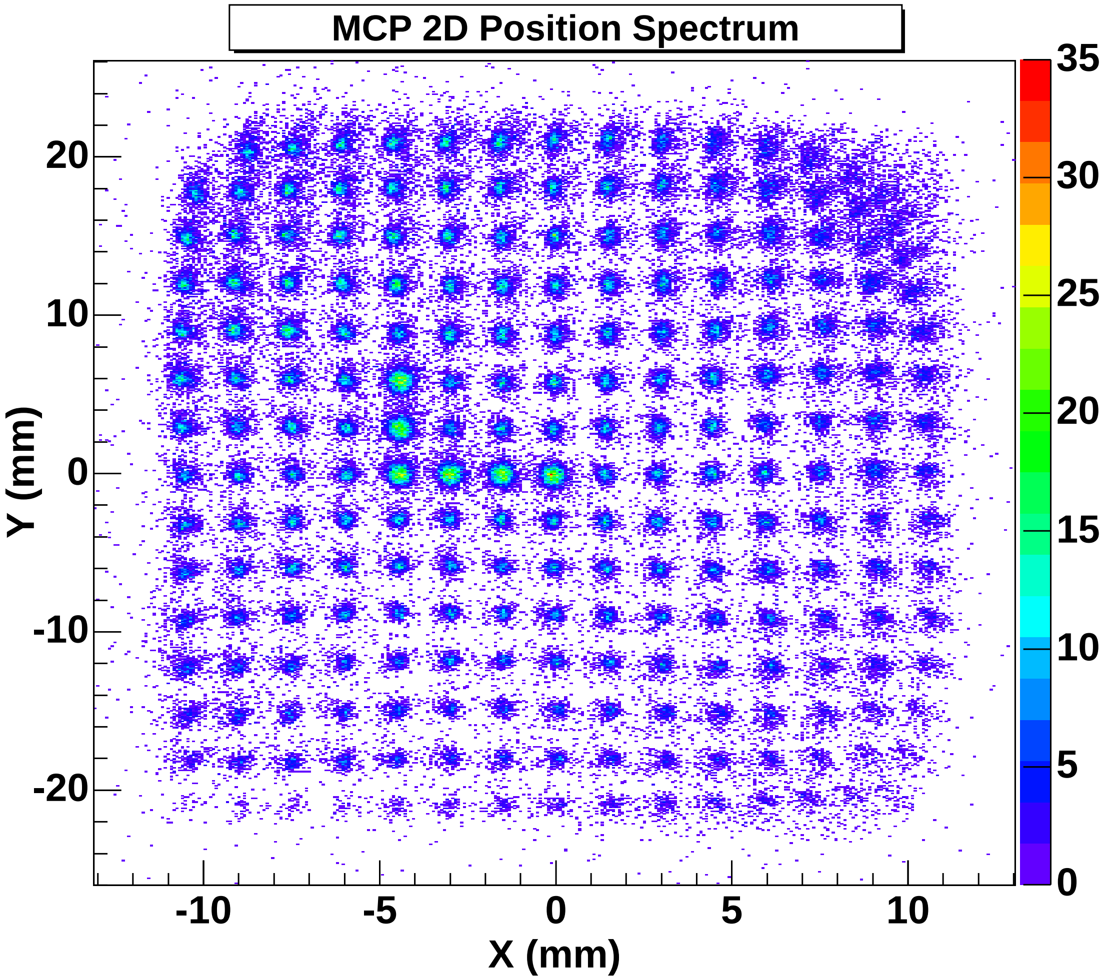

Figure 5.4: Spectrum of MCP mask calibration

deduced resolution is 0.35 mm in the X direction and 0.7 mm in the Y direction. The X resolution is better than the Y resolution because the foil is rotated around the vertical axis by 60 degrees, thus one is measuring $X \cos 60$, not X.

The resolution is not as good near the corners. This is likely caused by the small signal amplitudes of the corners. Note that this data was taken using 5.5 MeV alpha particles from an ^{241}Am source. Typically such alphas will generate 1 secondary electron per alpha particle. During our experiments with heavy rare isotope beams one expect 10–20 secondary electrons per beam ion. This should make the signals larger, and consequently, the signal to noise ratio at the edges should be much larger. During the experiments the beam will be 5 cm wide vertically and 1 cm wide horizontally.

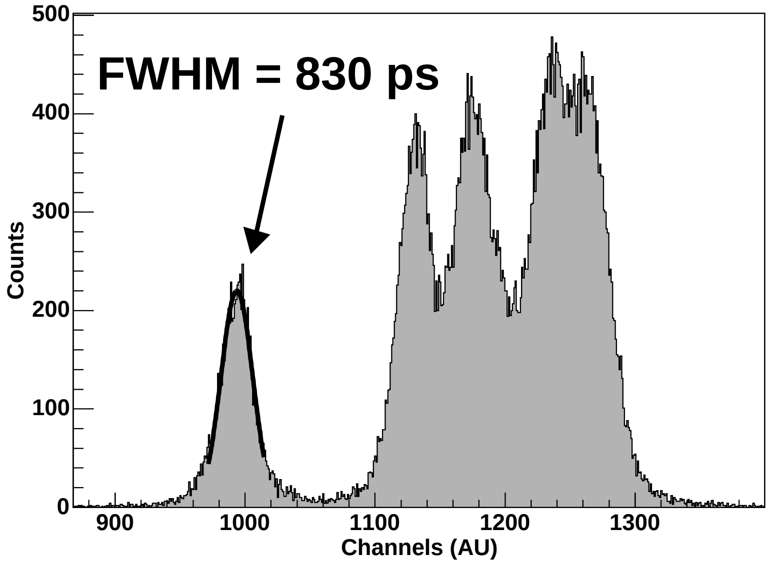

Figure 5.5: Time of flight spectrum between a MCP and a surface barrier detector

The resolution measured in this region with the alpha source is already sufficient to do the experiments.

5.3.3 Timing resolution

Timing resolution was also measured using a ^{228}Th alpha source. An MCP was setup in coincidence with a surface barrier silicon detector. Time of flight was then measured between the two detectors.

Figure 5.5 shows the time spectrum of one MCP in coincidence with a surface barrier silicon detector. The total resolution is shown in this figure to be 830 ps FWHM. This is a combination of the uncertainty of both detectors. The rise time on the MCP signal was measured to be about 3 ns and the rise time on the silicon detector was measured to be about 50 ns after the charge sensitive amplifier. Both signals used constant fraction discriminators followed by a single TDC with an intrinsic resolution of 30 ps. If one assumes the timing resolutions of the MCP and silicon detector are equal the MCP resolution would be 580 ps. If one assumes the timing resolution of the silicon detector is excellent, perhaps 300 ps, then the MCP resolution would be 770 ps.

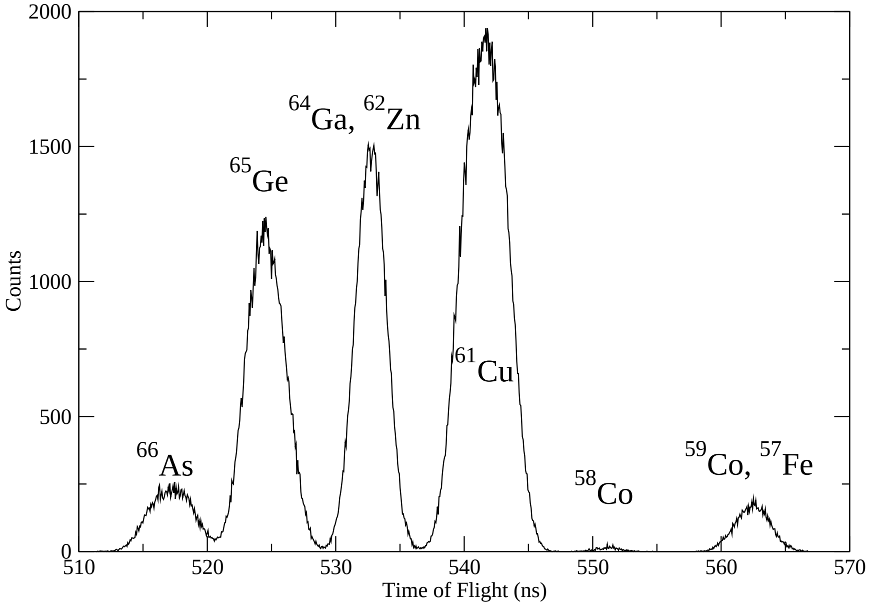

Figure 5.6: Simulated time spectrum for a cocktail beam containing ^{66}As

This is probably an upper limit on the resolution of the MCP. Figure 5.6 shows a simulated time spectrum for a cocktail beam containing ^{66}As, ^{65}Ge, ^{64}Ga, ^{62}Zn, ^{61}Cu, ^{58}Co, ^{59}Co, and ^{57}Fe. This calculation was performed with the program LISE++ assuming the timing was measured between the extended focal plane of the A1900 and the target position in the S800. The thin plastic scintillator at the extended focal plane was assumed to have 200 ps timing resolution, which is the typical resolution for the actual detector. From this, one can see that ^{66}As can be reasonably identified, as well as ^{65}Ge and ^{61}Cu. The other beams have similar flight times, and would require the S800's energy loss calculations to separate them. Identification prior to the target is not crucial as the S800 should be able to identify the outgoing particle in coincidence with the deuteron in the HiRA array. This is simply an additional parameter that can be used to clean up any background contamination.

5.3.4 Efficiency & counting rate

In order to measure the efficiency for heavy beams at high energy an experiment using the CCF at the NSCL was performed. A ^{40}Ca beam at 47 MeV/u was produced using

Figure 5.7: Image of the MCP setup in the 92” chamber

the A1900 fragment separator. Two MCPs were placed in the 92” scattering chamber in the N3 vault. A plastic scintillator was placed down stream.

Figure 5.7 is an image of the experimental configuration within the 92” chamber. Each of the MCPs was in its own copper cage. This was done to reduce pickup on the MCP signals. There is an entrance hole and an exit hole in each cage for the beam to travel. Downstream of the MCPs is a copper mask that can stop the beam, followed by a plastic scintillator. The copper mask is mounted on a target drive allowing it to be moved in and out of the beam.

The plastic scintillator placed downstream of the two MCPs served as the trigger for the data acquisition. The efficiency was therefore measured at various beam rates by looking at the coincidence between MCP and plastic. The results are shown in Table 5.1.

Table 5.1: MCP efficiency results for various beam rates

Beam Rate (pps)	MCP1 (%)	MCP2 (%)
9100	99	95
64000	99	95
930000	90	89

From this, one can see that for a beam of ^{40}Ca at 47 MeV/u the efficiency of each MCP each is 89 % or higher for a beam rate near 1×10^6 pps. This assumes a 100 % effiency for the plastic. The mask placed between the two MCPs and the plastic limited the rate of particles stiking the plastic to less then $1{\times}10^4$ pps. At this rate the plastic should be very efficient. The effiency for higher Z particles with the same energy should only increase with increasing energy loss in the foils, because that increases the secondary electron emission.

Based on the results of beam tests and α source tests, the MCP tracking detector system will provide the required resolution, beam rate, and efficiency needed for (p,d) transfer reaction mass measurements. It also has a timing resolution sufficient enough to allow incoming beam identification for many of the beams considered.

5.4 The full experimental setup

A description of HiRA and the MCPs has been given, at this point a description of the beam and full configuration of the (p,d) reaction hardware setup will be given for a measure of the mass of ^{65}As and ^{64}Ge.

Figure 5.8 shows the K500 and K1200 cyclotrons, and the A1900 fragment separator with a person shown to represent the scale of the figure. The beam starts as ^{78}Kr in the ion source. The ion source ionizes ^{78}Kr to a low charge. It is then injected into the K500 cyclotron where it is accelerated and transmitted to the K1200 cyclotron. In the center of this cyclotron it strikes a striper foil which will remove the remaining electrons. The ^{78}Kr is then accelerated to 140 MeV/u. The beam impinges upon a beryllium production target at the beginning of the A1900. The ^{78}Kr is fragmented by the beryllium target. This produces nuclei with masses ranging from ^{78}Kr down to protons. The first half of the A1900 filters out all particles that don't have the same mass to charge ratio as ^{66}As. At the intermediate image of the A1900, the beam is dispersed in the horizontal direction based on momentum. Slits are placed here to allow ±0.25 % momentum distribution about the central ray to transmit through the seperator. There is a wedge in the intermediate image that will slow the beam down. The energy loss in the wedge is described by the Bethe Equation 3.4. Particles with different charge and mass will consequently lose different amounts of energy. The second half of the A1900 fragment separator is then used to remove particles that do not have energy losses that leave them in the momentum acceptance of the A1900.

In this mode, the A1900 basically transmits an isotone chain. This means ^{65}Ge will be transmitted, along with ^{66}As. The rate of ^{65}Ge will be as large or slightly larger then ^{66}As. Additional nuclei with lower mass will also be transmitted. These will serve as calibration masses as they are closer to stability and have experimentally determined masses. This will allow a simultaneous measurement of the ^{65}As and ^{64}Ge masses and the calibration masses at the same setting of the beam line. The calibration masses allow one to absolutely calibrate the Bρ setting of the beam line. Using such calibrations one obtains the mass of ^{65}As and ^{64}Ge which gives one the Q-value for the ^{64}Ge$(p,\gamma)^{65}$As reaction.

After the A1900 the beam will travel to the extended focal plane where there is a thin plastic scintillator. This will serve as the start detector for a TOF measurement of the beam. Beyond the extended focal plane is the transfer hall and following that the S800 beam-line. Figure 5.9 is a 3-D rendering of the S800 spectrograph, with a person shown for scale. The beam will travel through the analysis line in dispersion matched mode to the target position inside the large (green) chamber at the ground level. The person in Figure 5.9 is standing next to this chamber. This chamber was designed and built to accommodate the HiRA detector system.

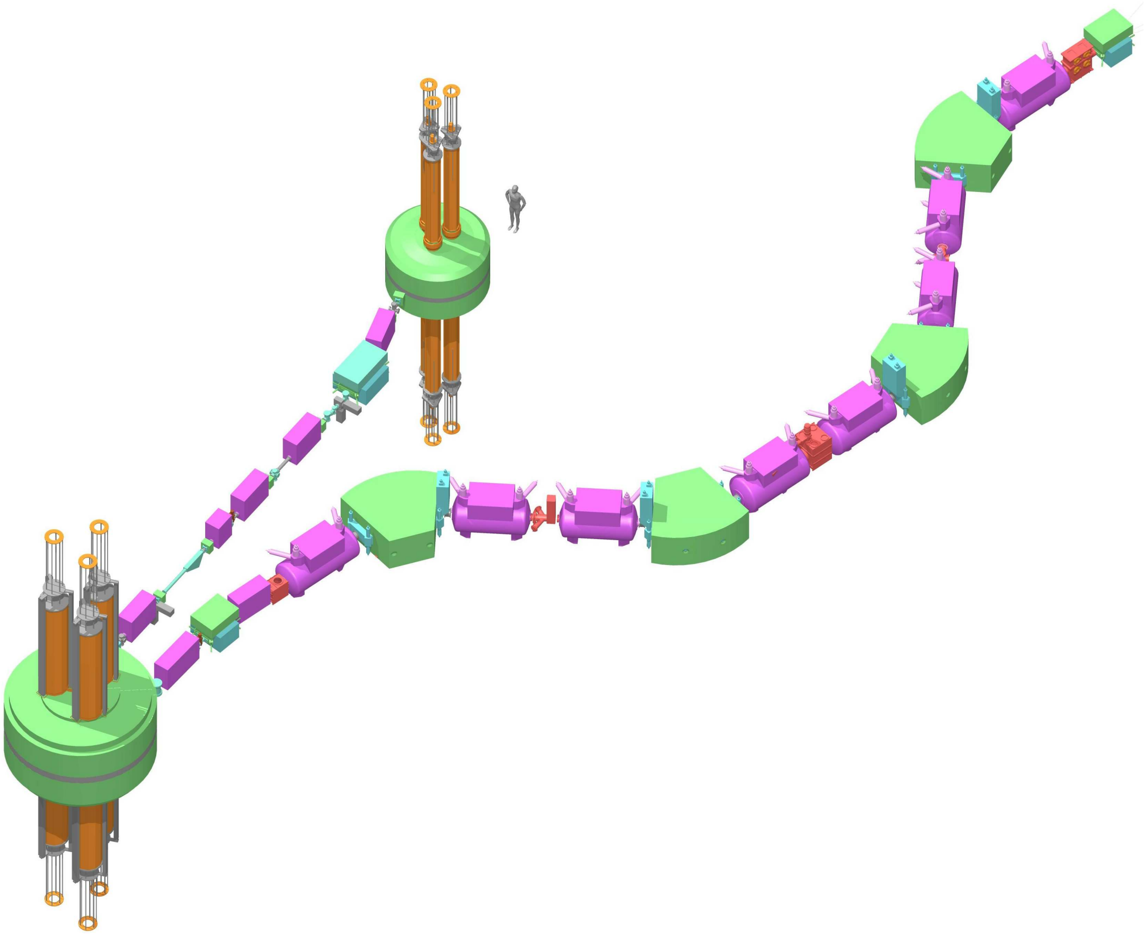

Figure 5.8: The NSCL cyclotrons and the A1900 fragment separator

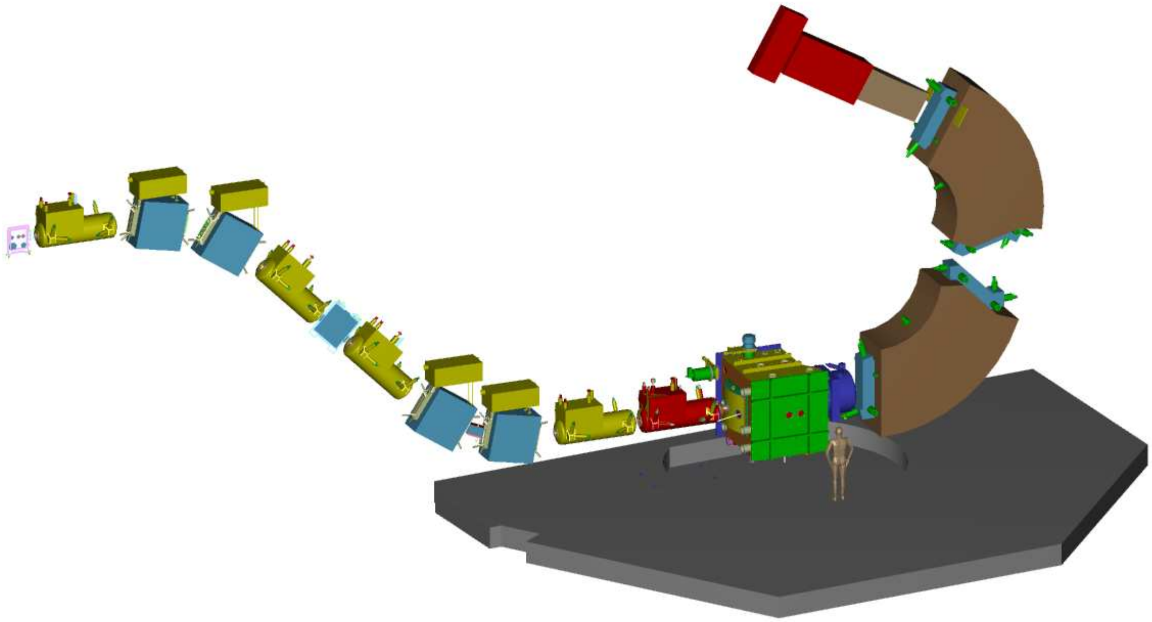

Figure 5.9: The S800 Spectrograph

In dispersion matched mode the vertical position at the target will be directly correlated with the momentum of the beam particle, relative to the centerline momentum. The beam will focus to a point in the focal plane in this ion optics mode. Ions that undergo (p,d) reactions in the target will lose one neutron in the target and therefore rigidity will be reduced. These particles will strike the focal plane detectors. Beam particles that do not react in the target will maintain their original rigidity, bend less then the reacted beam, and strike a beam dump in the second bending dipole of the S800.

The inside of the S800 scattering chamber is shown in Figure 5.10. It will contain two MCPs. The first one will be at the entrance of the chamber. This will give a position and time for the beam. The MCP electron emission foil will consist of a 150 μg/cm^2 aluminized mylar foil placed in the beam-line. The reaction target will also serve as the emission foil of the second MCP, and will be located 50 cm downstream from the first MCP. The target will be 0.5–1 mg/cm^2 polypropylene foil with about 1.5 nm of aluminum evaporated on the entrance side. This aluminum is necessary to

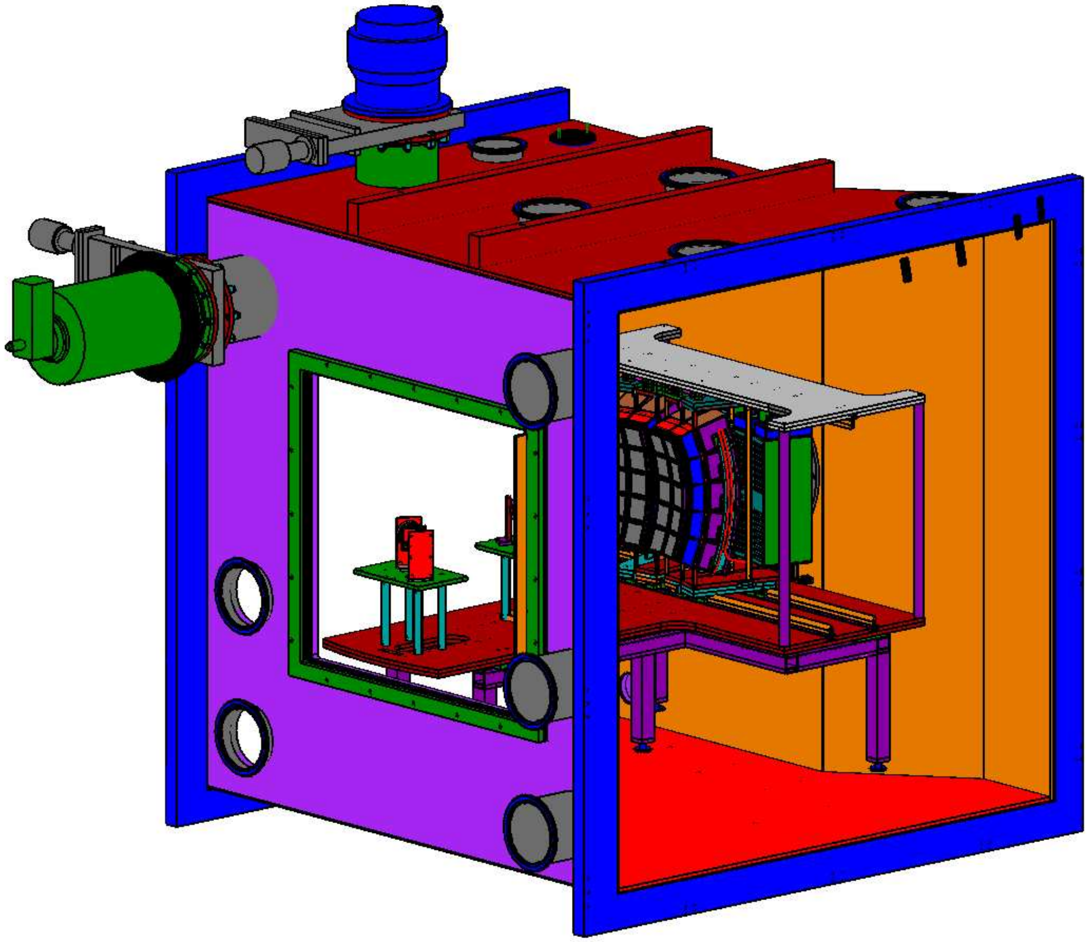

Figure 5.10: S800 Target Chamber with HiRA and MCPs in it

apply a voltage to the target, which accelerates the secondary electrons to the MCP. HiRA will be mounted at a distance of 50 cm downstream from the target MCP. This will allow coverage up to about 25 degrees in the lab. The energy of the deuterons at the angle are high enough that they can punch through the 1.5 mm silicon detector. The energy resolution from the CsI is not good enough, therefore the coverage of hira at a distance of 50 cm from the target will cover nearly all deuterons of interest for mass measurements.

Chapter 6

Summary and future work

This chapter is broken down into two components, the first will be a discussion of the key points in this dissertation and the corresponding results from. The second component is a discussion of the present experimental program and an outlook for future experiments utilizing the results of the work of this dissertation.

6.1 Summary

The first goal stated in the introduction was to define what are the key nuclear physics properties that can effect our understanding of X-ray bursts on the surface of neutron stars. The second goal was to determine how to measure these properties taking into consideration the accuracy that would be required to do so. The third goal was to develop the required tools to perform the measurements to the required accuracy.

Chapter 2 described the development of the program GAMBLER, and the results of GAMBLER calculations. These calculations indicate that the most important properties to determine experimentally are the masses of ^{64}Ge and ^{65}As because these masses govern the first, and longest waiting point in the rp-process above ^{56}Ni. It was shown that the time it takes to process from ^{64}Ge to the next potential waiting point ^{68}Se can vary between 10s to 100s of seconds depending on the masses of ^{64}Ge and

^{65}As. It was also pointed out that reaction rates in this region are calculated based on narrow resonances in states determined from studies of mirror nuclei. At lower temperature towards the end of the burst, the abundances of nuclei beyond the ^{65}As, are not in nuclear statistical equilibrium and are therefore sensitive to the existence of and energies of states within the Gamow window.

The calculations in Chapter 3 indicated the masses of ^{64}Ge and ^{65}As, along with level information could be measured to an accuracy better then 25 keV if sufficiently high resolution detectors are used in the appropriate configuration. The three measured quantities required to calculate the masses are the energy of the deuteron, the energy of the beam, and the reaction angle. The energy of the deuteron can be measured to 50 keV or better with a thick enough silicon detector. The beam energy can be measured with relatively modest position resolution of a few millimeters, utilizing the dispersion matching ion optics setting of the S800 analysis line and a position sensitive channel plate detector. The reaction angle can be determined to sufficient accuracy if there is 50 cm between two position measurements using two micro channel plate detectors sitting in the scattering chamber.

Chapter 4 described the design, construction, and testing of the High Resolution Array (HiRA), which will be used to measure the deuterons. Initial measurements suggest the energy resolutions of the silicon detectors are better then 40 keV. However the present electronics for processing the signals of the thick silicon detectors will limit the energy resolution. Current tests indicate the resolution is about 50 keV which should still be sufficient, however this is an area where improvement can be made.

The reaction angle measurement is strongly dependent on the position measurement of the beam. It was shown in Chapter 5 that the initial plan to use PPACs might be insufficient for this purpose and this led to the development of the MCP tracking system. Tests with these MCPs show that a resolution better than 1 mm is possible. This is critical as one must master all of the components of the measurement simultaneously in order to achieve the accuracy of 25 keV that was identified here.

Based on the work of this thesis an experimental program is underway to make the experiment a reality. At this time, the first set of experiments is planned and is therefore discussed in the following section.

6.2 Future work

6.2.1 ^{65}As Measurement

In the near future, there will be a final experimental test with the full detector system to verify all detectors functions to there full capabilities. After this is done, a measurement of the mass and level structure of ^{65}As and ^{64}Ge as well as many calibration nuclei will be done. This will be the first attempt for precision mass measurements far from stability using a transfer reaction.

6.2.2 Measurements beyond the proton drip-line

Depending on the actual masses of ^{64}Ge and ^{65}As and hence the Q-value for the ^{64}Ge$(p,\gamma)^{65}$As reaction, additional measurements may be required. The next waiting point in the process is the ^{68}Se- ^{69}Br region. ^{69}Br is proton unbound, however proton capture leading the rp-process through successive proton captures to ^{70}Kr may be possible, depending on the mass and structure of unbound ^{69}Br. The mass of ^{69}Br can obviously not be measured by a Penning trap because ^{69}Br is particle unbound and ^{70}Kr has a half life around 50 ms. This would be the next logical measurement. Beyond that is the ^{72}Kr waiting point. This would require a measurement of ^{72}Kr and ^{73}Rb.

6.2.3 Other reactions

The work of this thesis has been focused on using the (p,d) reaction for studies of mass and level structure. The detectors developed could also be used to do other direct reactions such as (d,p), (d,^{3}He), (t,p), proton elastic and inelastic scattering, and knockout to measure properties of neutron rich nuclei.

Bibliography

[1] H.A.Bethe. *Phys. Rev.*, **55**:103, 1939.

[2] C.W.Cook, W.A.Fowler, C.C.Lauritsen, and T.Lauritsen. *Phys. Rev.*, **107**:508, 1957.

[3] E.M. Burbidge, G.R.Burbidge, W.A.Fowler, and F.Hoyle. *Rev. Mod. Phys.*, **29**:548, 1957.

[4] A.G.W. Cameron. *Publications of the Astronomical Society of the Pacific*, **69**:201, 1957.

[5] J.Grindlay, H.Gursky, H.Schnopper, D.R.Parsignault, J.Heise, A.C.Brinkman, and J.Schrijver. **205**:127, 1976.

[6] F.-K.Thielemann, M.Arnould, and J.W.Truran. *Advances in Nuclear Astrophysics*. Frontiere, Gif sur Yvette, 1987.

[7] T.Rauscher and F.-K.Thielemann. *Stellar Evolution, Stellar Explosions and Galactic Chemical Evolution*. IOP, Bristol, 1998.

[8] T.Rauscher and F.-K Thielemann. *Atomic Data and Nuclear Data Tables*, **75**:1, 2000.

[9] H.C.Graboske, H.E.DeWitt, A.S.Grossman, and M.S.Cooper. **181**:457, 1973.

[10] H.E.DeWitt, H.C.Graboske, and M.S.Cooper. **181**:439, 1973.

[11] F.X.Timmes, 2005. http://www.cococubed.com/code_pages/codes.shtml.

[12] F.X.Timmes and F.D.Swesty. *Astro. Phys. Journal. Sup.*, **126**:501, 2000.

[13] L.Bildsten. *The many Faces of Neutron Stars*, **1**:419, 1998.

[14] J.R.Buchler and W.R.Yueh. **210**:440, 1976.

[15] H. Schatz, L. Bildsten, A. Cumming, and M. Wiescher. **524**:1014, 1999.

[16] A.Y.Potekhin, G.Chabrie, and D.G.Yakovlev. **323**:415, 1997.

[17] N.Itoh, H.Hayashi, and Y.Kohyama. **404**:268, 1993.

[18] A.Y.Potekhin, D.A.Baiko, P.Haensel, and D.G.Yakovlev. **346**:345, 1999.

[19] G.Bader and P.Deuflhard. *Numerische Mathematik*, **44**:373, 1983.

[20] W.H.Press, W.T.Vetterling, S.A.Teukolsky, and B.P.Flannery. *Numerical Recipes in C++*. Cambridge University Press, 2002.

[21] T.A.Davis, 2005. http://www.cise.ufl.edu/research/sparse/umfpack.

[22] T.A.Davis. *ACM Trans.Math.Software*, **30**:165, 2004.

[23] A.Cumming and L.Bildsten. **544**:453, 2000.

[24] L.Van Wormer, J. Görres, C.Iliadis, M.Wiescher, and F.-K.Thielemann. **432**:326, 1994.

[25] J. Clark, 2005. Private communication.

[26] A.H.Wapstra, G.Audi, and C.Thibault. *Nucl. Phys. A*, **729**:129, 2003.

[27] B.A.Brown, R.R.C.Clement, H.Schatz, A.Volya, and W.A.Richter. *Phys. Rev. C*, **65**:045802, 2002.

[28] H.Savajols. *Hyperfine Interactions*, **132**:245, 2001.

[29] M.Chartier, W.Mittig, G.Auger, B.Blank, J.M.Casandjian, M.Chabert, J.Fermè, , L.K.Fifield, A.Gillibert, A.S.Lalleman, A.Lèpine-szily, M.Lewitowicz, M.Maccormick, M.H.Moscatello, F.Deoliveira, N.A.Oor, G.Politi, F.Sarazin, H.Savajols, C.Spitaels, P.van Isacker, A.C.C.Villari, and M.Wiescher. *Hyperfine Interactions*, **132**:275, 2001.

[30] A.S.Lalleman, G.Auger, W.Mittig, M.Chabert, M.Chartier, J.Fermè, A.Gillibert, A.Lèpine-szily, M.Lewitowicz, M.H.Moscatello, N.A.Orr, G.Politi, F.Sarazin, H.Savajols, P.van Isaker, and A.C.C.Villari. *Hyperfine Interactions*, **132**:315, 2001.

[31] G.F.Lima, A.Lépine-Szily, G.Audi, W.Mittig, M.Chartier, N.A.Orr, R.Lichtenthaler, J.C.Angelique, J.M.Casandjian, A.Cunsolo, C.Donzaud, A.Foti, A.Gillibert, M.Lewitowicz, S.Lukyanov, M.MacCormic, D.J.Morrissey, A.N.Ostrowski, B.M.Sherril, C.Stephan, T.Suomijarvi, L.Tassan-Got, D.J.Vieira, A.C.C.Villari, and J.M.Wouters. *Phys. Rev. C*, **65**:044618, 2002.

[32] YU.A.Litvinov, F.Attallah, K.Beckert, F.Bosch, M.Falch, B.Franzke, H.Geissel, M.Hausmann, TH.Kerscher, O.Klepper, H.J.Klung, C.Kozhuharov, K.E.G.Löbner, G.Munzenberg, F.Nolden, Yu.N.Novikov, Z.Patyk, W.Quint, T.Radon, C.Scheidenberger, M.Steck, L.Vermeeren, and H.Wollkik. *Hyperfine Interactions*, **132**:283, 2001.

[33] G.Bollen, F.Ames, D.Beck, J.Dilling, O.Engels, S.Henry, F.Herfurth, A.Kellerbauer, H.-J.Klung, A.Kohl, E.Lamour, D.Lunney, R.B.Moore, M.Oinonen, C.Scheidenberger, S.Schwarz, G.Sikler, J.Szerypo, and C.Weber. *Hyperfine Interactions*, **132**:215, 2001.

[34] G.Savard, R.C.Barber, D.Beeching, F.Buchinger, J.E.Crawford, S.Gulick, X.Feng, E.Hagberg, J.C.Hardy, V.T.Koslowsky, J.K.P.Lee, R.B.Moore, K.S.Sharma, and M.Watson. *Nucl. Phys. A*, **626**:353, 1997.

[35] B.E.Tomlin, C.J.Barton, N.V.Zamfir, M.A.Caprio, G.L.Gill, R.Krücken, J.R.Novak, J.R.Cooper, K.E.Zyromski, G.Cata-Danil, C.W.beausang, A.wolf, N.A.Pietralla, H.Newman, J.Cederkall, Benyuan Liu, Z.Wang, R.F.Castena, and D.S.Brenner. *Phys. Rev. C*, **63**:03414, 2001.

[36] LISE++, 2005. http://nscl.msu.edu/lise.

[37] B.Davin, R.T.de Souza, R.Yanez, Y.Larochelle, R.Alfaro, H.S.Xu, A.Alexander, K.Bastin, L.Beaulieu, J.Dorsett, G.Fleener, L.Gelovani, T.Lefort, J.Poehlman, R.J.Charity, L.G.Sobotka, J.Elson, A.Wagner, T.X.Liu, X.D.Liu, W.G.Lynch, L.Morris, R.Shomin, W.P.Tan, M.B.Tsang, G.Verde, and J.Yurkon. *Nucl. Instr. and Meth. A*, **473**:302, 2001.

[38] Micron Superconductor LTD, 1 Royal Buildings,Marlborough Road, Lancing, Sussex BN158UN, England.

[39] Glenn F. Knoll. *Radiation Detection and Measurment, 3rd edition.* John Wiley & Sons, Inc, New York, 1999.

[40] Pico Systems, 534 Lindeman Rd. Kirkwood, MO 63122.

[41] W.G.Gong, Y.D.Kim, G.Poggi, Z.Chen, C.K.Gelbke, W.G.Lynch, M.R.Maier, T.Kurakami, M.B.Tsang, and H.M.XuK.Kwastkoski. *Nucl. Instr. and Meth. A*, **268**:190, 1988.

[42] D.W.Stracener, D.G.Sarantites, L.G.Sobotka, J.Elson, J.T.Hood, Z.Majka, V.Abenate, A.Chbihi, and D.C.Hensley. *Nucl. Instr. and Meth. A*, **294**:485, 1990.

[43] D.G.Sarantites, P.-F Hua, M.Devlin, L.G.Sobotka, J.Elson, J.T.Hood, D.R.LaFosse, J.E.Sarantites, and M.R.Maier. *Nucl. Instr. and Meth. A*, **381**:418, 1996.

[44] R.T.de Souza, N.Carlin, Y.D.Kim, J.Ottarson, L.Phair, D.R.Bowman, C.K.Gelbke, W.G.Gong, W.G.Lynch, R.A.Pelak, T.Peterson, G.Poggi, M.B.Tsang, and H.M.Xu. *Nucl. Instr. and Meth. A*, **295**:109, 1990.

[45] A.Wagner, W.P.Tan, K.Chalut, R.J.Charity, B.Davin, Y.Larochelle, M.D.Lennek, T.X.Liu, X.D.Liu ad W.G.Lynch, A.M.Ramos, R.Shomin, L.G.Sobotka, R.T.de Souza, M.B.Tsang, G.Verde, and H.S.Xu. *Nucl. Instr. and Meth. A*, **456**:290, 2001.

[46] I.Iori, L.Manduci, A.Moroni, R.Scardaoni, Sun ChongWen, Zhang Yuzhoa, Zhang Guangming, F.Giglio, E.Mora, G.Di Pietro, L.Dellera, A.Cortesi, R.Bassini, C.Boiano, S.Brambilla, M.Malatesta dn M.Bruno, M.D'Agsotino, M.L.Fiandri, E.Fuschini, P.M.Milazzo, G.Busacchi, A.Cunsolo, A.Foti,

C.Gianino, G.Sava, F.Gramegna, P.Buttazzo, G.V.Margagliotti, G.Vannini, G.Auger, and E.Plagnol. *Nucl. Instr. and Meth. A*, **325**:458, 1993.

[47] A.R.Gabler, W.Döring, M.Fuchs, B.Krusche, V.Metag, R.Novotny, M.R öbig Landau, H.Ströher, V.Tries, C.Molenaar, H.Löhner, J.H.G.van Pol, A.Raschke, M.sumbera, L.B.Venema, H.W.Wilschut, R.Averbeck, W.Niebur, A.Schubert, R.S.Simon, R.Beck, J.Peise, G.J.Miller, R.O.Owens, and G.Anton. *Nucl. Instr. and Meth. A*, **346**:168, 1994.

[48] F.Cavallari. *Nucl. Instr. and Meth. A*, **461**:368, 2001.

[49] P.Schotanus and R.Kamermans. *IEEE Trans. Nucl. Sci.*, **37**:177, 1990.

[50] J.B.Birks. *Theory and Practice of Scintillation Counters.* Pergammon Press, Oxford, 1964.

[51] M.Pârlog, B.Borderie, M.F.Rivet, G.Tabacaru, A.Chbihi, M.Elouardi, N.Le Neindre, O.Lopez, E.Plagnol, L.Tassan-Got, G.Auger, Ch.O.Bacri, N.Bellaize, F.Bocage, R.Bougault, B.Bouriquet, R.Brou, P.Buchet, J.L.Charvet, J.Colin, D.Cussol, R.Dayras, A.Demeyer, D.Dorè, D.Durand, J.D.Frankland, E.Galichet, E.Genouin-Duhamel, E.Gerlic, S.Hudan, D.Guinet, P.Lautesse, F.Lavaud, J.L.Laville, J.F.Lecolley, C.Leduc, R.Legrain, M.Louvel, A.M.Maskav, L.Nalpas, J.Normand, J.Pèter, E.Rosato, F.Saint-Laurent, J.C.Steckmeyer, B.Tamain, O.Tirel, E.Vient, C.Volant, and J.P.Wieleczko. *Nucl. Instr. and Meth. A*, **482**:674, 2002.

[52] S.Burachas, S.Beloglovski, I.Makov, Y.Saveliev, N.Vassilieva, M.Ippolitov, V.Manko, S.Nikulin, A.Vassiliev, A.Apanasenko, and G.Tamulaitis. *Nucl. Instr. and Meth. A*, **486**:83, 2002.

[53] F.A.Danevich, A.Sh.Georgadze, V.V.Kobychev, B.N.Kropivyansky, A.S.Nikolaiko, O.A.Ponkratenko, V.I.Tretyak, S.Yu.Zdesenko, and Yu.G.Zdesenko. *Phys. Rev. C*, **62**:045501, 2000.

[54] MOSIS, 4676 Admiralty Way, 7th Floor Marina del Rey CA 90292-6695.

[55] D. Shapira, T.A. Lewis, and L.D.Hulett. *Nucl. Instr. and Meth. A*, **454**:409, 2000.

[56] D. Shapira, T.A. Lewis, L.D.Hulett, and Z.Ciao. *Nucl. Instr. and Meth. A*, **449**:396, 2000.

[57] D. Shapira and T.A. Lewis. *IEEE Trans. Nucl. Sci.*, **47**:1974, 2000.